

University of Trento
Department of Physics



Doctoral thesis:

**Implementation of an all-optical setup for
insect brain optogenetic stimulation and
two-photon functional imaging**

Tutor:
Albrecht Haase

Ph.D. student:
Mirko Zanon

XXXII Doctoral Cycle in Physics
Academic year 2019 - 2020

Contents

Abstract.....	4
Introduction.....	5
Theoretical background.....	7
Insect nervous system.....	9
1.1 Neurons.....	9
1.2 Olfactory system.....	12
Microscopy.....	15
2.1 Fluorescence imaging.....	15
2.2 Two-photon microscopy.....	21
2.3 Recording neuronal activity with calcium sensors.....	24
Optogenetics.....	26
3.1 Engineered light-based actuators.....	27
3.2 Applications.....	29
All-optical implementation.....	32
Experimental work.....	35
Materials and methods.....	37
5.1 All-optical setup.....	37
5.2 Setup characterization.....	41
5.3 HEK cell lines.....	44
5.4 Insect preparation and drosophila lines.....	45
Insect preparation.....	45
Drosophila lines.....	47
5.5 Experimental protocol.....	49
5.6 Signal and response characterization.....	50
5.7 Odorants characterization.....	52
5.8 Custom analysis software.....	53
Results.....	56
6.1 Experiments on HEK cells.....	56
6.2 Experiments on <i>drosophila</i>	60
6.2.1 Odor stimulation.....	61
6.2.2 Whole brain responses to optogenetic stimulation.....	66
6.2.3 Antennal lobe stimulation.....	73
6.2.4 Single glomerulus stimulation.....	77
6.3 Data analysis.....	79

Conclusions	87
Bibliography	89
Personal articles	99
Index of abbreviations	99
Index of figures.....	100
Acknowledgments	103

Abstract

Insect brain is a very complex but at the same time small, simplified and accessible model with respect to the mammalian one. In neuroscience a huge number of works adopt *drosophila* as animal model, given its easiness of maintenance and, overall, of genetical manipulation. With such a model one can investigate many behavioral tasks and at the same time have access to a whole brain in vivo, with improved specificity and cellular resolution capabilities.

Still, a remarkable goal would be to gain a precise control over the neural network, in order to fully manipulate specific areas of the brain, acting directly on network nodes of interest. This is possible thanks to optogenetics, a technique that exploits photosensitive molecules to modulate molecular events in living cells and neurons. At the same time, it is possible to perform a neuronal readout with light, exploiting calcium-based reporters; in this way, neuronal response investigation can gain in temporal and spatial resolution. This is an all-optical approach that brings many advantages in the neural network study and an insight in the functional connectivity of the system under investigation.

We present here a setup that combines a two-photon imaging microscope, capable of in vivo imaging with a sub-cellular resolution and an excellent penetration depth down to hundreds of microns, with a diode laser optogenetic stimulation.

With such a setup we investigate the *drosophila* brain in vivo, stimulating single units of the primary olfactory system (the so-called glomeruli, about 20 μm of diameter). By our knowledge this is one of the first time a similar all-optical approach is used in such an animal model: we confirm, in this way, the possibility to perform these experiments in vivo, with all the advantages coming from the improved accessibility of our model.

Moreover, we present the results using a sample co-expressing GCaMP6 and ChR2-XXL, optimal performing sensor and actuator, largely exploited in the field for their high efficiency: these were rarely used in combination, since their spectral overlap, nevertheless we are able to show the feasibility of this combined approach, enabling to take advantage from the use of both these performing molecules.

Finally, we will show different approaches of data analysis to infer relevant information about correlation and time response of different areas of the brain, that can give us hints in favor of some functional connectivity between olfactory subunits.

Introduction

In the last decades the field of neuroscience underwent a huge development: different neural network functions were studied, both structurally and functionally, and improved maps of neuronal connections and functions were constructed. The importance of all these developments is fundamental both in the pure research field and in the applicational one, like for example in branches like neurosurgery, neurology and psychiatry. Progressing with these studies, it appeared clear the necessity to reach a precise and specific control over neural network functions: this dream was already pointed out in 1979 by Francis Crick, who remarked that “to understand these higher levels of neural activity we would obviously do well to learn as much as possible about the lower levels,” going on to suggest that “a method by which all neurons of just one type could be inactivated, leaving the others more or less unaltered” would be required to make advances in basic neuroscience.” (Crick, 1979). Different options were investigated and had a large success in many applications: electrical manipulation for example can be a good candidate for a temporally precise control, but still not enough spatially; on the other hand, spatial selectivity can be reached in some extent with pharmacology and other techniques, lacking otherwise temporal precision since they act on long time scales. Even if these techniques allow for a very high level of neuronal control, a combination of spatial and temporal resolution remained still hardly accessible.

The solution became clear in 2005 when optogenetic techniques started to be developed consistently in the neuroscience field (Boyden et al., 2005): that is a combination of optical and genetic tools to precisely control biological systems. The use of light to activate photosensitive molecules (opsins) is a powerful tool in neuronal control, since it permits the combination of genetic precision (expressing the opsin only in subpopulations of neurons of interest) with the physical spatial accuracy dictated by the illumination source, like for example a collimated laser beam; at the same time temporal precision is given by the fast dynamic of the opsin response.

Clearly, a full application of all these capabilities remained limited, since many constraints also occur: for example, depending on the specific opsin structure, a very collimated light could target not enough molecules to elicit neuronal response, or the dynamic of the sensor could be not fast enough to report single action potential signals; during the last years many different molecules were thus engineered and improved, and at the same time used with different excitation sources like lamps, LEDs or lasers, such as with different readout methods like electrophysiology or behavioral assays. In particular, an interesting readout technique is the optical one: imaging techniques, such as calcium imaging, are largely pointed as ideal detection instruments in combination with optogenetics, even if many difficulties occur with this combined approach. The idea is that of constructing an all-optical setup, in which both the excitation of the neurons and their response are controlled by light, and at the same time a direct feedback control can be performed creating a closed loop tool which can be fundamental also for practical applications; clearly, many limitations arise here, since a particular attention has to be taken considering spectral overlap between opsins and calcium sensors, and at the same time the sources of excitation and imaging have to be chosen properly not only to work but also not to release too much energy damaging the sample. Still, efforts to overcome these limitations are constant, and also nowadays developments are progressing. At the beginning the attention was focus on the use of sources like lamps or LEDs, illuminating big areas of the neural system under interest; a refinement consists in the use of a laser, a more collimated source: very few works pointed out the use of a one-photon laser activation, orienting nowadays all towards the most expensive technology of two-photon lasers capable of a better spatial resolution with respect to the classical one-photon (Zipfel et al., 2003).

A more detailed insight in these questions and studies is reported in chapter 4.

With this work, instead, we want to prove the possibility of combining the powerful two-photon excitation technique to perform the imaging protocol, with the simpler and less expensive solution of a one-photon activation laser source, still capable of good spatial precision (in the order of tens of microns).

A detailed description of the two-photon system and its advantages is provided in chapter 2.2, our setup is described in chapter 5.1, while the power and parameters optimizations are reported in chapter 6.

Finally, the work is developed studying the *Drosophila* brain. This insect is largely used in neuroscience since its convenience for genetical modifications; moreover, thanks to its small size, it brings an improved accessibility to an *in vivo* brain, with respect to other bigger animals like mice. The advantages of two-photon imaging fit perfectly with this model, allowing for a detailed study going down to cellular level and up to the whole brain, with an optimal capability for in depth imaging down to hundreds of microns. Importantly, insects like flies and bees are studied in many comparative works with the human brain, being a simplified model to study and develop results useful to be extended to mammalian brain processes understanding and to the applicational sector like diseases investigation; particularly, many analogies can be found in the olfactory pathway (Sinakevitch et al., 2018).

I've applied the all-optical approach trying to investigate functional connectivity at the level of the primary olfactory centers (the antennal lobes) of *Drosophila*; in this way we can improve our investigation of insect olfactory system, completing the study of antennal lobe connectivity and characterization of stimuli elaboration, already performed with more classical but less controllable stimuli like odorants (Paoli et al., 2018). A description of the brain and olfactory system of the fly can be found in chapter 1.2, while all the optogenetic experiments and results are reported in chapter 6.

We can state that our work can be relevant in the neuroscience field, since, even if already applied in other animals, it is one of the first time an all-optical approach like this is shown in *Drosophila*, with all the advantages reported before, given by the combination of both a simplified but potent two-photon setup and the simple but powerful animal model itself.

Part I

Theoretical background

Chapter 1

Insect nervous system

1.1 Neurons

The central nervous system combines information from the entire body and coordinates activity across the whole organism; synthesizing inputs from different sensory neurons that individually encode a tiny and specific part of the total environment, it is also the fundamental machinery responsible for producing behavior: it integrates many different sensory inputs and produces sophisticated representations of the outside world and the internal state of the insect. This is performed by its coordination of the activity of about 300 skeletal muscles, driving the body in precise spatial and temporal actions and monitoring the consequences during ongoing behavior.

The basic unit of the nervous system is the nerve cell, the neuron: it consists of a cell body, *soma*, (containing the nucleus, abundant mitochondria, Golgi complexes and endoplasmic reticulum), and one or more projections to make contact with other neurons or organs. The regions specialized for the reception of incoming signals are called *dendrites*, the main projection which conducts signal over long distances is called *axon*, while the points at which neurons convey or receive information are known as *synapses*; quite all insects' central nervous system neurons are monopolar, meaning they have only the axon as single projection from the soma, that then branches forming the dendritic input regions and arborize to contact regions (see Figure 1); peripheral sense cells are instead usually bipolar, while other cells occurring in the ganglia can be multipolar.

Each neuron is almost fully covered by folds of one or more *glial cells*, more abundant than neurons in the central nervous system; here they have an important role in the development of the system itself, they pass nutrient materials to the neurons and probably play a role in reparations. Synaptic contacts can occur only where these glial folds are absent; between the glial cells there is the extracellular space.

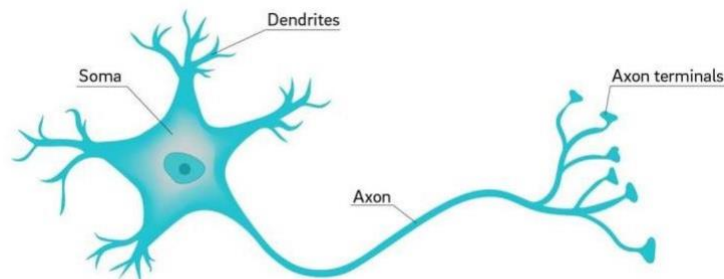


Figure 1 Sketch of a monopolar neuron.

At the level of most synapses, the transmission from one cell to the other involves mainly chemical messengers: the two plasma membranes are closed together, separated by a gap of 20 – 25nm called synaptic cleft, and in the adjacent cytoplasm there are synaptic vesicles containing the chemical transmitter that is released into the cleft. Chemical messengers have three types of function:

- 1 *neurotransmitter*: released in the synaptic cleft and with a transient effect on the electrical potential (acetylcholine is probably the most widespread one in insects);
- 2 *neuromodulator*: released in the vicinity of the synapse, modifying synaptic transmission with a slow and long-lasting effect;
- 3 *neurohormone*: released into the hemolymph, functioning as hormones.

Some neurons can instead be directly in electrical contact: in this case the current can flow straight across the gap, that is smaller (about 3.5nm), and the connection is called gap junction.

The number of synapses can change during development and with the experience of the insect in a process called plasticity, that alter the strength of physiological connection and is fundamental particularly in the formation of long-term memory.

Neurons, as all cells, present a difference in electrical potential that is maintained across the plasma membrane: the inside is negatively charged with respect to the outside; for this reason, the cell is said to be polarized. This resting potential is about -70 mV and arises from the differential distribution of negatively and positively charged ions creating an electrochemical gradient across the cell membrane, and from the membrane permeability to these different ions itself. This is due to the combination of several factors; one of these is the presence of large, non-diffusible organic anions within the neuron, while most cations (Na^+ , K^+ , Ca^{2+}) can cross the membrane (Donnan equilibrium is established); moreover a large chemical gradient for potassium is present across the cell membrane, due to the action of sodium-potassium pumps, which use ATP to exchange Na^+ ions from the cell with the outside (in a ratio of 3:2); also the cell is more permeable to K^+ than to Na^+ , so that potassium ions are at higher concentration within it, while sodium and chloride ions have higher concentration outside.

A change in the potential toward zero, i.e. a decrease in its negative charge, is called depolarization; if instead an increase in negativity occurs, we call it hyperpolarization. These electrical variations (triggered by chemical alterations in ion concentration) are how signals are encoded at the level of neurons.

Transmission of signals via the nervous system involves three processes:

- 1 the incoming signal, chemically encoded, is converted in an electrical one; the *receptor potential*, i.e. change in membrane potential produced by the incoming signal, spreads passively through the neuron, but it decays exponentially in amplitude as current leaks back, across the neural membrane;
- 2 the electrical signal is actively transmitted along the axon as *action potentials*, in a self-sustaining wave of depolarization, covering, in this way, large distances without attenuation;
- 3 the electrical signal depolarizes the adjacent cells, with the generation of a new receptor potential.

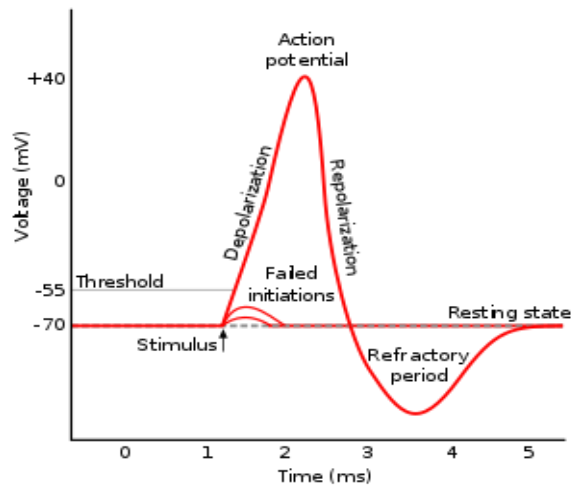


Figure 2 Action potential: cell depolarization and repolarization after a stimulus onset are depicted; a refractory period follows before the cell is back to its resting state.

What it is supposed to happen during the transformation from receptor potential to action potentials is the encoding of the signal voltage amplitude into action potential spiking rate and number, resulting in a 'digital' input: in this way the number and frequency of these inputs give information about any original signal magnitude. What it happens in every case, is the generation of an action potential every time enough depolarization brings the membrane potential up to a certain threshold (about -55 mV). It follows that, differently from receptor potentials with stimulus dependent amplitudes, the one of an action potential isn't related to the amount of current producing it, but instead it's an all-or-none threshold signal, encoding a digital information. The total number of action potentials produced in the unit time is called firing rate.

The total duration of an action potential is about 2-3ms and it is characterized by different phases (Figure 2 Action potential: cell depolarization and repolarization after a stimulus onset are depicted; a refractory period follows before the cell is back to its resting state.):

- 1 *depolarization*: as the receptor potential spreads passively, it induces a current, producing a small depolarization of the membrane in the axon and causing voltage-sensitive sodium channels to open; this determines a rapid positive swing in the charge on the inner membrane. During this rising phase, the period of permeability to sodium is short because the sodium channels close automatically and become inactivated;
- 2 *repolarization*: falling phase in which the change in voltage activates potassium channels, but does it slowly than with sodium channels, starting to open them at sodium channels closure. Potassium flows out of the cell and brings down its electrochemical gradient, restoring the more negative charge inside.
- 3 *refractory phase*: phase in which sodium channels stay inactivated and the continuous outflow of potassium blocks any tendency for depolarization; this means that for 2 – 3ms no more change in the membrane potential can occur in the area through which the action potential has just passed.

Thus, there is a current flow away from the depolarization point inside the axon, and inversely toward it on the outside: where this current reaches an area of resting membrane it produces a slight depolarization propagating the action potential; the conduction velocity in a nerve fiber generally has a square root proportionality with the diameter, but it can change also with temperature.

1.2 Olfactory system

The brain is the principal association center of the body, since it receives sensory inputs from very different sense organs; three main regions are recognized: the protocerebrum, deutocerebrum and tritocerebrum. We will now focus our general description on the principal sites connected to odor information processing in insect (fly and bee) brain. Odor is perceived by *olfactory receptor neurons* (ORNs) at the level of the antennae and maxillary palps; here the chemical signal is converted in an electrical one and transmitted through ORNs axons to specific glomeruli in the first olfactory centers (*antennal lobes*, ALs). In these areas synaptic contacts are formed with *local interneurons* and *projection neurons* (PNs), which project to higher brain centers, the mushroom bodies (MBs) and/or lateral horns (LHs) (Figure 3, Sayin et al., 2018). In the following the main areas are described in detail.

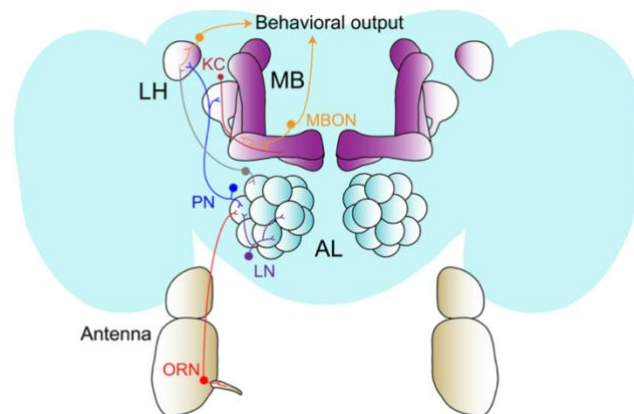


Figure 3 Sketch of *drosophila* olfactory pathway: the odor is detected by ORNs at the level of the antennae, information is passed to glomeruli in the AL and sent to higher order centers (MBs and LHs) through PNs (Sayin et al., 2018)

- The primary olfactory centers are located in the deutocerebrum, containing the *antennal olfactory lobes* (ALs) and the antennal mechanosensory and motor centers. The two antennal lobes, related to the two antennae, are formed by spherical subunits of dense synaptic neuropil, called *glomeruli*; axons from olfactory sensilla on the antenna terminate in these glomeruli, axons of the same receptor projecting to only one glomerulus (Fishilevich & Vosshall, 2005); from here they synapse onto *projection neurons* (PNs) passing information to higher order processing centers, principally the calyces of the *mushroom bodies* and other regions in the dorso-lateral edge of the protocerebrum called *lateral horns*. There is also a third population of interneurons, the *local neurons*, entirely confined to the antennal lobe, interconnecting different glomeruli. Within a species, glomeruli seem to be constant in shape and position; in the *drosophila* brain, for example, there are about 50 glomeruli per antennal lobe, while in bee 160. Most of the projection neurons use acetylcholine as transmitter, while others use the inhibitory GABA, on the contrary interneurons are mainly inhibitory using GABA or histamine.

The relatively large number of glomeruli and output neurons provides the insect with the potential to distinguish a very large number of odors using patterning activation. In fact many studies were conducted about odor recognition and discrimination, starting from the receptor neurons level, where works in *drosophila* shown that the activity of each neuron scales with the concentration of the odor and the sensitivity across odorants follow a power-law distribution (Si et al., 2019); moreover, broadly tuned receptors (activated by different odors) were shown to be more sensitive to structurally similar odorants, and receptors with similar odor sensitivity often map to widely dispersed glomeruli (Hallem

& Carlson, 2006). At the level of antennal lobes, interesting studies demonstrated that odors are codified by specific glomerular pattern of activation, highly conserved among individuals, both in mammals (for example in mice) olfactory bulb (analogous of the antennal lobe in insect), and in insects like bees and fruit flies (Galizia et al., 1999; Haase et al., 2011; J. W. Wang et al., 2003); moreover not only the spatial information is relevant, but also the temporal activation of different glomerular units plays a fundamental role in stimuli elaboration (Martelli et al., 2013; Paoli et al., 2016; Seth, 2015). In particular, focusing on ALs response, we found a predictable way to recognize an odor presented to a bee simply looking at the temporal and spatial activation of glomeruli, adding the temporal aspect complementary information to the solely intensity spatial pattern (Paoli et al., 2018). Both functional modifications and structural plasticity were discovered at the level of ALs after learning and experience-dependent processes (Andrione et al., 2017; Faber et al., 1999).

- The second order olfactory centers are the *mushroom bodies* (MBs) and *lateral horn* (LH), located in the protocerebrum. The protocerebrum occupies a dorsal position in the head; antero-dorsally there is a region called pars intercerebralis, at which side are the MBs, consisting of a cap (calyx), from which a stalk (peduncle) runs ventrally dividing in two or three lobes (α, β, γ lobes); calyces can be double, comprising three concentric rings known as lip, collar and basal ring: this is a characteristic of insects with large olfactory system, like bees. The form of calices is given by a large number of interneurons (*Kenyon cells*) which have their somata above the calyx: a typical Kenyon cell has dendrites in the calyx and an axon running down the stalk that divides ventrally to form α and β lobes.

The relative size of MBs is generally related to the complexity of behavior in the insect; furthermore, changes in them occur with age: for example, the number of fibers in *Drosophila* mushroom bodies increases more than 20% over the first week of adult life, increasing the calyx volume; moreover, this process is affected by the insect's experience both in *Apis* and *Drosophila*. Mushroom bodies are involved in both olfactory and visual learning, therefore they are considered as multimodal integration centers between the two senses, encoding stimulus quality of a given modality at the level of the input and nonlinear integrating the information across the two modalities at the output (Strube-Bloss & Rössler, 2018); there is also evidence of their role in some decision making processes.

Furthermore, it was shown that bees with anesthetized MBs are still capable of elemental olfactory discrimination, but not of ambiguous problems; inhibition of GABAergic signaling in the calyces, but not in the lobes, in the same way impairs non-elemental learning, suggesting a requirement of GABAergic feedback neurons from the lobes to the calyces for complex learning (Devaud et al., 2015).

The information encoded at the level of the MBs is sparse and broader with respect to the primary elaboration centers, nonetheless some interesting results were enlightened, like the fact that most Kenyon cells subsets, still integrating random combination of inputs, receive stereotyped inputs from single PNs, maximizing performances on a stimulus discrimination task (Eichler et al., 2017); moreover, looking at the processing of temporal variation of olfactory stimuli, a significant temporal transformation between sensory neurons and PNs spike patterns was found, manifested by the PNs output strongly signaling the sensory neurons spike rate and its rate of change (A. J. Kim et al., 2015). Studies were also conducted to understand odor elaboration process through PNs, showing PNs organization and their conserved representation of odors from the ALs (Jeanne et al., 2018; Seki et al., 2017), and how the information is elaborated passing from ALs to MBs and LH (Galizia, 2014).

It is clear how many efforts were spent in order to investigate the function of all these brain structures, and many information are available at the moment. In particular, at the level of the primary centers, the ALs, different studies revealed the role of the glomeruli in odor discrimination, as reported previously. Still, a complete connectome of glomeruli and, moreover, of their projections to different regions of the mushroom bodies is missing. Optogenetics is an optimal tool in order to target a specific node of this glomerular network, and manipulate it to understand its specific role within the AL; moreover, investigating functional activity in a living insect will provide a solid base to address these questions. Our setup, being capable to merge the optogenetic glomerular targeting with functional imaging *in vivo*, will give a contribution to the field, showing the possibility to address all the previous points: ideally, it could be used to target specific glomeruli and reconstruct a complete connectome of the AL; furthermore, more advance investigation can be performed at the level of MBs too. To our knowledge, this is one of the first time a similar all-optical approach is applied to study *in vivo* functional connectivity in drosophila, being published only recently one similar work (Huang et al., 2019).

Chapter 2

Microscopy

Light is a fundamental tool to target and have access to a large number of cells simultaneously; thus, the use of fluorescence light to control and monitor neuronal activity became a common practice in the last decade. The study of neuronal circuits is usually performed *in vivo* by near-infrared light, capable of minimizing scattering and optimizing spatial resolution via multiphoton processes. Different approaches focused also on the three-dimensional accessibility with complementary techniques, to access volume up to hundred microns (Ronzitti et al., 2018). In this chapter I will give an introduction about fluorescence imaging process, arriving to describe two-photon imaging potentialities and functional imaging with calcium sensors.

2.1 Fluorescence imaging

Fluorescence

Luminescence is the process which describes the emission of photons from any electromagnetically excited substance. Electrons in an excited electronic state are able to re-emit (radiatively or not) the previously absorbed energy, going back to their ground state. Luminescence refers to the radiative emission and it's formally divided in two categories, depending on the nature of the excited state and consequently to the time scales of the process:

- *Fluorescence*: the excited electron is in a singlet state and hence the transition to the ground state is spin allowed; this transition occurs rapidly, within a time of the order of $10^{-9}s$.
- *Phosphorescence*: the excited electron is found in a triplet state and hence the transition to the ground state is spin forbidden by the selection rule (i.e. highly improbable). This transition will occur within longer times, typically of the order of *ms* to *s*.

Usually, these transitions are graphically represented with a Jablonski diagram (see Figure 4), (Antosiewicz & Shugar, 2016). In normal conditions, at room temperature, no excited electronic states neither higher vibrational states of S_0 can be populated simply by thermal contribution: only when the proper energy is externally supplied, molecules get excited to some higher vibrational energy level of the excited state, relaxing to the lowest one soon after (generally within $10^{-12}s$ or less), through internal conversion. After this, molecules typically go back to an excited vibrational state of S_0 , releasing energy as fluorescence light, and internal conversion happens again. A different phenomenon can also occur, when molecules in the S_1 state undergo an intersystem crossing driven by a spin conversion to the first excited triplet state T_1 : since the lifetime of this state is bigger, the light emission will occur with longer times and we assist to the phosphorescence process.

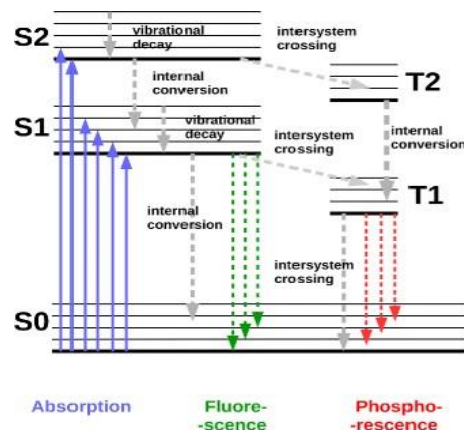


Figure 4 Jablonski energy level diagram of luminescence processes: fluorescence and phosphorescence are depicted. The singlet ground, first and second electronic states are depicted by S0, S1 and S2, triplet states with T1 and T2; moreover, some vibrational energy levels are added to the graph. Radiative transitions are shown as colored arrows, while non-radiative processes are represented by gray arrows (Antosiewicz & Shugar, 2016).

Further considerations can be done:

- Fluorescence emission always occurs at longer wavelengths (i.e. lower energies) than absorption; this energy loss is mainly due to non-radiative relaxations and eventually to fluorophore interactions with the environment. This energy difference is called *Stokes shift*.
- Emission spectra are typically independent on the excitation wavelength; this is due to *Kasha's rule*: it states that all excited states relax through non-radiative processes, i.e. emission of photons happens always only from the lowest energy state of the excited level, whatever the absorbed energy.
- Looking at the transitions between S0 and S1 (which in general are predominant), fluorescence spectra are usually mirror images of absorption ones, given by the presence of non-radiative processes.
- The fluorescence lifetime corresponds to the time in which the molecule stays in the excited state, before to fall back to the ground state. For a first order decay the number of molecules N in the excited state, $-\frac{dN(t)}{dt} = kN(t)$; integrating, $N(t) = N(0)e^{-kt}$. In a uniform population of excited molecules, the decay in time of fluorescence intensity is described by an exponential function: $I(t) = I(0)e^{-t/\tau}$. The constant τ gives the time in which the fluorescence decays to $\frac{1}{e}$ $\sim 37\%$ of the starting fluorescence.
- The fluorescence emission is polarized if the fluorophores are excited with polarized plane light; the level of polarized emission depends on the anisotropy of the specimen, since the fluorophores absorb preferentially the photons with an electric field vector parallel to the dipole momentum of the transition (the absorption probability is proportional to the squared cosine of the angle between the dipole and the incident radiation electric field vector).

Clearly, there could be exceptions to all of these rules, mainly depending on environmental characteristics, such as temperature, pH, presence of other compounds and so on.

Molecules responsible for fluorescence emission are said fluorophores: they are typically constituted of aromatic groups with atoms arranged in one or more rings and electrons delocalized in π -bonds. Fluorophores can be generally divided in two main classes:

- *Intrinsic fluorophores*: they occur naturally in biological systems, such as aromatic amino acids (tryptophan, tyrosine, phenylalanine), coenzymes NAD(P)H and flavins;
- *Extrinsic fluorophores*: they are added to the sample to provide fluorescence when it is not naturally present. They can be used to label proteins, membranes, DNA, or to detect membrane potential or ion currents.

Every fluorophore has its specific fluorescence excitation and emission spectra, which can be taken as reference to fix the appropriate wavelengths of excitation and signal detection. An example is shown in Figure 5.

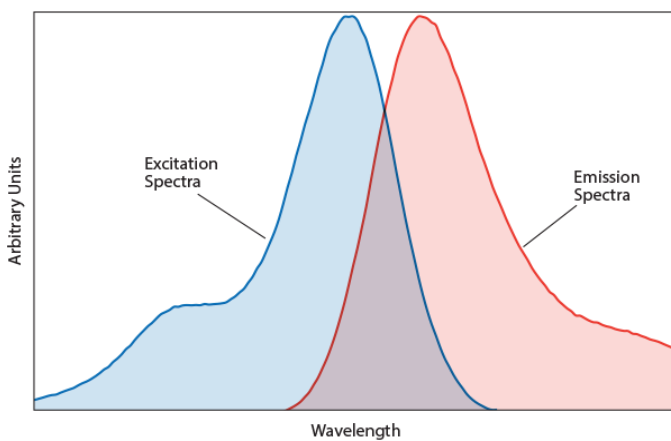


Figure 5 Example of fluorescence absorption (blue) and emission (red) spectra. The emission spectrum is red-shifted (Stokes shift) with respect to absorption one.

From wide-field to confocal imaging

In 1852 Stokes was the first at describing fluorescence, noticing that this kind of emission was always characterized by longer wavelength with respect to the excitation light's one; also, first investigations in the 19th century showed that many specimens (ranging from minerals to chlorophyll and different inorganic compounds) exhibit fluorescence upon ultraviolet light irradiance. In the 1930s fluorochromes were introduced in biology to stain tissue components, bacteria, and other pathogens; later in the 1950s the technique to label antibodies with a fluorescent dye was developed (Albert et al., 1950).

Fluorescence has the advantage of providing a very high signal-to-noise ratio, which enables to distinguish spatial distribution of even low concentration species. In 1961 the Green Fluorescent Protein (GFP), a naturally fluorescent protein present in jellyfish, was discovered (Shimomura et al., 1962), and in 1994 it was successfully expressed in other organisms (Chalfie et al., 1994): this was an evolution in the field and since then, fluorescence microscopy, coupled to optical microscopy, has become an essential tool in biology and biomedical sciences to study cellular and tissue structure and dynamics at the molecular level, given the significant increase in detected signal achieved with respect to the weak autofluorescence of biological samples. A further improvement was reached with the development of lasers in the 1960s: they offered a high degree of spatial and temporal coherence with the possibility of focusing the beam in a tiny spot of very high local irradiance. Moreover, it became possible to effectively separate the fluorescence signal by using filters and dichroic mirrors: the majority of fluorescence microscopes used in life sciences is composed by epifluorescence microscopes, where the objective used for focusing the excitation beam on the sample is also used to capture fluorescence signal, and the two beams are separated by a dichroic mirror. Nowadays, fluorescence microscopy is an essential tool in biomedical sciences for live cell imaging and for studying normal and pathological cell biological processes, using fluorophores to specifically target the molecules of interest; moreover, fluorescence techniques are generally less destructive than other imaging techniques, such as electron microscopy.

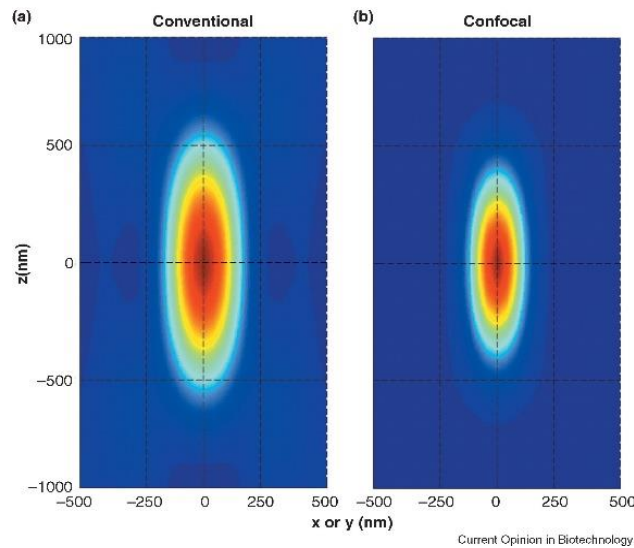


Figure 6 Point spread function as observed along the y axis: (a) for a conventional microscope, (b) for a confocal microscope. Function calculated for $NA=1$ and $\lambda = 500\text{nm}$ (Garini et al., 2005).

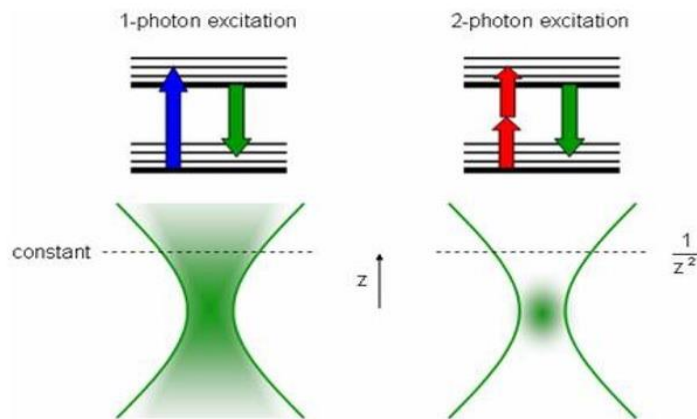
In principle, not only fine cellular structures, but even single molecules, can be imaged with fluorescence microscopy: the limitation is given by the fact that they have to be enough spatially separated to be resolved. The microscope resolving power is in fact limited by the wave-like nature of the electromagnetic radiation, actually to approximately half the wavelength, corresponding to about 200nm for visible light. Furthermore, being the light diffracted, the image of an illuminated point source is significantly broadened and it is seen as a central bright spot (Airy disc) surrounded by diffraction rings (Airy patterns): its intensity distribution is called point spread function (PSF, see Figure 6), (Garini et al., 2005). The diffraction limit was first pointed out in 1873 by Abbe (Abbe, 1873), as $d = \lambda/2NA$ where d is the resolvable size, λ is the illumination wavelength and NA is the numerical aperture of the objective, defined as $NA = n\sin\alpha$, with n refractive index of the medium between the objective and the sample and α half the observation angle. All this means that one can resolve a specific detail in the sample if the numerical aperture of the objective is large enough to capture its first order diffraction pattern (central Airy disc). The Abbe theory was then refined in 1896 by Rayleigh who quantified the separation between two Airy patterns in order to be able to distinguish them as separate entities: his criterion states that they are distinguishable if the center of one Airy disk falls on the first minimum of the other (Wolf, M. Born, 1961); thus, resolution of a conventional microscope can be estimated as: $d_{xy} = 0.61\lambda/NA$ (lateral resolution), $d_z = 2\lambda n/NA^2$ (axial resolution) (Garini et al., 2005), and it is directly related to the FWHM of the PSF.

In a wide-field microscope the entire image plane is illuminated at once usually by a filtered mercury or xenon source: in this case the fluorescence image is the sum of sharp image details from the in-focus-region, combined with blurred image from all the out-of-focus regions, leading to a reduction of image contrast. This becomes a problem especially with thick samples: the image of a biological specimen will only be in focus if its axial dimension is minor than the axial resolution limit (given by the objective parameters). This is why, in the development of fluorescence microscopes, spatial resolution was identified as the main parameter on which to improve. As previously mentioned, the introduction of laser sources gave a big boost in the development of high-resolution microscopy, becoming able to focalize the excitation laser source in small spots, with raster scanning imaging of the sample. An example is confocal laser scanning microscopy (CLSM); its principle was originally presented by Marvin Minsky in 1957, but it became a standard technique only thirty years later toward the end of the 1980s. CLSM takes advantage of a conventional epifluorescence microscope combined with an excitation laser beam by which point-by-point illumination with simultaneous point-by-point detection is performed; with the use of a pinhole, out-of-focus scattered photons are rejected, increasing the signal-to-noise ratio and obtaining better lateral and axial resolution with respect to widefield microscopy. As can be understood, resolution depends on the diameter of the pinhole: the smaller the diameter, the better the resolution but at the same time the less the image brightness. For a very small pinhole (diameter approaching zero) the following formulas were derived: $d_{xy} = 0.37\lambda/NA$ (lateral resolution), $d_z = 1.4\lambda n/NA^2$ (axial resolution).

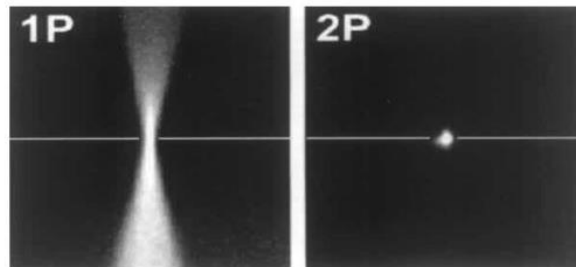
To obtain the final image of the focal plane, the focused spots are rapidly and serially scanned in the xy plane by a deflection mechanism (for example with galvo-mirrors); furthermore, changing the height of the objective, it is possible to focus on different z positions, imaging diverse in-depth planes of the sample. The emitted photons are separated from excitation ones by a dichroic mirror. Since each pixel is excited individually, the resulting image can no longer be viewed by eye or cameras, but the pixel intensity value must be captured by specific devices such as photomultiplier tubes (PMTs), with a digital reconstruction of the image. To note that, since confocal microscopy permits optical sectioning (the acquisition of well-focused images from various sample depths), it is possible to obtain also 3D reconstructions of the specimen.

Clearly, even if the out-of-focus photons problem is reduced with this method, it's not completely solved, since, given the light propagation shape, the sample is still illuminated inside a cone area surrounding the region of interest (see Figure 7, left), leading quickly to photobleaching and photodamage. A different way to obtain confocality and improve this problem is to exploit a physical process called multi-photon absorption: this type of microscopy is a form of laser scanning technique that uses localized nonlinear excitation (the energy absorbed is no more linearly proportional to the illumination power) to induce fluorescence only in a focused plane; thanks to its characteristics, it's one of the most suitable imaging techniques for microscopy in thick tissue and in live animals.

The primary signal source in multi-photon microscopy is given by two-photon excited fluorescence, even if three-photon, second and third harmonic generation can be of big interest too, as demonstrated by their parallel development since '90s (Barad et al., 1997; Freund & Deutsch, 1986; Gryczynski et al., 1995; Xu et al., 1996).



<http://biomicroscopy.bu.edu/research/nonlinear-microscopy>



M. Rubart (2004) Two-Photon Microscopy of Cells and Tissue. *Circulation Research* 95:1154-1166

Figure 7 One photon vs. two photon excitation process

2.2 Two-photon microscopy

Two-photon process was proposed for the first time in 1930 by Maria Göppert Mayer (Goepper Mayer, 1931): the mechanism consists in the excitation of a molecule via absorption of two quanta of light (of less energy with respect to one-photon process), in a time interval of the order of 10^{-16} s, during a single quantum event involving intermediate virtual (physically not allowed) energy states (Figure 7, right) (Diaspro & Robello, 2000).

In general, we have a power law relationship of the type $F \propto I^n$, where F is the fluorescence intensity, I the incident intensity and n the number of absorbed photons. Hence it follows that 2PE fluorescence is proportional to the intensity squared: doubling the intensity will lead to a 4-fold fluorescence emission (Goepper Mayer, 1931). From this it follows that $N_{2P} = \sigma_{2P} I^2$ where N_{2P} represents the number of absorbed photons per second and σ_{2P} is the two-photon cross section. Having N_{2P} units of *photons/s* and I units of *photons/cm²s*, σ_{2P} has to be in units of *cm⁴/photon*. Cross-sections for multi-photon absorption are very small compared to the ones for single-photon absorption (from 10^{-15} to 10^{-17} cm²) and generally two-photon cross-sections are measured in GM (Goeppert-Mayer) units, where $1GM = 10^{-50}$ cm⁴/photon. Intrinsic molecules, such as coenzyme NADH (reduced nicotinamide adenine dinucleotide), have extremely low two-photon action cross-sections ($< 10^{-4}GM$), while common fluorescent dyes have values in the range 1-300 GM (Zipfel et al., 2003). Being the two-photon cross-sections so small, high photon fluxes, of the order of 10^{30} photons/cm²s, are needed to make the process happen.

The transition probability P at time t from ground state n to an excited state m (via intermediate virtual state k), indicating with φ the wavefunction for a given state, is

$$P_m(t) = \frac{2\pi t}{\hbar^3} \left| \sum_k \frac{|\langle \varphi_n | \mu \epsilon | \varphi_k \rangle| |\langle \varphi_k | \mu \epsilon | \varphi_m \rangle| \epsilon^2}{\omega_{kn} - \frac{1}{2}\omega} \right|^2 \rho\left(\frac{\omega}{2} = \omega_{mn}\right)$$

where ϵ is the polarized field, μ the dipole moment, ρ the density of the excited states and ω represents transition frequency; in particular the resonance condition is $2\omega = \omega_{nm}$.

From this formula the transition rate can be extracted by partially deriving on time the transition probability, to finally obtain the absorption cross section:

$$\sigma_{n \rightarrow m} = \frac{2\pi t}{\hbar^3} \left| \sum_k \frac{|\mu_{nk}| |\mu_{km}|}{\omega_{kn} - \frac{1}{2}\omega} \right|^2 \rho\left(\frac{\omega}{2} = \omega_{mn}\right)$$

where $\mu_{nm} = \sum_i \int \varphi_n^* \mu_i \varphi_m d^3r$ is the dipole matrix element. Some interesting considerations follow.

- The excitation process depends no more linearly on the light intensity as for conventional microscopy, this is why it is said to be non-linear; since it depends on the squared energy (E_2), the fluorescence intensity depends on the distance from the axial focal point (z) as:

$$I_{\text{fluorescence}} \propto 1/z^4$$

Moreover, the fluorescence molecules are spread in three-dimensional space as the square of the intensity distribution: by this effect, the two-photon microscopy reveals as a powerful tool with high axial resolution and consequently 3D intrinsic capability.

Furthermore, the absorption cross section is very low, compared to the single photon one; this is related to the fact that two simultaneous quanta of light are rarely available for two-photon absorption.

For all these reasons the exciting fields have to have very high peak intensities, and, still, the probability for the process to occur is high enough only in the higher power points (the very focal region).

The pulse width (τ_p) must be chosen much smaller than the fluorescence lifetime of the fluorophores, which is of the order of few ns, and typical pulse widths less than 100 fs are used. On the contrary, the repetition rate (f_p) of the pulses must account for a repetition time longer than the lifetime, and values around 100 MHz are typically used.

To have a quantitative idea, obtaining (from $E = hc/\lambda$) the photons flux for a laser power of 1mW, one can estimate

$$1 \text{ mW} \sim \lambda \cdot 10^{12} \text{ photons/s/nm} \sim 10^{15} \text{ photons/s}$$

(for a typical two photon wavelengths of $\sim 900 \text{ nm}$); to calculate the intensity at the focus, this value must be divided by the area of the beam in the focal plane ($\sim 10^{-9} \text{ cm}^2$), giving an intensity of $\sim 10^{24} \text{ photons/cm}^2/\text{s}$. Thus, the intensity squared at the focus gives an increased probability of 10^7 times compared with the unfocused beam.

This ensures that the emission light is only coming from the focal plane and a point-to-point scanning 3D imaging is possible without the requirement of a pinhole. Thus, resolution limits achievable are the same as for confocal microscopy:

$$r_{plane} = \frac{0,61\lambda}{NA} \sim 0,5\mu m$$

$$r_{axial} \sim 2\mu m$$

Still, an high spatial and temporal density of photons required to induce non-linear effects is not achievable with old light sources without damaging the biological sample: this is why its application to biology has been long delayed after the first experimental proof in '60s by Kaiser and Garret with a $\text{CaF}_2 : \text{Eu}^{2+}$ crystal sample (Kaiser & Garrett, 1961); the first application to laser scanning microscopy arrived in 1990 with Denk (Denk et al., 1990). Not to release too much power on the sample and at the same time increase the process probability, a very fast pulsed laser is needed to fulfill these requirements; actually, the use of multi-photon microscopy increased exponentially as femtosecond laser sources became available (as it is visible in Figure 8 for the years 1990-2004), (Zipfel et al., 2003).

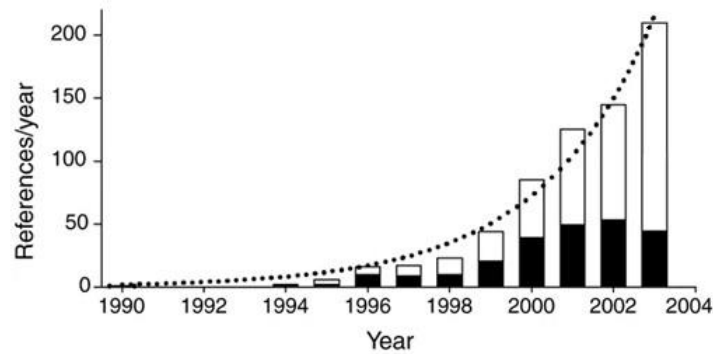


Figure 8 Publications related to multi-photon microscopy (instrumentation development -black-; usages to improve biological research -white-), (Zipfel et al., 2003)

Here there is a simple calculation of commonly used mean and peak intensities for a femtosecond pulsed laser: considering a pulse width $t_{pulse} = 100 \text{ fs}$, a repetition rate (pulses frequency) $R = 80 \text{ MHz}$ and a mean power at the sample $P_{mean} = 10 \text{ mW}$, this means one can reach a peak power

$$P_{peak} = \frac{P_{mean}}{t_{pulse}} \frac{1}{R} > 1,2 \text{ kW}$$

sufficient for the process to occur.

- Another interesting point is directly related to the photons' energies involved in the process: since the molecule is now excited by two quanta of light, the energy they should transmit is approximately the half with respect to a single photon, meaning red shifted wavelengths. Considering the Rayleigh scattered light intensity dependence on the wavelength λ ($I_{scattered} \propto 1/\lambda^4$), the use of red and infrared illumination light ensures a bigger penetration depth (down to about 1 mm), with respect to blue shifted one-photon light, that is more scattered.
- Looking back at the cross-section equation, transitions between initial and final states with the same parity are allowed: that's because two-photon process contains two dipole terms that make it an even function. Thus, there is a non-null transition probability to the excited states even when there is zero probability of direct transition, meaning impossibility for one-photon excitation occurrence: this fact implies that some fluorophores, not excitable via one-photon, can be accessed by the two-photon process.

All these advantages make the technique particularly adapt and advantageous for in vivo imaging of small animals, with an optimal spatial resolution and reduction of photodamage. Combined with a galvo system for a fast scanning, an adequate temporal resolution can be reached too.

2.3 Recording neuronal activity with calcium sensors

Calcium is an element exploited in different processes such as neurotransmitter release from nerve terminals, muscle contraction, cell migration; moreover it has a fundamental role in signal transduction coming from the activation of ion channels; in particular an incoming action potential depolarizes the synapses and results in opening voltage-sensitive calcium channels allowing these ions to move into the neuron: calcium then increases the probability that a synaptic vesicle will release the transmitter into the synaptic cleft. The greater the amount or frequency of action potentials, the more calcium enters the cell.

Calcium imaging techniques take advantage of so-called calcium indicators, fluorescent molecules responding to the binding of Ca^{2+} ions with a change in their fluorescence properties. For example, the binding of Ca^{2+} ion to a fluorescent indicator molecule can lead to either an increase in quantum yield of fluorescence or emission/excitation wavelength shift. An example is reported in Figure 9 where the two different two-photon spectra of the calcium dye GCaMP6m, respectively bound to calcium and free, are depicted (Barnett et al., 2017).

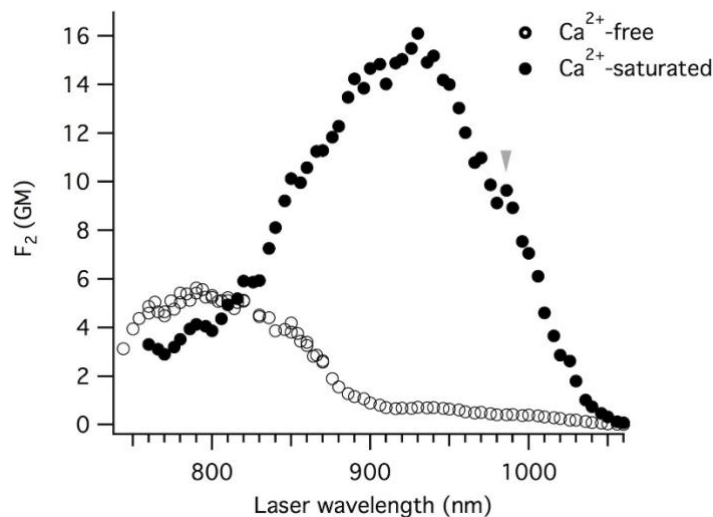


Figure 9 Two photon excitation spectra of GCaMP6m are presented as a linear combination of the two individual two-photon action cross-section spectra (Barnett et al., 2017).

When the endoplasmic reticulum releases the calcium ions into the cytosol, they bind to these signaling proteins that are thus activated; to notice, in the cytosol calcium is only shortly active, suggesting a very low free state concentration, instead when inactive it is mostly bound to organelle molecules (like calreticulin).

There exist two main classes of calcium indicators:

- *Chemical indicators*: these are small molecules that can chelate calcium ions. They are all based on an EGTA homologue called BAPTA (a chelating agent that has high selectivity for calcium ions Ca_{2+} versus the magnesium ones Mg_{2+}). Frequently used chemical indicators are Fura-2, Indo-1, Fluo-3, Fluo-4, Calcium Green-1.

These dyes are often used with the carboxyl groups of the chelator masked as acetoxymethyl esters, in order to make the molecule lipophilic allowing it to enter easily into the cell. Once it is inside, cellular esterases will free the carboxyl groups and the indicator will be active to bind calcium. The original free form of the indicator can also be directly injected into cells, targeting also specific compartments: this can have the advantage of removing uncertainties of dye localization, since the acetoxymethyl ester can also enter the endoplasmic reticulum and mitochondria.

- *Genetically encoded indicators (GECI)*: they don't need to be loaded into the cell since their encoding genes can be easily transfected to the lines. It is also possible to have transgenic animals expressing the dye in all cells or selectively in certain cellular subpopulations. GECIs are engineered from green fluorescent protein (GFP) or its variants (for example circularly permuted GFP, YFP, CFP), fused with calmodulin (CaM) bound with M13 domain of the myosin light chain kinase. Another option is to fuse variants of GFP with troponin C (TnC), a protein that can bind with calcium, and the mechanism of FRET (Foerster Resonance Energy Transfer) is applied for signal modulation. (M. Z. Lin & Schnitzer, 2017).

The first real time Ca_{2+} imaging was performed in 1986 in cardiac cells (Cannel et al., 1987), later development of the technique revealed sub-cellular Ca_{2+} signals in the form of Ca_{2+} sparks and Ca_{2+} blips, thanks to laser scanning confocal microscopy. A combination of chemical Ca_{2+} fluorescent indicators was also used, evaluating their relative response, to quantify calcium transients in intracellular organelles such as mitochondria.

Chapter 3

Optogenetics

Optogenetics is a stimulation technique based on the expression, in the cell membrane, of light-sensitive proteins that, upon illumination, alter the electric state of the neuron; it's a fundamental step forward in neuromodulation and, thanks to its combination of optical and genetic tools, spatial and temporal control of biological systems can be achieved, with a specificity unreachable by other methods like electrical stimulation or pharmacology (Boyden et al., 2005). In the past decade it has transformed the neuroscience field, offering new insights into neurologic diseases and future possibilities for applications in clinical settings.

Some early attempts to drive intracellular change with light exploited lasers to ablate proteins in signaling pathways (for example the receptor Ptc in the Hedgehog pathway of *Drosophila* embryos), (Schmucker et al., 1994) or to turn them on (for example targeting axons to stimulate action potentials), (Hirase et al., 2002). Only later light stimulation was started to be coupled with genetic manipulations, such as the targeted expression of *Drosophila* arrestin-2, rhodopsin, and a G-protein subunit in rat hippocampal neurons (chARGe strategy), (Zemelman et al., 2002); other attempts were focused on the expression of the ligand-gated ion channels P2X2 and TRPV1 with versions of their agonists, chemically modified to make them biologically inert and reactivable only after exposure to ultraviolet radiation (Lima & Miesenböck, 2005). These possibilities brought to applications ranging from mapping neuronal circuits to clinical implications such as restoring vision and ameliorating Parkinsonian deficits (Boyden, 2011).

The problem with these initial attempts was that neuronal activity could only be induced very slowly, and still targeting specific populations of neurons was difficult; the limited penetration depth was another limiting factor in targeting neuronal populations. A way to overcome these disadvantages was discovered in a class of light-sensitive ion channels called microbial opsins: since microbes have no complex organs, they developed these molecular sensors for the visible light in order to perform homeostatic functions such as maintain osmotic balance in seawater (Stoeckenius, 1985). Microbial and algal opsins have the property of sensing electromagnetic radiation and consequently transducing it into transmembrane ion flux actuating an intracellular change: thus, representing the optimal candidates to investigate light-stimulated induction of neuronal activation, they were largely studied in the mid-2000s.

3.1 Engineered light-based actuators

Conventional optogenetic effector or actuator tools can be classified into two big families, microbial opsins (type I) and animal opsins (type II); they can be genetically introduced into cells where they induce neuronal firing in response to light. The genes from both opsin families encode seven-membrane structures, ion channels that require retinal as a cofactor, a molecule closely related to vitamin A, which undergoes isomerization after the absorption of a photon: when the two molecules are bound together, the retinal isomerization brings to a conformational change in the opsin itself, initiating transmembrane ion movement. Thus, exposure to light of the proper characteristic wavelength results in a transient peak photocurrent, followed by a lower stable plateau for channel desensitization (Nagel et al., 2003); channels recover in the dark after a time constant (τ_{off}), again characteristic of each opsin.

The first opsin to be isolated (from *Halobacterium halobium*) was bacteriorhodopsin proton pump (Lozier et al., 1975; Oesterhelt & Stoerkenius, 1971); its characteristic wavelength is $570nm$, green. But for decades its potentiality in controlling intracellular activity were not fully appreciated, until the advent of light-activated neuronal stimulation techniques that renewed the interest on the microbial opsins. Nagel et al. soon isolated a similar proton pump, channelrhodopsin-1 (ChR1), from the primitive pigmented eyespot of the algae *Chlamydomonas reinhardtii* (Nagel et al., 2002); soon after, channelrhodopsin-2 (ChR2) was isolated from *C. reinhardtii*: it's peak absorption is at approximately $460nm$ and the characteristic time constant is $18ms$; these made it the perfect candidate for reliably driving neuronal spiking (Nagel et al., 2003), and from there on it was largely used in many optogenetic studies.

Excitatory Opsins

ChR2 was the first opsin to be introduced as single-component optogenetic tool, enabling temporal control of neuronal activity on the millisecond scale (Boyden et al., 2005). The discovery in vertebrate tissues of large quantities of retinal cofactor permitting opsin to be expressed as a single component (Deisseroth et al., 2006; F. Zhang et al., 2006) encouraged many groups to engineer opsins through codon optimization in order to permit a more consistent expression in mammalian tissues, a modulation of the activation time course varying ion conductance properties, a different light wavelength of activation. Beginning with the introduction of the H134R mutation into ChR2 (Gradinaru et al., 2007; Nagel et al., 2005) that has improved the size of steady-state current at the expense of temporal precision, further work has been performed to enhance opsin functions:

- To achieve higher levels of expression, endoplasmic reticulum export motifs were added to ChR2 (Gradinaru et al., 2008)
- A chimeric combination of ChR1 and ChR2 was created in order to decrease photocurrent falloff due to prolonged light stimulation (ChEF, 33% inactivation vs 77% for ChR2); a further mutation was engineered to speed up channel closure permitting higher-frequency stimulation (ChIEF), (J. Y. Lin et al., 2009).
- ChETA, with its destabilized active conformation of retinal, allowed for faster spontaneous re-isomerization to the inactive state (Gunaydin et al., 2010).

- Step function opsins (SFOs) yielded bistable activation with a prolonged activity after the light stimulus, up to a time constant of 29 minutes with the advanced stabilized step function opsin (SSFO) (André Berndt et al., 2009; Yizhar et al., 2011). SFOs have also the property to be able of inactivation by a pulse of green (542 nm) light, which causes retinal reisomerization to the inactive state; thus, SFOs represented the first “on-off switch” to control neural activation with light.
- The identification of VChR1 (from *Volvox carteri*) opened the path to red-shifted activation wavelength opsins (F. Zhang et al., 2008). Later, ReaChR has been engineered as a ChIEF and VChR1 hybrid to achieve improved plasma membrane expression in mammalian cells and higher photocurrents than other red-shifted opsins; the big advantage is given by the red excitation wavelength around 590 – 630nm, less absorbed and scattered by tissue ensuring an optimal tissue penetration (J. Y. Lin et al., 2013).

Inhibitory Opsins

Inhibitory opsins have not a so extended optogenetic toolkit as for excitatory ones. The first light-sensitive ion pump succeeding in neuronal spiking inhibition was a chloride channel isolated from the halobacterium *Natronomonas pharaonis*, NpHR; it is maximally activated by yellow light at 573–613nm (F. Zhang et al., 2007).

- Enhanced halorhodopsins eNpHR2.0 and eNpHR3.0 improved NpHR membranetrafficking (Gradinaru et al., 2008, 2010).
- Other potential inhibitory opsins were identified in proton pumps from different species: eBR from *Halobacterium*, Arch from *Halorubrum sodomense*, ArchT from *Halorubrum* strain TP009, and Mac from *Leptosphaeria maculans*. A 3–5-fold increase in photocurrent was achieved with membrane trafficking-enhanced versions (eArch3.0, eArchT3.0, eMac3.0), (Mattis et al., 2012).
- The ChR1–ChR2 chimeric version of C1C2 engineered to conduct chloride ions instead of cations (iC1C2) was created for inhibition with the usual blue light (Kato et al., 2012). SwiChR resulted from the alteration of iC1C2 kinetics to resemble the SFO step-function-like properties: it is an inhibitory chloride channel enabling stable and reversible neuronal inhibition with red light (Andre Berndt et al., 2014).

3.2 Applications

Not only the optimization of opsins is important, but also the development of delivery technologies to express them *in vitro* and *in vivo* is fundamental.

For both applications, viral delivery systems have been widely used to transfer opsin packages to cells thanks to their high infectivity, low toxicity and easy of production with standard equipment. This expression can be achieved by three methods (Hamblin & Avci, 2015):

Viral vectors. Vectors to deliver the opsin gene into the host cell genome were successfully identified in lentiviruses and adeno-associated viruses: the aim is achieved with a recombinant virus by fusing the gene with a cell-specific promoter; in this way the vector delivers the transgene in the host cell, where it is incorporated into the genome. This system has the advantages of a fast implementation and high expression levels over long periods; at the same time a disadvantage is given by the payload capability, since viruses lower specificity limiting the possible length of the promoter sequence.

Transgenic animals. To obtain a transgenic line one needs first a transgene cassette, consisting in a promoter and a transgene. This is then injected into zygotic eggs, mice or rats and integrates randomly into the host cell genome, achieving expression with a specificity driven by the promoter. This technique overcomes viral payload limitations allowing the use of larger promoters to confer greater specificity; moreover, the level of expression in transgenic animals is highly uniform. Many different transgenic, opsin-expressing organisms were developed (Fenno et al., 2011): *Caenorhabditis elegans*, *Drosophila*, zebrafish, rat, and, most prominently, mouse.

Cre-dependent expression system. The Cre-dependent expression system consists in a combination of both viral and transgenic methods with the production of a transgenic line that expresses Cre-recombinase in the target cells; it uses a Cre-dependent virus carrying an inverted opsin fusion gene, designed to deliver opsins in specific cells when activated by Cre: when transduced into cells expressing Cre-recombinase, the fusion gene is irreversibly inverted allowing cell-specific gene expression of the opsin (F. Zhang et al., 2010). In this case gene expression depends on the co-expression of Cre-recombinase, therefore even if cells may be infected, if not present the Cre-recombinase, there won't be any opsin expression.

In Vivo Applications

Relevant early developed works in different animal models are reviewed below, focusing on the first applications of optogenetics in these different models (Fenno et al., 2011). More recent works are summarized instead in chapter 4, filtered by focusing on an all-optical implementation.

Thanks to the easy quantification of *Caenorhabditis elegans* body-wall contraction and elongation, many studies were performed on this model: control of muscle wall motor neuron and mechanosensory neuron activity were mainly performed (Nagel et al., 2005; F. Zhang et al., 2007). Moreover, a vast investigation of different mutant strains for synaptic protein defects (Liewald et al., 2008; Stirman et al., 2010) and nicotinic acetylcholine receptor function (Almedom et al., 2009) was performed. Finally, all-optical physiological experiments, combining both stimulation and readout with light, were conducted in this model (Guo et al., 2009; Tian et al., 2009). Another interesting animal for optogenetics is the *zebrafish*, given its short generational time and the easy integration of foreign DNA combined to the organism transparency itself. The first use in this animal examined the role of somatosensory control of escape behavior (Douglass et al., 2008); later, using lines with eNpHR-enhanced yellow fluorescent protein (eYFP) and ChR2-eYFP expression controlled by the Gal4/UAS system, specific neuronal subtypes targeting was achieved, opening the path for many interesting biological studies (Arrenberg et al., 2009). Other groups have examined cardiac function and development (Arrenberg et al., 2010), transduction of sensory neuron mechanoreception (Low et al., 2010), command of swim behavior (Arrenberg et al., 2009; Douglass et al., 2008), and saccade generation (Schoonheim et al., 2010). From a technical point of view, photoconverting

proteins Kaede and Dendra were used to study the light spread, observing that this neural targeting combined with the use of a small-fiber permits the stimulation of a spot around 30μ -diameter.

One of the most used model in this field, thanks to its easy genetical accessibility, is the *drosophila*: exploiting expression of upstream activation sequence (UAS):ChR2 (W. Zhang et al., 2007), flies were fundamental to investigate the neuronal basis of the nociceptive response (Hwang et al., 2007) and appetitive/aversive odorant learning at both receptor and neurotransmitter level (Bellmann et al., 2010; Schroll et al., 2006); moreover studies were performed to rescue photosensory mutants (Xiang et al., 2010). Additionally, Gal4/UAS targeting of ChR2 to the larval neuromuscular junction system was demonstrated (Hornstein et al., 2009). Many other creative uses of optogenetic tools in *drosophila* were performed, for example the validation of neurons identified in a screen to probe the proboscis extension reflex (Gordon & Scott, 2009), driving monoamine release to validate fast-scanning cyclic voltammetry detection of serotonin and dopamine (Borue et al., 2009), and the investigation the innate escape response (Zimmermann et al., 2009).

Another important animal model in this field is the mouse: mice represent the majority of transgenic animals and are the most widely published optogenetic model organism. Mouse embryonic stem cells have also been used in this field (Stroh et al., 2011). The first study using channelrhodopsin in behaving mammals focused on the contribution in sleeping and wakefulness of hypothalamic hypocretin (orexin) neurons (Adamantidis et al., 2007). Mice have also been used to investigate amygdala circuits involved in fear and anxiety: ChR2 was used to demonstrate that lateral amygdala pyramidal neurons are sufficient in auditory cued fear conditioning (Johansen et al., 2010); functional circuits within the central amygdala were further delineated, demonstrating that distinct subpopulations of inhibitory neurons separately drive conditioned fear (Ciocchi et al., 2010; Haubensak et al., 2010); finally, the differential effects in regulating anxiety behaviors while activating lateral amygdala projections onto central amygdala neurons, were described (Tye et al., 2011). Optogenetic modulation in mouse was also used to control monoaminergic systems: for example ChR2, eNpHR2.0, and TH::Cre transgenic mice were used in modulating bidirectionally the locus coeruleus neurons, showing that consequently sleep and arousal states were strongly modulated (Carter et al., 2010); mechanisms underlying dopamine-modulated addiction were investigated (Brown et al., 2010), and it was shown that cholinergic interneurons of the nucleus accumbens can modulate cocaine-based place preference (Witten et al., 2010); the connectivity of striatal medium spiny neurons has also been described (Chuhma et al., 2011). Studies in mouse cortex and hippocampus enabled the understanding of complex mammalian neural circuit dynamics with direct optogenetic modulation of principal and local-circuit inhibitory neurons: reports on the parvalbumin expressing fast-spiking interneurons functions demonstrated their involvement in gamma oscillations and information processing in mouse prefrontal and somatosensory cortex (Cardin et al., 2009; Sohal et al., 2009); fast functional mapping of motor control across the motor cortex was also achieved in Thy1::ChR2 mice with a focal stimulation of pyramidal neurons (Ayling et al., 2009; Hira et al., 2009), and the mapping of projection patterns in callosal cortical projections was possible by axonal stimulation in contralateral regions with respect to the injected cortical areas (Petreanu et al., 2007). The spatial receptive fields of various neuron types (Kätzel et al., 2011; Petreanu et al., 2009; H. Wang et al., 2007) and the basic properties of cortical disinaptic inhibition (Hull et al., 2009) were also studied. Optogenetics was also applied in mouse models of depression to investigate the possible therapeutic mechanism of cortical intervention (Covington et al., 2010) and to develop novel strategies for peripheral nerves control (Llewellyn et al., 2010).

Other mammals are also used for optogenetic experiments, such as rats: blood oxygen level-dependent (BOLD) responses in functional magnetic resonance imaging (fMRI) were studied with virally delivered optogenetic: a BOLD response was driven by ChR2 in excitatory neuronal populations not only in local cortical targets but also in downstream thalamic regions, allowing to obtain global maps of specific cell population activity within intact living mammals (Lee et al., 2010). Insights into diverse physiological functions was performed too: for example, modulation of rhythmic beating activity in rodent cardiomyocytes was achieved, demonstrating the potential for applications in this field (Bruegmann et al.,

2010); moreover, modulation of cardiovascular function, breathing, and blood pressure in both anesthetized and awake rats are largely performed (Abbott et al., 2009; Alilain et al., 2008; Kanbar et al., 2010).

Finally studies on primates are less spread: attempts to assessing viral vector efficiency were conducted in rhesus monkeys and safe expression of the opsin was proved in macaque too (Diester et al., 2011; Han et al., 2009). Optogenetic efficacy on physiological measures was also shown by eNpHR2.0 delivered to human neural tissue in the form of ex vivo human retinas; this has an interesting relevance for retinitis pigmentosa, a disease in which retina light-sensing cells degenerate; normal phototransduction as well as center/surround computational features, directional sensitivity, and light-guided behavior could be restored by manipulating light-insensitive cone cells with the expression of eNpHR2.0 (Busskamp et al., 2010). Additionally, the functionality of ChR2 in human embryonic stem cell-derived neurons was demonstrated (Weick et al., 2010).

Chapter 4

All-optical implementation

Optogenetics is used with different stimulation tools and in combination with many readout methods; for example, a huge amount of studies was performed with a wide stimulation by lamps or LEDs, most of the time looking at the response at a behavioral level or with common tools of electrophysiology. A general illumination like this provides a less specific activation, targeting all the neurons expressing the opsin; an improvement can be done choosing collimated sources like lasers, best at all two-photon lasers. At the same time the readout method can be more or less resolved, for example behavioral studies gives only a specific kind of information, while to study neuronal response in detail better techniques are electrophysiology or calcium imaging. Still the first one, largely used, is useful to reach single cell resolution, with the drawback of a lack of precision in targeting specific cells and a huge limitation in study whole network activity; on the contrary calcium imaging is an appropriate candidate to overcome all these limitations.

Thus, the idea would be to use an all-optical setup, exploiting the light both to stimulate the neurons (thanks to optogenetics) and to read out their response (with calcium imaging); this approach was largely pointed as an ideal tool in neuronal investigation, but at the same time many technical drawbacks, intrinsic on this combined approach, characterized its application until now (Packer et al., 2015): this is due to some practical limitations arising from the use of the two techniques in combination, that make the setup harder to implement. Apart from the cost effectiveness of having two lasers (particularly for two-photon lasers or holographic implementations for a more complicated patterned stimulation), the biggest problem arises from molecules spectra overlap. In particular, calcium sensor excitation spectrum and opsin activation spectrum have to be considered. In principle, the activation profile of the optogenetic molecule should be spectrally separated from the calcium sensor one, in order to avoid any neuronal activation while imaging. However, some degrees of freedom can be gained playing with different imaging and stimulation powers, resulting in an effective procedure (activating the opsin only with a higher and spreader power, thus not while imaging) even in presence of some spectral overlap. Moreover, many different solutions were developed in these years, engineering different molecules with a huge variety of spectra. For example, as reported in Chapter 2.2, the most used sensors in transgenic animals are GECIs: at the moment, one of the most common and efficient sensor is GCaMP6 (even if recently a new improved version -GCaMP7- was developed (Dana et al., 2019)), which has an excitation spectrum covering the blue wavelength and an optimal excitation wavelength coincident with that necessary to activate one of the most common opsin, ChR2 (470 nm with one-photon, 940 nm with two-photon). As anticipated, many different molecules were consequently engineered, like red-shifted calcium sensors that can be excited with green light, or shifted opsins as well (as reported in Chapter 3.1); the disadvantage in this approach is that these molecules are generally less efficient than the GCaMP or ChR2 families, with lower response signal, lower resting state signal, lower activation rate. The main works performing an all-optical approach are listed below, explicating the efforts they did to overcome these technical limitations.

- Different works provide a combination of two-photon activation with two-photon imaging, overcoming the problem of overlap with a red-shifted opsin.
 - One of the most recent examples was performed by Marshel et al. studying orientation-specific ensembles of mouse cortical layers: they used multiplexed multiphoton-holography to stimulate a red-shifted opsin in combination with two-photon calcium imaging (Marshel et al., 2019). Yang et al. characterized a similar setup for a volumetric imaging in mouse (Yang et al., 2018) and Mardinly et al. performed a similar approach too, with a custom soma-targeted opsin (Mardinly et al., 2018). Foerster et al. set up an all-optical two-photon toolbox using GCaMP combined with ChrismonR in larval zebrafish (Förster et al., 2017). Zhang et al. created a closed-loop setup, with a direct activation of cells under threshold (Z. Zhang et al., 2018); even before, Packer et al. were able to activate specific neurons in mouse with a such setup (Packer et al., 2015) and Rickgauer et al. performed experiments in hippocampal place cells during spatial navigation of mice (Rickgauer et al., 2014). On the contrary, Forli et al. tried to perform single cell stimulation varying also the calcium sensor, using jRCaMP, a red-shifted one, not overlapping with ChR2 (Forli et al., 2018). Also other works adopted this option, studying larval zebrafish's circuit driving motor behavior (dal Maschio et al., 2017).
- Other few works were oriented to one-photon stimulation, exploiting different techniques to solve overlapping problems.
 - Recently Saber et al. estimate the connectivity in *in vitro* rat neurons using a red-shifted calcium sensor (Saber et al., 2018); Braubach et al. activated single glomeruli in mouse, imaging with a blue shifted molecule (Braubach et al., 2018); Kim et al. oriented towards a red-shifted opsin to study the activity of different brain areas perturbed by optogenetics mimicking natural pattern in freely moving mice (C. K. Kim et al., 2016) and a similar approach was performed by Zhang et al. to inhibit neurons in *C. Elegans* too (Y. P. Zhang & Oertner, 2007). Bovetti et al. exploit an inhibitory opsin in combination with GCaMP in mouse (Bovetti et al., 2017). Highly interesting it is a very recent contribution given by Huang et al., in which they performed such an all-optical approach for one of the first time in *Drosophila* brain with a red-shifted opsin (Huang et al., 2019).
 - If all these works just reported above tried to overcome the problem of overlap using different types of molecules with not overlapping spectra, very few works performed an all-optical protocol with the highly efficient ChR2 and GCaMP molecules. Recently Conti et al. followed this approach to study intra hemispheres correlation in mouse, exploiting a separated path for the two sources and the targeting of different areas of stimulation and imaging, spatially separated to avoid signal crossing (Conti et al., 2019); Szabo et al. already before demonstrated the possibility to use this combination of molecules to control alive mice, reducing crosstalk playing with different powers of stimulation and imaging (Szabo et al., 2014), and similarly Guo et al. reconstruct functional connectivity between different groups of neurons in *C. Elegans* (Guo et al., 2009). Similarly, previous works were performed by Wilson et al. and Zhang et al., respectively in mouse and *C. Elegans*, studying inhibitory neurons (Wilson et al., 2012; F. Zhang et al., 2007). Such an approach was performed also in zebrafish by Helmbrecht et al. to study the behavioral functions of different classes of projection neurons connecting tectum to premotor areas (Helmbrecht et al., 2018).

From the previous review it is clear that the works adopting an all-optical approach are relatively not so numerous despite their usefulness, moreover a cost effective one-photon stimulation is occasionally investigated. Interestingly also the fact that all these works are performed mainly on mice or *C. Elegans*, and with a combination of molecules that never adopts both the most performing sensors together. To our knowledge, only the previous cited work (Huang et al., 2019) has already applied such an approach to *Drosophila in vivo*, an animal model full of advantages both from a genetical point of view, easy to genetically manipulate, and for its size, small enough to study an entire brain down to cellular level; still, this is not performed with ChR2 and GCaMP combination.

Thus, in this work, we will show for the first time the possibility to apply, for a functional connectivity experiment, the combination of some of the most advantageous characteristic in an optogenetic experiment:

- cost effective blue laser stimulation
- high resolution and penetration depth with two-photon calcium imaging
- combined use of two of the highly efficient molecules for optogenetics (ChR2-XXL and GCaMP6)
- study of a whole brain of an *in vivo* *Drosophila*

Part II

Experimental work

Chapter 5

Materials and methods

5.1 All-optical setup

The optical setup consists of a two-photon microscope combined with a femtosecond pulsed Ti:sapphire laser, whose output power can be controlled by a Pockels cell. The beam is scanned in the plane by galvo-mirrors and the laser beam is focused onto the sample through a water-immersion objective. Focus is controlled by the height of the objective which can be varied using a motor and a piezo-electric device. The emitted light coming from the sample is collected in an epi-geometry and, after being separated from the excitation light, detected by photomultiplier tubes. The scan and the reconstruction of the images are controlled by the software PrairieView. The complete setup is placed on the Newport *RS4000™* optical table with vibrational isolation via laminar flow. An additional diode laser (473nm) is collimated in the same optical path in order to stimulate the opsin. Let's see in details the main characteristics of the different components; a simplified schematic of the setup is shown in Figure 10 and Figure 11.

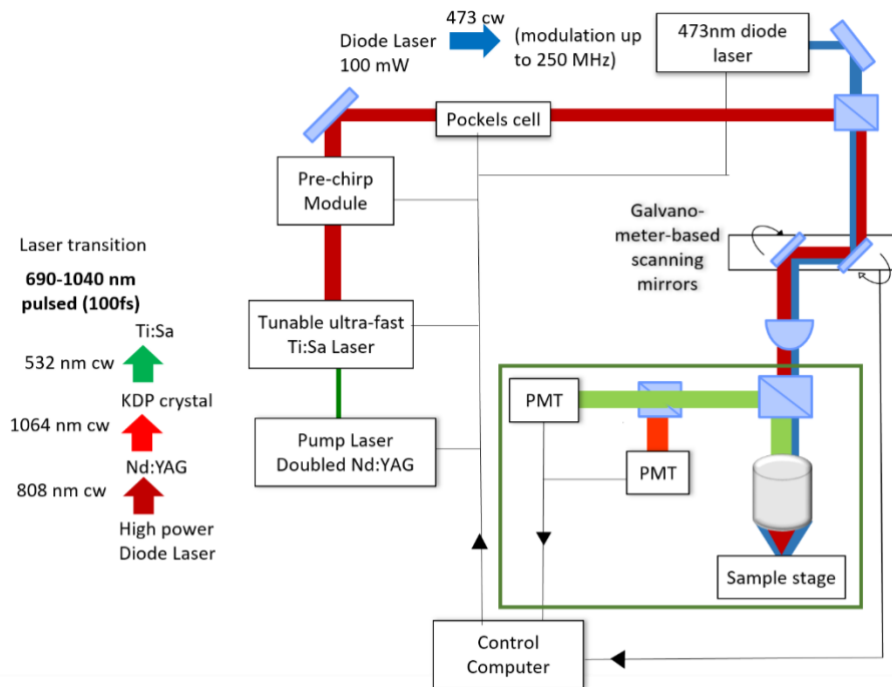


Figure 10 Scheme of the setup

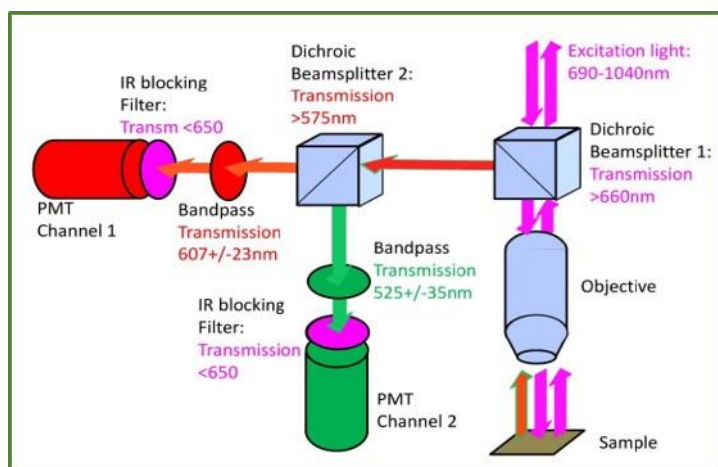


Figure 11 Scheme of filters and PMTs

Imaging laser

The excitation source is the Spectra-Physics MaiTai® DeepSee™ mode-locked Ti:sapphire laser, integrated with the Spectra-Physics 14 W Millennia® Nd:YAG pump laser. Its wavelength is tunable in the range 690–1040nm. It provides an average power > 2.5W, with a peak power > 425kW (at 800nm). At 800nm the obtained pulses have a width < 100fs and a repetition rate of 80MHz (± 1 MHz). Spectra-Physics MaiTai® DeepSee™ laser introduces pre-compensation, which corrects in advance for the dispersion caused by transmission through the optical path (that lengthens the pulses) allowing the maximum fluorescence signals to be observed.

Pockels cell

The Pockels cell (*Conoptics*) is an electro-optic modulator which can be used to modulate the power of the laser beam. It is based on the Pockels effect: first described in 1906 by the German physicist Friedrich Pockels, this effect consists in the linear variation of the refractive index of a non-centrosymmetric material with respect to the strength of an applied electric field. This is caused by forces that distort the position, orientation or shape of the molecules constituting the material. Combined with other optical elements, in particular with polarizers, Pockels cells can be used as amplitude modulators: the change in the polarization state of the transmitted beam (due to the change of the refractive index of the material) and the subsequently transmission through the polarizer permit to change the optical amplitude and the delivered beam power. In this setup, the applied electric field can be changed by the operator through a parameter (that will be called p-parameter) present in the microscope software. The Pockels cell is very sensitive to environmental variations (such as temperature variation).

Laser optics

A big problem with a short light pulse is that when it passes through a dispersive material such as glass, it becomes ‘chirped’; the longer wavelength components travel faster so the pulse width lengthens. In the visible and near-IR region, all materials have positive dispersion (red leads blue), so that femtosecond pulses passing through optics are always ‘positively chirped’ and thus longer than they were directly out of the laser. Positive dispersion can be offset by adding negative dispersion before the beam travels through the optics. This is known as dispersion compensation, or prechirping and in our apparatus is achieved using a prism pair system. The intensity of the laser is controlled using a pockels cell combined with polarizer element, this configuration guarantees very fast switching (ns) and a good extinction rate, however the

pockels cell suffer of temperature dependence of the birefringence. The laser beam is scanned on the sample using a galvano-meter based scanning mirrors system where two mirrors can be precisely tilted allowing for X-Y scanning. The z-axis can be scanned using a step-motor to move the objective up and down.

Activation laser

The chosen laser is a research grade diode laser produced by Toptica Photonics with emission wavelength at 473nm and a maximum output power of 100mW . In the next table there are the nominal characteristics of the laser.

Wavelength	473nm
Maximum output power	100mW
Beam diameter	1mm
Divergence	<1mrad
Pointing stability	<5urad/K
Polarization	>100:1, linear
Analog modulation	1MHz
Digital modulation	250MHz
RMS noise	< 0.2 (10Hz – 10MHz)

The laser was furnished with a dock for fiber coupling and two input port for analogical and digital control. Being a diode laser, the output power can be modulated directly controlling the pumping current with a theoretical maximum modulation frequency of 1MHz for analogical modulation and of 250MHz for digital modulation. The laser was connected through the analogical port with the control computer in order to automatically control the power and the on/off switching using a simple voltage input between 0 and 5V. The laser was coupled with a single mode fiber (TM00) and brought inside the 2P microscope box.

Using two tilting mirrors and a dichroic one the activation laser was carefully aligned on the same optical path of the 2P laser. This implies that the activation is spatially modulated using the same scanning box of the imaging part. Some apparatus uses two different sets of scanning mirrors for the activation and the imaging part and this allows performing an imaging scan even during the activation protocol. However, this solution was much more expensive. The dichroic mirror before the objective lets light of 473nm to pass and a notch filter before the PMTs prevents the 473nm scattered light to reach the PMTs.

During the imaging part the scanning mirrors have to quickly scan all the position in the field of view or along the scanline, while during the activation they have to stop at discrete points where the activation takes place. The time speed is guaranteed by a high switch box produced by Bruker.

Microscope

We used Prairie Ultima In Vivo two-photon microscope (*PrairieTechnologies*), mounted inside a box to prevent noise coming from ambient light. The laser beam entering the optical path of the microscope can be scanned in the xy plane through a pair of 3mm galvo-mirrors (*CambridgeTechnologies*), which are mirrors controlled by a galvanometer, an instrument that converts an applied electric current in a magnetic moment; mirrors rotate because of this effect and the reflected laser beam is consequently deflected. The two-photon microscope is equipped by a water-immersion objective ($20\times$ NA 1.0, *Olympus*). The focus can be controlled changing the height of the objective: the microscope has a standard z-motor device, with a travel range of 25mm and $0.01\mu\text{m}$ minimum step size, and a z-piezo device with a travel range of $150\mu\text{m}$ and $0.1\mu\text{m}$ step size. The microscope is designed for epifluorescence collection: the emitted light coming from the specimen passes through the objective and encounters a primary dichroic beam-splitter (cutting off at 660nm , *ChromaTechnology*) which separates the emitted UV-VIS light from the back-scattered

excitation IR light. Then, the emitted light beam is filtered by an IR-blocking filter (shortpass at 650nm) and is divided by another dichroic beam-splitter (cutting-off at 575nm) before encountering the two detectors. Both detectors are Hamamatsu Multialkali PMTs and are preceded by two different band-pass filters (*ChromaTechnology*): one is a $607/45\text{nm}$ filter (channel 1, red), the other a $525/70\text{nm}$ (channel 2, green).

Software

The scan and the reconstruction of the images are controlled by the software PrairieView. With this software it is possible to set the imaging working conditions: the spatial resolution (from 64×64 to 2048×2048 *pixel*), the field of view (optical zoom, rotation), the dwell time, the laser power (varying the voltage applied to the Pockels cell through the p-parameter), the excitation wavelength, the sensitivity of the detectors (varying the voltage applied to PMTs). Moreover, it is possible to control the position of the sample in all the three spatial coordinates during live scan. The software gives also the possibility to perform z-series, which are collections of images at different depths (choosing the driving device, motor or piezo, and given the initial and final positions and the step size), and more complicated t-series that connect different operations in time sequence. Signals are collected from Ch1 and Ch2, images are automatically reconstructed pixel by pixel and data saved as different TIFF images. All the chosen imaging parameters (from laser wavelength to dwell time, parameter, pixel resolution, etc. for each sequential image) are saved in an XML file. Collected images were processed with Matlab framework (*MathWorks*) for background subtraction, intensity normalization and more advanced analysis (better explanations are reported in paragraph 4.6).

5.2 Setup characterization

Here I report the power calibrations for our two lasers, the blue diode laser for opsin activation and the two-photon laser at 940nm. The powers are calculated for different values of reference, referring to arbitrary units used in our control software, ranging from 0 (minimum power) to 1000 (maximum power). Power values are measured with a power meter at the exit of the objective, thus they don't correspond to the effective power arriving at the sample focal plane, since this depends strongly to the depth of imaging and tissue scattering.

Usual working powers were around 150 software control a.u. for the blue laser and 200 software control a.u. for the two-photon, meaning powers of respectively less than 0.05 mW and about 1 mW at the sample.

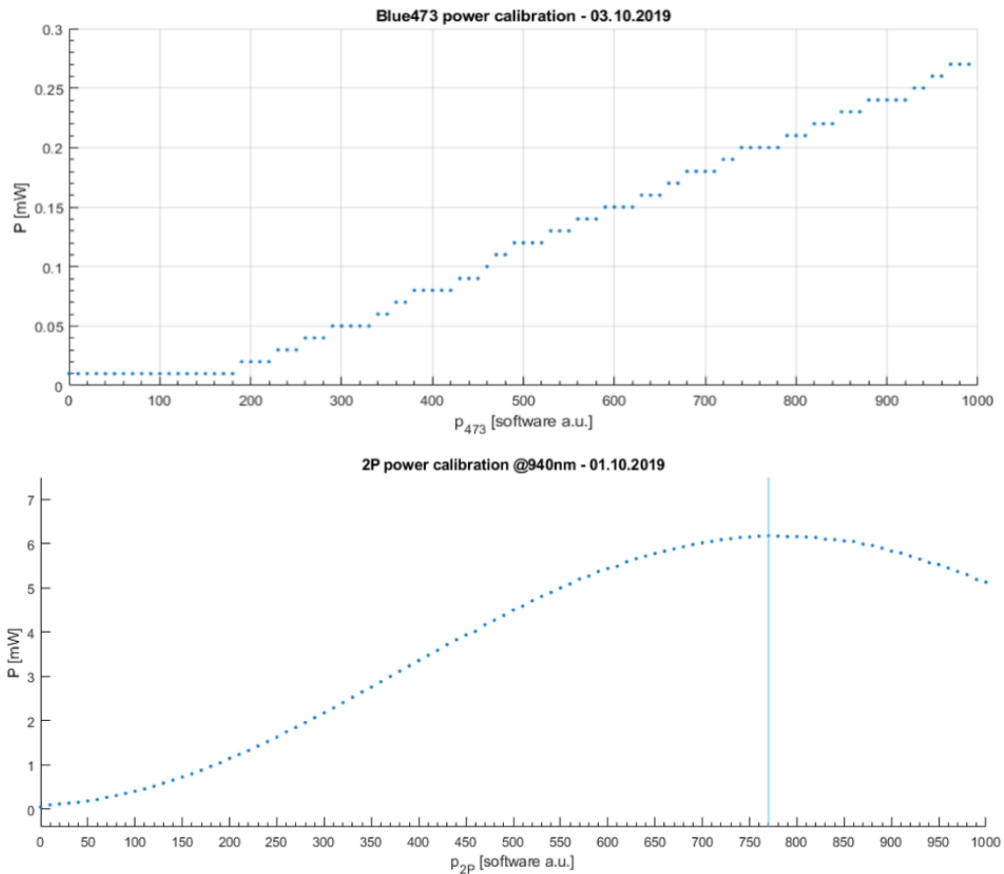


Figure 12 Laser power calibration curves. The units on the x axes refer to a scale from 0 to 1000 of arbitrary units of the microscope software.

We can notice from the two-photon calibration curve that the maximum power reachable is around 6 mW; this is due to a beam partial suppression happening before the Pockels cell, in order to limit the maximum power delivered at the objective focal plane. In practice, it is possible to increase this value.

Secondly, we checked the alignment of the blue laser with the infrared one, in order to be sure that the reference of our stimulation points corresponded precisely to the expected position in the two-photon field of view. To perform this task, we've used a glass slide colored with a yellow fluorescent marker and we've bleached specific points with the blue laser at high power. In this way we could check the difference between the point position set with the software and the effective spot position (given by the bleached hole in a reference image acquired with the two-photon microscope); thus, it is eventually possible to rearrange the coordinates of blue laser spot position by software for a perfect coincidence with the effective spot.

The final result can be shown in Figure 13, where the reference positions of the blue laser spots (red circles) are set properly in correspondence of the effective bleached spots in the two-photon image of the yellow marker layer. In this case a grid of 25 points was used, where for every point the blue laser was opened at relative high power (about 0.12 mW at the sample) for 500ms.

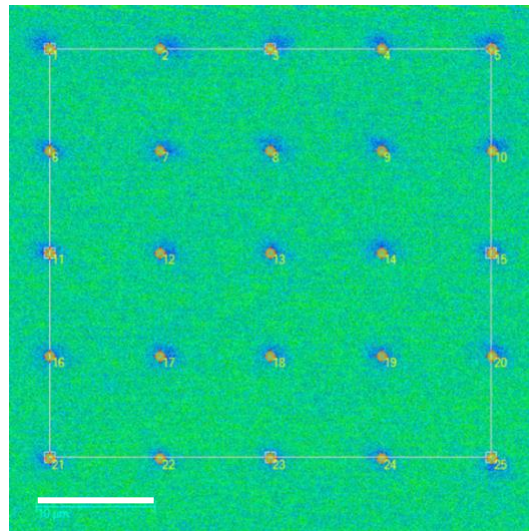


Figure 13 Lasers alignment procedure. A two-photon image of a yellow marker layer is taken as reference and some points are bleached with the blue laser (0.12 mW at the sample, 500ms): the coordinates of the points can be adjusted by software in order to fit perfectly the effective hole positions. Scale bar 10 μm .

In this way we are sure that the two beams are properly aligned in the plane, since to a given galvo setting corresponds the same point at the field of view for both the laser beams. This procedure doesn't involve the z-alignment that can be optimized only by acting on the manual alignment of the beams.

Finally, an estimation of the blue laser spot was performed, in order to infer an order of magnitude on the blue beam dimensions. Again, for an easy quantification, a homogeneous marker sample was used to be bleached, with parameters set as previously.

An idea is given in Figure 14, in which the bleaching spot on the fluorescent sample is visible, reporting some images at the extremities of the spot and on the focal plane. What we can infer from here is that the blue laser has a point spread function that indicatively doesn't exceed the $5\mu\text{m}^2$ in the plane and has an extension of less than $20\mu\text{m}$ in the axial direction.

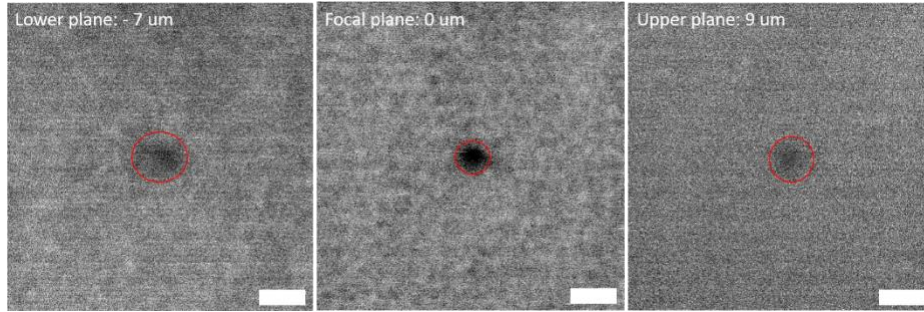


Figure 14 Bleaching spot by the blue laser at different planes (lower -7um, focal 0um, upper 9um). Scale bar 5um.

The stimulation spot is clearly improvable with a two-photon laser, that would be more confined (order of less than 1um in the plane) and less scattered in the tissues (since working with infrared wavelengths), permitting to reach a specific single cell stimulation. Nevertheless, we can say that together with genetical selectivity we can still expect to reach a high precision in stimulation with these beam characteristics, particularly we can notice that the illumination spot can be confined in a glomerulus volume (the subunit of the antennal lobes) that has typical dimensions of 20um for fruit flies.

5.3 HEK cell lines

In order to perform preliminary optimization experiments, cells were co-transfected with calcium sensor and opsin. Starting from the vectors pcDNA3.1/hChR2(H134R)-mCherry and pGP-CMV-GCaMP6m, different lines of HEK293 cells were co-transfected with GCaMP6 and ChR2:mCherry, so that the specific expression could be checked thanks to its fluorescence signal in two different channels (red for opsin and green for calcium sensor). An example is reported in Figure 15; as it is visible the co-expression doesn't reach a 100%, instead some cells present only GCaMP expression, some other only the opsin and about 20% have both the constructs.

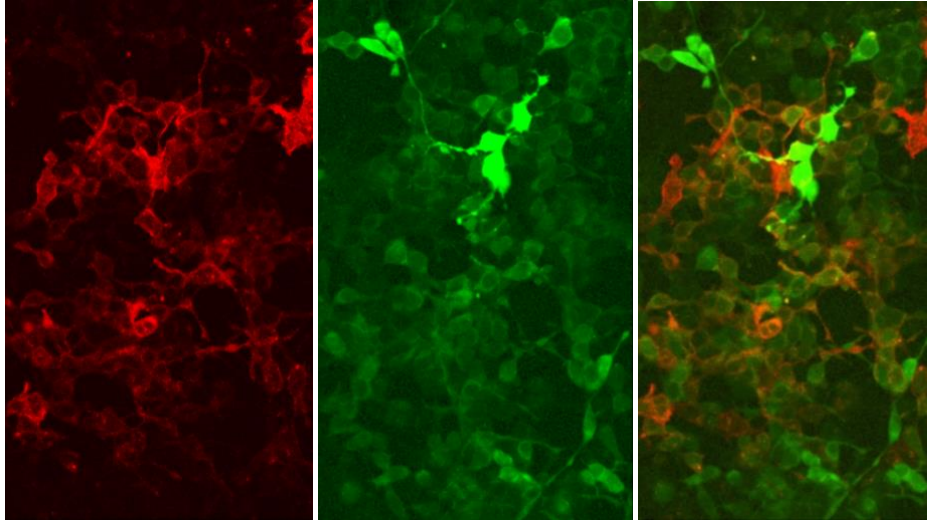


Figure 15 HEK cells expressing opsin ChR2:mCherry (red, left); calcium sensor GCaMP6 (green, middle); the right figure represents the merge.

The transfection followed a standard procedure:

1. One day before transfection cells were plated in 500 μ L of growth medium without antibiotics, 40-45% confluent. This allows to obtain 70-90% confluence at the time of transfection.
2. Plasmid is diluted in 50 μ L of medium, mixing gently. Lipofectamine is diluted in 50 μ L of medium and incubated for 5 minutes at room temperature. Just after, these are combined together and incubated at room temperature for 20 minutes.
3. The complexes are added to the well containing the cells with medium and mixed gently.
4. Cells are incubated for 18-48 hour at 37°C 5% CO₂.

The idea to use cells as a starting point was thought to test the setup and handle a simpler model than a living insect; the availability of the HEK293 and their characteristic to be strong and resistant cells brought us to choose them for our preliminary experiments. Other works have already shown the possibility to induce current changes in HEK following optogenetic stimulation of ChR2, in particular light activation of this molecule was found to cause depolarization of 10-25 mV within 10 ms and repolarization within 200 ms, thus capable to elicit action potentials (Li et al., 2005; Venkatachalam & Cohen, 2014).

5.4 Insect preparation and drosophila lines

Insect preparation

The sample preparation and drosophila brain exposure procedure were adapted from previous works (Silbering et al., 2012).

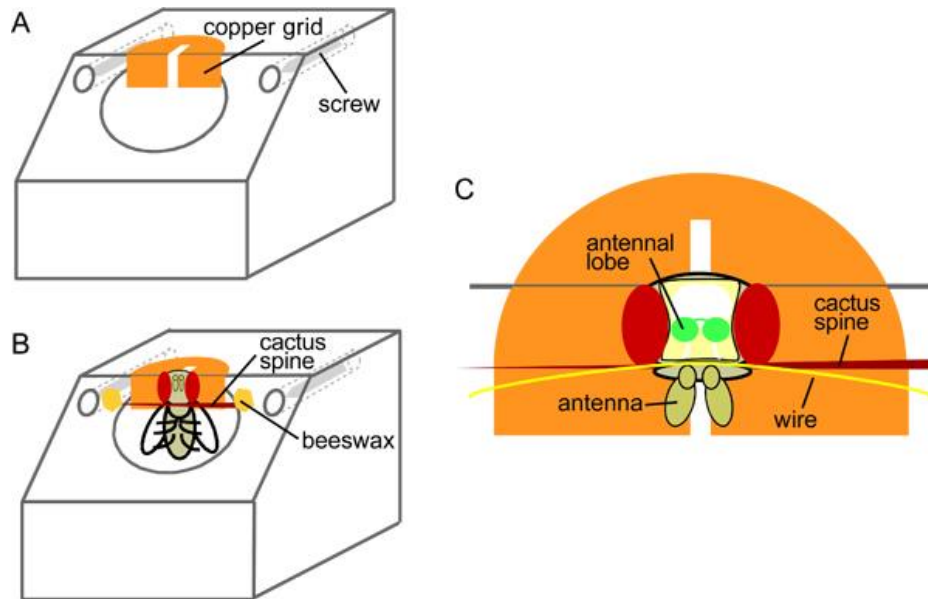


Figure 16 *Drosophila* preparation protocol (Silbering et al., 2012). In figure A it is visible the mounting block with the copper grid fixed; figure B shows the fly blocked by the neck and in figure C a view from the top shows the separation of the antennae from the head complex.

1. Customized plexiglass mounting blocks were used to allow easy mounting and dissection of the fly, blocking the animal by the neck. A copper grid is fixed and leveled on the block to create a “collar”, with the slit centered on the hole of the block. Both grid flaps have to be glued on the inclined front of the block so that the slit is pointing straight downwards (45°) (see Figure 16A and Figure 17).
2. Flies of the appropriate genotype are anesthetized by cooling on ice, female are chosen for their bigger dimensions. Holding the fly by the wings it can be introduced into the mounting block sliding its neck along the slit of the copper grid and rotating it until it is looking down. When the surface of the head is at the same level with the top surface of the block, the fly is blocked in that position with a cactus spine in front of its proboscis to prevent it from moving; the head is completely fixed with drops of glue on the sides (Figure 16B and Figure 18 left).

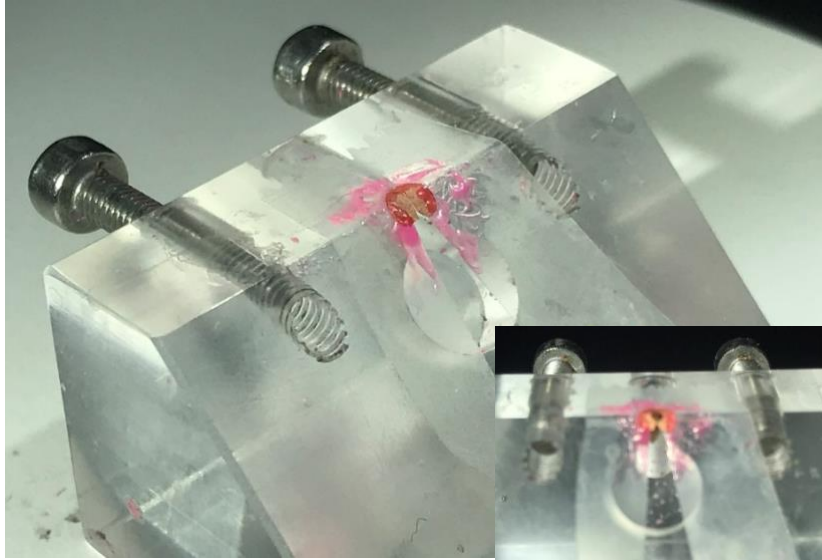


Figure 17 Image of a mounting block with the copper grid used to fix drosophila by the neck.

3. After assembling a wire holder with a plastic coverslip making a "U" shape and a piece of wire across the top of the "U", the antennae of the fly are pushed creating some space between the antennal plate and the head, with the help of this wire inserted in the cuticular fold between head and antennae; to push the wire gently the screws built into the block are used for fine forward movements (Figure 16C and Figure 18 top right).
4. At this point an antennal shield, composed by a hole in a not-sticky piece of tape surrounded by a plastic cover slip, is placed on the top of the head; the hole should be of the dimensions of the head itself, not extending beyond the eyes to prevent preparation from leaking and keep the antennae completely dry (Figure 18 bottom right).



Figure 18 The drosophila is blocked with a cactus spine (left), the antennae are pushed by a wire (top right) and covered with a plastic shield (bottom right).

5. The hole between the tape and the cuticle is sealed with two-component silicon, in a thin layer; a drop of Drosophila Ringer's saline (130 mM NaCl, 5 mM KCl, 2 mM MgCl₂, 2 mM CaCl₂, 36 mM saccharose, 5 mM HEPES, pH 7.3) is then placed on the head.
6. At this point it is possible to cut the cuticle using a sapphire blade, performing a cut along the eyes and across the ocelli on the back. Finally, after removing gently the piece of cuticle, glands and trachea are removed too with fine tweezers, and the drosophila is ready to be observed.

Drosophila lines

For our experiments we created some basic stable lines, in order to express the molecules in specific neurons of interest; in particular we obtained:

- UAS-ChR2-XXL/Cyo; LeXAop-GCaMP6m/TM6b
- UAS-GCaMP6f/Cyo; LeXAop-ChR2-XXL/TM6b
- nSyb-LexA/CyO; orco-GAL4/Dr
- GH146-LexA/CyO; orco-GAL4/TM6b

It was not possible to obtain stable lines already co-expressing opsin and calcium sensor; however, crossing these basic lines, the desired result is obtained. Thus, performing these crosses, it is possible to have drosophilae expressing the calcium sensor pan-neuronally and the opsin at the level of receptor or projection neurons. In particular GH146 will drive an expression at the level of PNs, orco in the olfactory neurons, nSyb in all neurons. The labels Cyo, TM6b, Dr represent the phenotype (curly wings, hairy fly and thin eyes respectively).

Crosses were performed with a standard procedure: drosophilae are stored, separated by lines, in plastic tubes containing food. 2-3 virgin female are selected from one population and 2-3 male from the other one, and they are put together; after 5-7 days, when the eggs are laid, parents are removed and the eggs left growing. After 2-3 weeks the new drosophilae are born and can be selected according to the proper phenotype.

In our experiments we have tested mainly drosophilae with the genotype *Orco-GAL4/UAS-ChR2-XXL; nSyb-LexA/LexAop-GCaMP6m*; in Figure 19 an example of the molecules expression is presented in a dissected and stained brain, where it is clearly visible the expression of the opsin at the level of the antennal lobes (magenta in figure) and the calcium sensor in all neurons (green).



Figure 19 Image of a dissected and fixed fly brain, marked with antibody anti-ChETA (top left, magenta) for ChR2-XXL identification and anti-GFP (top right, green) for calcium sensor GCaMP identification. The opsin is expressed in the antennal lobes, GCaMP pan-neuronally. Bottom figure represents the merge. Scale bar: 100 μ m. (Damiano Zanini, private communication).

5.5 Experimental protocol

After sample preparation, the insect is directly ready to be put under the objective, immersed in the drop on the top of the fly head (Figure 20). We focused on the brain of the insect, identifying the different areas, in particular focusing on the antennal lobes. A good compromise between PMTs gain, laser power and dwell time was chosen in order to obtain a good signal with a high signal to noise ratio. In particular, relatively high PMT gain and low laser powers were set to have sufficient signal without releasing too much power to the sample, for the same reason relatively small values of dwell time were chosen gaining also in temporal resolution. Since our main goal was to monitor intensity profile in time, in most of the experiments we kept a low spatial resolution (generally 2D images at 128x128 pixels), reaching a significant time resolution of the order of 5 Hz.

Usual values of the different parameters used are reported in the following table:

Spatial resolution	128x128 pixels
Dwell time	8 μ s
Frame per second	3.5fps
Two-photon power	p200 = 1mW at objective
Blue laser (473nm) power	p150 = less than 0.02mW at objective
Imaging (2P) wavelength	940nm (optimized for GCaMP6)

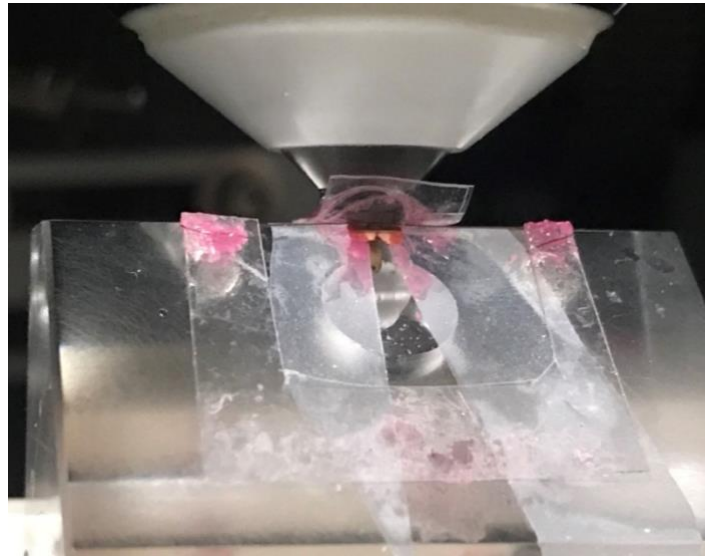


Figure 20 Example of a drosophila blocked under the microscope

5.6 Signal and response characterization

Neuronal responses to stimulation are calculated as change in fluorescence with respect to a baseline value F_0 (average fluorescence before stimulation), normalized to this same value, in order to obtain an absolute reference value:

$$\Delta F/F_0[\%] = \frac{F - F_0}{F_0} 100$$

In this way we can compare activations in different samples and subjects, evaluating a percentual variation from the resting state.

To understand what such a variation means, it is then useful to refer to the excitation spectra of the fluorescent marker used for the experiment. In particular we are going to perform two-photon calcium imaging with GCaMP6m/f (Chen et al., 2013); previously, in Figure 9, I've reported the two-photon cross-section for this molecule: as it is visible, focusing at a wavelength of about 940 nm, we obtain the maximum difference between fluorescence emission of neurons with low calcium concentration and high calcium concentration. This means that we would obtain a big change in fluorescence following neuronal activation; in particular, for this combination of marker and wavelength, an increment will correspond to the high calcium concentration configuration (active neuron). Thus, what we are going to expect in our signal computation, is an increase in percentual fluorescence variation following a neuronal activation, while a decrease (negative variation) can be interpreted as inhibition.

Another important point to consider is the stimulation contribution to the signal; since we switch between blue and two-photon laser, the activation source contribution to the signal can be completely removed from our data. In particular when the blue activation laser is opened the photomultipliers get saturated, thus we can clearly detect the corresponding frames and remove them from our intensity profile computation. An example of raw data is reported in Figure 21, where the saturation peaks are visible in correspondence of blue laser stimuli.

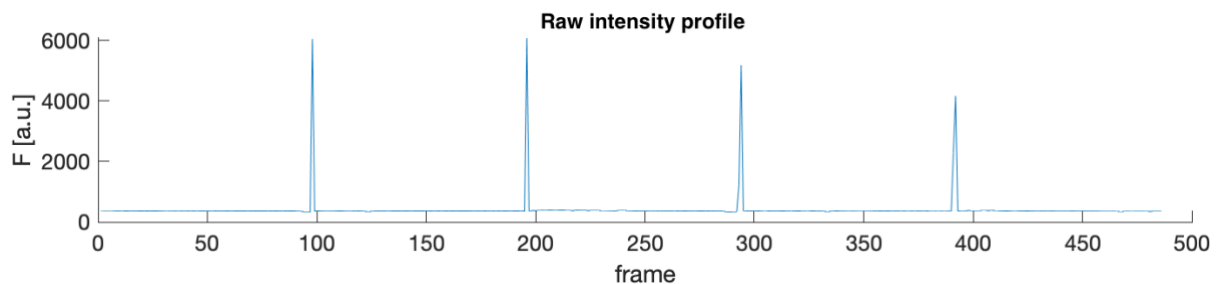


Figure 21 Example of raw data intensity profile with four blue laser stimulations. The frames in correspondence with the stimulation present saturated pixels and are clearly detectable (peaks in the profile); consequently they are removed to compute the final profile and analysis.

Furthermore, it is interesting to notice the kinetics of our sensor; some temporal characteristics are reported in Figure 22. We can see that for GCaMP6f/m (light blue and magenta lines) the response rise time is about 200-300 ms, while the decay time is of the order of 1s (clearly smaller for the fast variant), increasing also with the number of action potentials. These values are compatible with the timing scales of responses found in our experiments and ensure us to be able to detect a clear response also just after stimulation is ended, since the signal remains high for seconds.

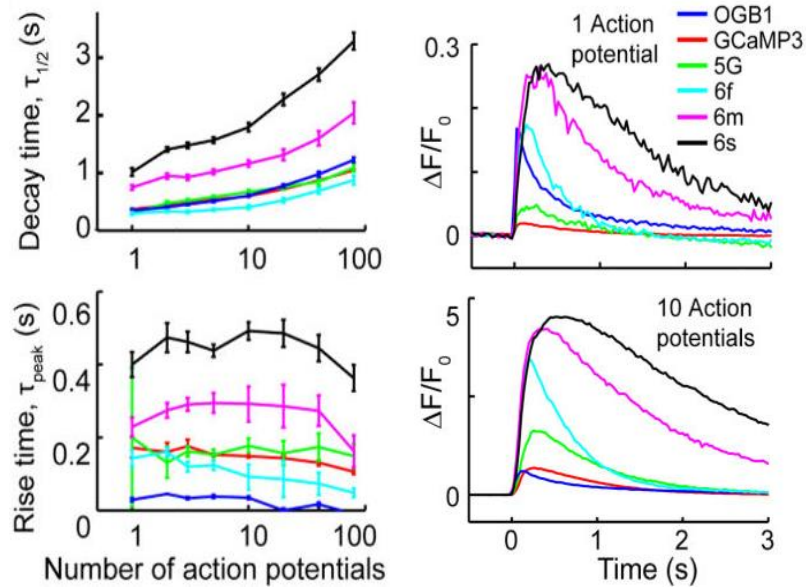


Figure 22 Decay time, rise time and fluorescence variation for different markers. Light blue and magenta are respectively GCaMP6f and GCaMP6m. (Chen et al., 2013).

5.7 Odorants characterization

In our experiments with odorants a series of 3 repetitions was presented with 3s of odor opening and 20s inter trial interval; the odorants we used were 1-hexanol, 3-hexanol, 1-nonanol, isoamyl acetate and acetophenone, already tested in drosophila (Fishilevich & Vosshall, 2005) and of interest to us for a possible comparative research with our previous work on honey bees (Paoli et al., 2018).

Odors were presented all together, mixed in a single presentation; they were used diluted at 1:200 and the concentrations were monitored with a photoionizer (miniPID, Aurora Scientific) at the level of antennae position; in particular in Figure 23 we report the normalized curves for the five odors, from which the arrival time of the odor at the insect antennae can be estimated (zero time refers to the opening of the valves).

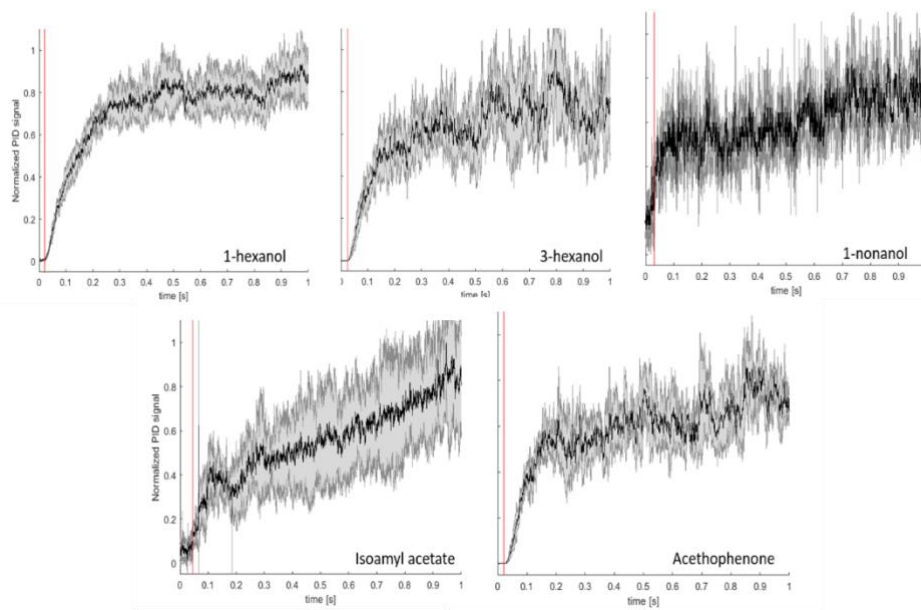


Figure 23 miniPID response curves for the five odorants (mean \pm SEM, $n = 5$). Red lines denote threshold criteria and onset points for odor concentration increase with respect to valve opening (for more details, Paoli et al., 2018).

5.8 Custom analysis software

Data were processed entirely with Matlab. A custom graphic interface was created in order to obtain a solid tool to perform all kind of analysis and investigations useful to extract information from the raw data in a fast way. A simplified flow chart of the app functionalities is reported in Figure 24.



Figure 24 Simplified flow chart of the custom Matlab app functionalities

In particular a first calculation of the fluorescence variation is computed, with background subtraction and stimuli individuation, together with a time-frequency analysis; more advanced correlation and cross-correlation analysis are then implemented.

I will present briefly the software designed in Matlab and subsequently the different correlation analysis performed on the data collected, to show the potentialities of our imaging toolbox. The software created is reported in Figure 25 and Figure 26.

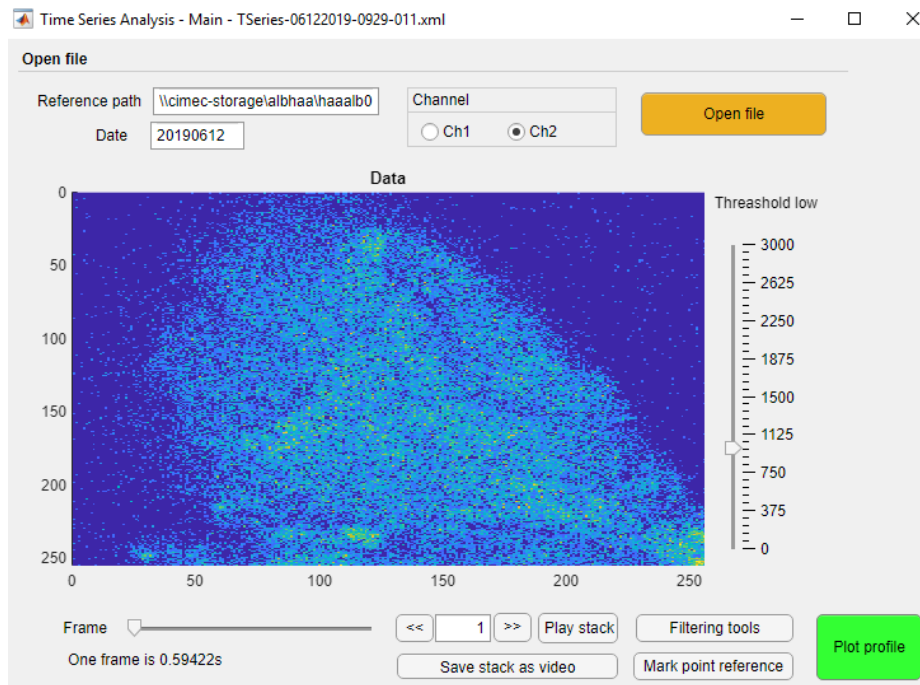


Figure 25 Analysis app layout, loading window

As it is visible, time series can be loaded and eventually filtered to remove pixels below a given threshold (more detailed filtering tools can be also applied in order to visualize image in a custom way). From these data the intensity profile and the power spectrum can be extracted (Figure 26).

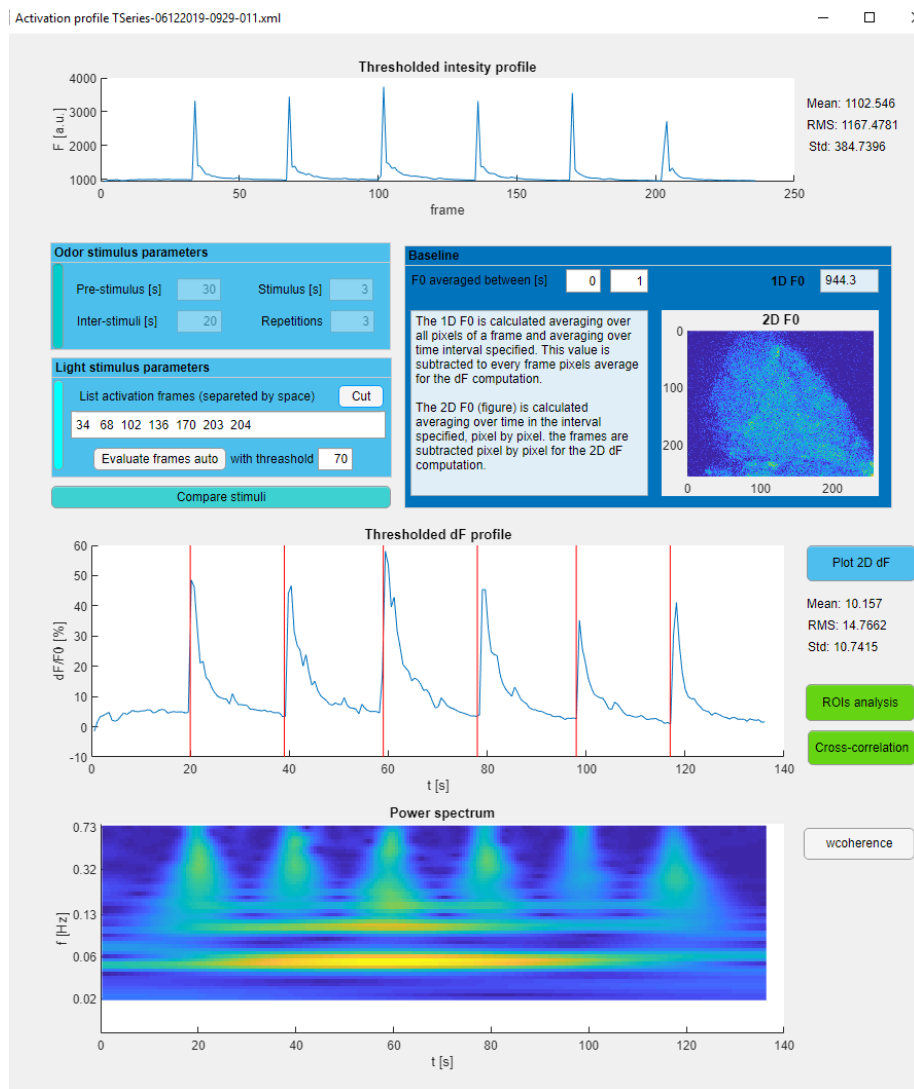


Figure 26 App layout, intensity profile and time-frequency analysis

In this section the raw profile is shown (upper figure), together with the modified one (middle), evaluated as percentual change in fluorescence, and considering the stimuli presentations. A power spectrum in the time-frequency domain is also computed (lower figure).

The reference fluorescence can be set choosing the time interval in which to average the signal to obtain the F0, and the fluorescence variation with respect to this value can be also visualized as 2D image. This tool is interesting to visualize pixel or areas more active in time, without losing information through ROI averaging.

Other interesting tools for a more detailed analysis are the ROIs and the cross-correlation ones. The first permits to select on the 2D image different regions of interest, from which to extract the intensity signal localized in that area; the signal can be reported like the general whole profile, as average over the different stimulations or separately for every stimulus. In these last two cases a new reference fluorescence F_0 is calculated for each stimulation, averaging over the frames just before the stimulus in a time interval selected by the user.

Every time, the program will report the chosen fluorescence variation for the selected ROIs and a correlation matrix between the given signals.

A more detailed study on correlation can be performed with the cross-correlation tool, with which, in an analogous way, different raw or averaged signals can be cross-correlated to investigate temporal delays in responses and correlations, and to infer information about signals directionality. A wavelet coherence analysis can also be applied to investigate coherence in time-frequency space with phase variations information between signals.

Some of these kinds of analysis are reported in paragraph 6.3.

Chapter 6

Results

6.1 Experiments on HEK cells

First trials were performed in HEK cells, in order to work on a simplified model. HEK293 cells were co-transfected with GCaMP6 and Chr2:mCherry, so that the specific expression could be checked thanks to its fluorescence signal in two different channels.

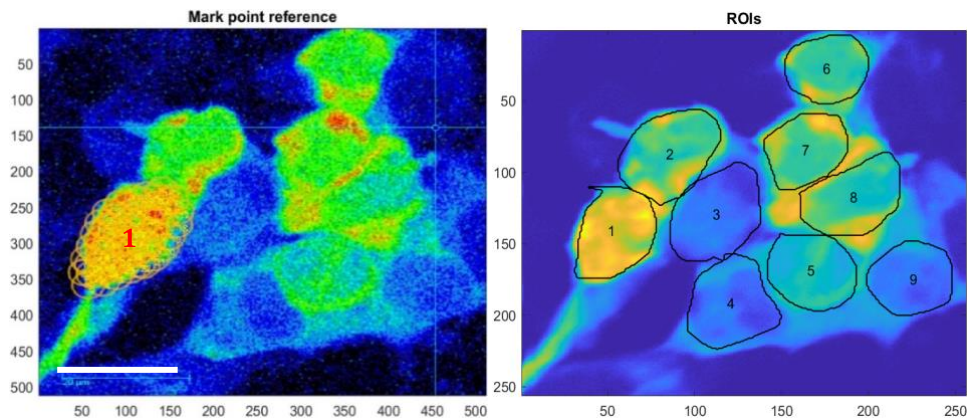


Figure 27 HEK cells activation protocol: activation points are depicted on the left (40 points inside one cell), while on the right different ROIs are selected. Scale bar 20 μm .

As a first attempt in order to activate these cells we performed many different stimulation paradigms with different number of stimulation points and durations. As first example I report a stimulation of a cell with 40 points for a total of 7s blue laser stimulation (with power at the objective $<0.01\text{mW}$), repeated for two times; how it is clear in Figure 27 (left), only one cell is pointed (this cell co-expresses both GCaMP and opsin), corresponding to ROI 1 in Figure 27 (right).

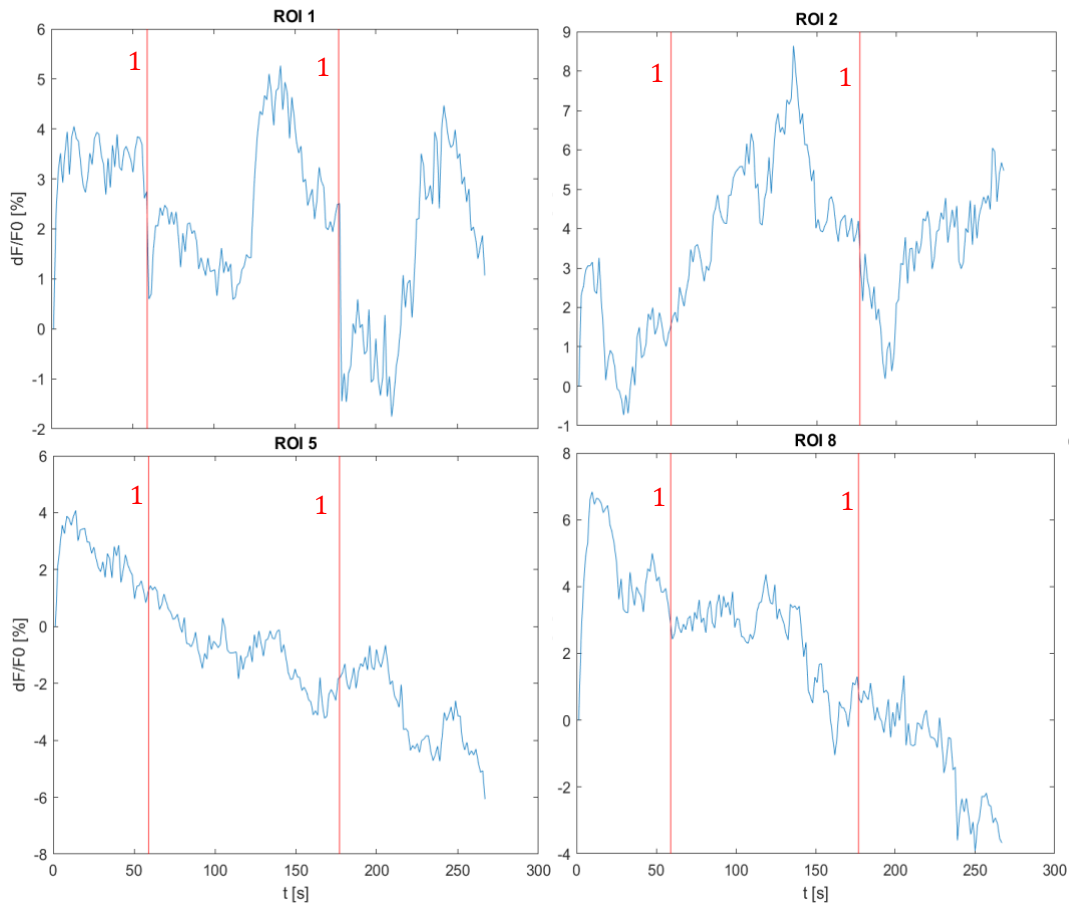


Figure 28 Fluorescence response (percentage in change of intensity) for different ROIs of Figure 27. Two set of 7s-stimulation were performed (the saturated stimulation frames were removed from the profiles where a red vertical line is depicted, indicating the stimulus occurrence).

The intensity profile for some of the ROIs is depicted in Figure 28, where it is visible the fluorescence variation in correspondence of the two stimulations (red vertical lines). Most of the cells seem not to show any significant variation, while the activated one exhibits a behavior clearly different from the others in correspondence of the two illuminations. Here, it is still hard to explain this behavior, since soon after excitation it seems there is a negative variation, maybe due to bleaching, but always followed by a fast increase; instead, another interesting increment that could mimic an activation can be seen after the first stimulation of ROI2 (neighboring cell to the activated one) . Anyway, this is a first preliminary step that suggests that something is happening in the cell expressing the opsin, after photo-stimulation, but still it's hard to give a clear interpretation of the behavior, lacking, in particular, repeated measurements.

After some attempts the stimulation points were optimized and decreased, in order to obtain the smallest stimulation capable of cell activation. In the following example only three points per cell were used, and two different stimulations were performed: the first one (at 30s) targets a cell co-expressing opsin and calcium sensor (ROI 1 in Figure 29 -right-), the second one (at 90s) illuminates a cell with only GCaMP expression (ROI 2 in Figure 29 -right-).

Looking at the results of Figure 30 it is interesting to notice how ROI 1 is highly activated by the correspondent first stimulus while this is not true for ROI 2 with the second stimulus: this could be properly expected since the second stimulation target cell 2 that doesn't express any opsin and thus it is actually not activated by blue laser stimulation. Similarly, a response can be found in ROI 3 (the first neighbor cell to the activated ones) that shows an increase only after first stimulation, i.e. subsequently the cell properly expressing the opsin is activated. Other cells, instead, seem not to have any significant response.

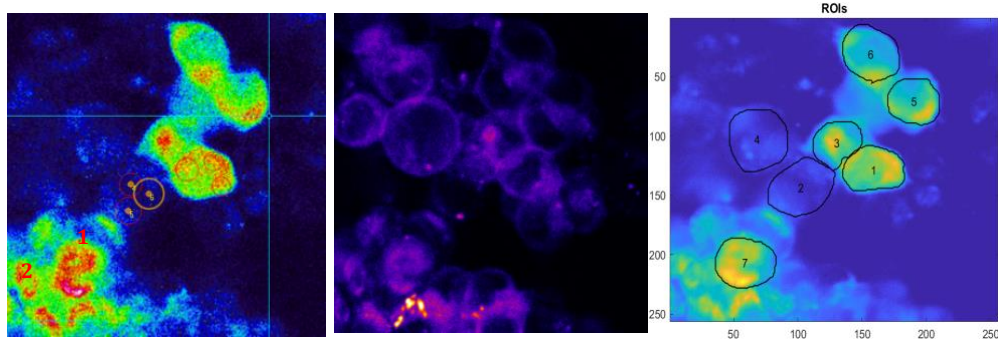


Figure 29 HEK cell stimulation protocol. Green channel (GCaMP, left), red channel (Chr2, middle), ROIs analyzed (right). On the left also the stimulation points are visible, three for ROI 1 (opsin and calcium sensor co-expressing cell) and three for ROI 2 (only calcium sensor expressing cell).

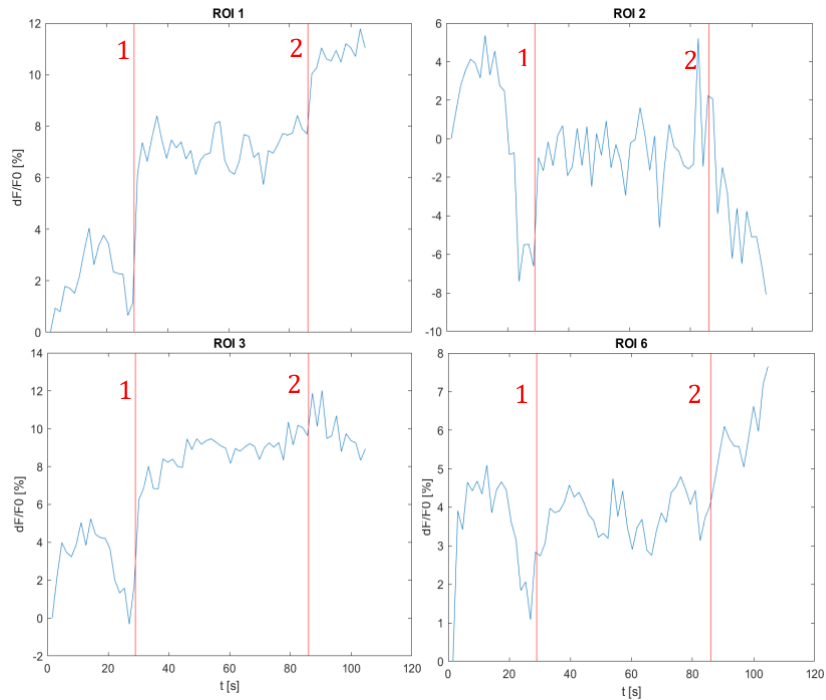


Figure 30 Fluorescence response for different ROIs of Figure 29. First stimulation (vertical line) targets the three points in ROI 1, cell co-expressing opsin and calcium sensor; second stimulation targets the three points in ROI 2, cell only expressing GCaMP.

These first experiments give us the bases to validate our setup, and to optimize parameters for a single cell activation. HEK cells are a good and simplified model for this purpose, even better could be the use of neurons to easily check also cellular connection.

Unluckily, we were not able to perform many experiments with these samples, since it took a long time to optimize the transfection in order to co-express the two molecules in a large amount of cells: what it was happening the most of the times was a complementary transfection, in which the main part of cells expressing the opsin (red cells in Figure 31 left) were not expressing GCaMP (green cells, middle) and vice versa; in fact it can be noticed from the merge (right figure) how the co-expression rate (yellowish area in the merge) is quite low, not permitting to perform numerous and repeated experiments.

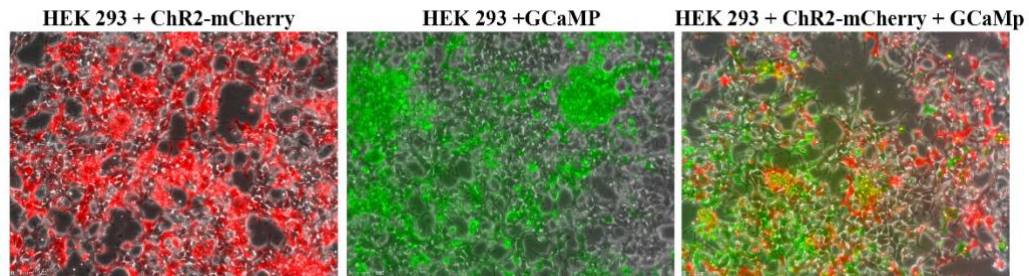


Figure 31 HEK cells expressing opsin (red, left) and GCaMP (green, middle). On the right the merge, with yellowish areas representing the co-expression. The co-expression rate is poor (less than 10%).

Moreover, further experiments with these samples were no longer doable, due to organizational bureaucratic limitations; there was no availability of other type of cell like neurons, as well.

Thus, a further and more detailed study on these cells and on neurons can be an interesting improvement in order to characterize better the setup from a lower level of complexity (with respect to animal models) and control parameters of the activation protocol.

Since the limitations we encountered and the availability of transgenic drosophila lines, we chose then to move directly on experiments with living flies.

6.2 Experiments on *drosophila*

I will report here some of the data obtained from our all-optical experiments on the *drosophila* brain, in which I will show how our setup can be used to stimulate specific areas of an intact brain *in vivo*, monitoring the activation over large areas. Later, in the next section, I will focus more on a deeper analysis that we performed applying different tools on these data.

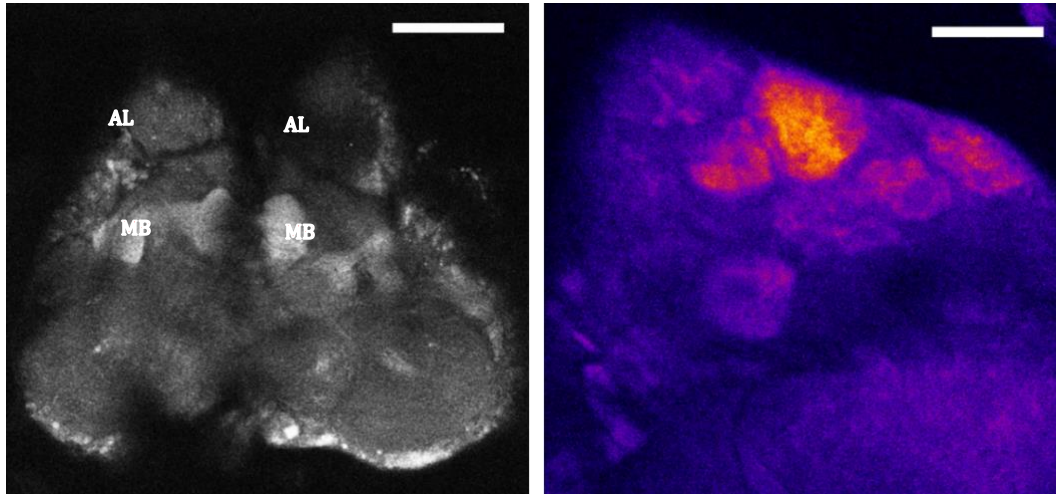


Figure 32 Example of resting state fluorescence (with GCaMP6 at 940nm) of *drosophila* whole brain (left) and antennal lobe (right). Scale bar: left 100 μm , right 20 μm .

In Figure 32 two examples of our samples are reported, a whole brain on the left and a zoom in the antennal lobe on the right. As it is visible, already with the resting state fluorescence of GCaMP6 at 940nm it is possible to identify specific regions of the brain, and in particular the glomeruli inside the antennal lobe are distinguishable. Images with this resolution (512x512 or 1024x1024 pixels) are taken only as reference, since during the acquisitions, to gain temporal precision, we perform scanning at lower spatial resolution.

6.2.1 Odor stimulation

As a first step to study responses *in vivo* we checked the glomerular activation following odorant presentation, in order to control the effective responsiveness of our drosophilae and have a reference activation signal.

I will report in the following discussion a few examples showing the change in fluorescence linked to odor presentation, looking at the response of the primary olfactory centers and their subunits, the glomeruli. The stimulus was presented as a combination of 5 different odors as discussed in the previous methods section 5.7.

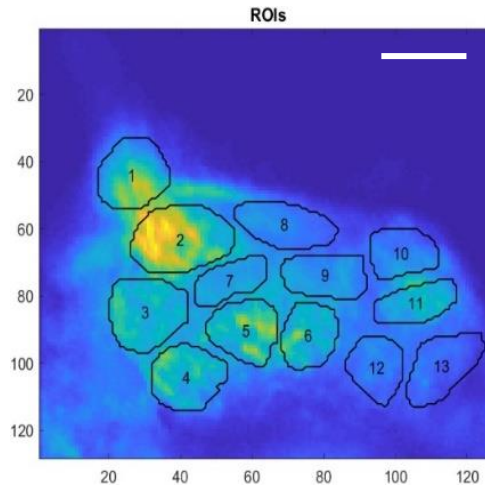


Figure 33 Reference ROIs corresponding to different glomeruli inside a fly antennal lobe. Intensity profiles for the different ROIs during odors presentation are reported in Figure 34. Scale bar 20 μm .

As it is visible from the profiles of Figure 34, a clear variation in intensity is detectable in specific areas of the antennal lobe in response to the odor mix presentation. In the figure, only some exemplificative ROIs are reported, sufficient to understand that the fly is alive and responsive, and odorant specific glomerular activation can be investigated.

In these data, for the odorant mixture presentation, it is interesting to notice how the response is different for different regions of the antennal lobe, including glomeruli not responding significantly (like ROI 1), glomeruli highly activated with a change in percentage bigger than 50% (ROI 9,11) and glomeruli that seem to show an inhibitive behavior (negative variation, ROI 2,4). Moreover, between the activated glomeruli, different response timings are detectable, with responses that are more peaked and extinguishing faster (ROI9) or longer lasting activations (ROI 8).

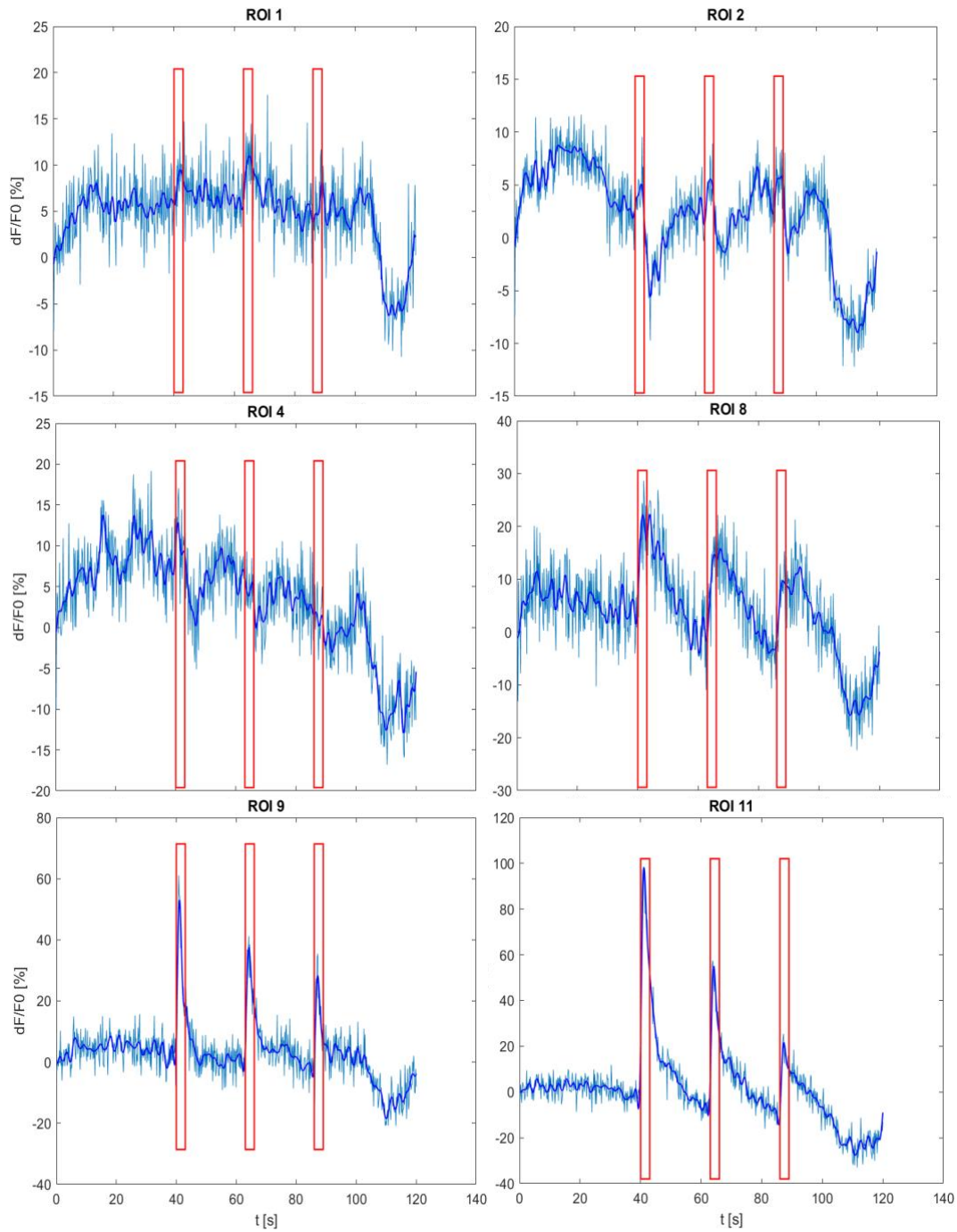


Figure 34 Intensity profile of fluorescence variation for different ROIs of Figure 33 during an odor mix presentation protocol. The red rectangles represent the odor presentation.

Other considerations can be done comparing the previous Figure 34 showing the response of different areas to odorant mixture, with Figure 36 reporting the same glomeruli activated by a presentation of 1-hexanol only. It is already well known how different odorants elicit characteristic glomerular response, as it is visible in the example of Figure 35 (J. W. Wang et al., 2003).

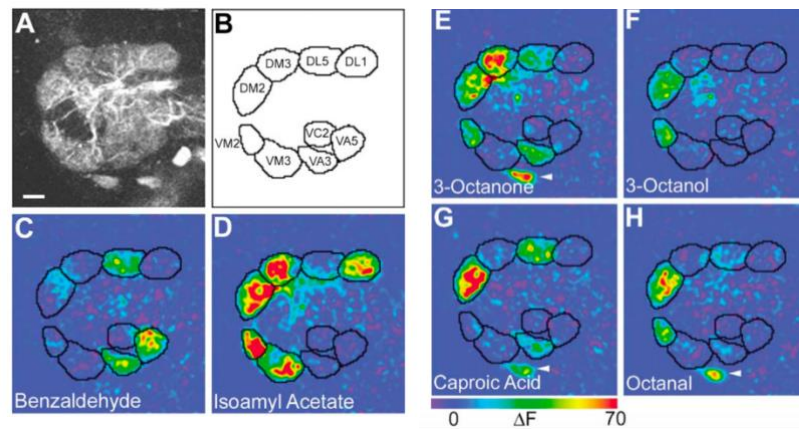


Figure 35 Different odors elicit different patterns of glomerular activation in the AL. Scale bar 10 μm . (J. W. Wang et al., 2003).

I've reported in the following (Figure 36) an example to show how some glomeruli can respond very similarly to different compounds (e.g. ROI 11), while other have a completely different behavior.

Another consideration about odor response can be done regarding data in Figure 37 where an average profile for two regions is reported: ROI 1 is inside the antennal lobe, comprehending glomeruli that have, in this example, an overall inhibitive behavior; instead ROI 2 is at the outer border of the antennal lobe, where glia cells are present and in this case there is a clear positive activation.

These examples show the possibility of monitoring a response to odor stimulation in the brain of the flies at different levels of complexity, particularly focusing on the different behavior of the glomeruli: this opens the possibility to a study similar to the one already performed in our group with bees (Paoli et al., 2018).

At this point, we still have some issues with odor responses, since not all the flies are always responsive (even if in most of the cases they still show a neuronal activation following blue laser stimulation); thus, at the moment, it was not possible to perform a systematic study to construct an odor map of glomerular activation: it will be interesting to optimize and complete this, in order to obtain a solid dataset to compare with optogenetic recordings.

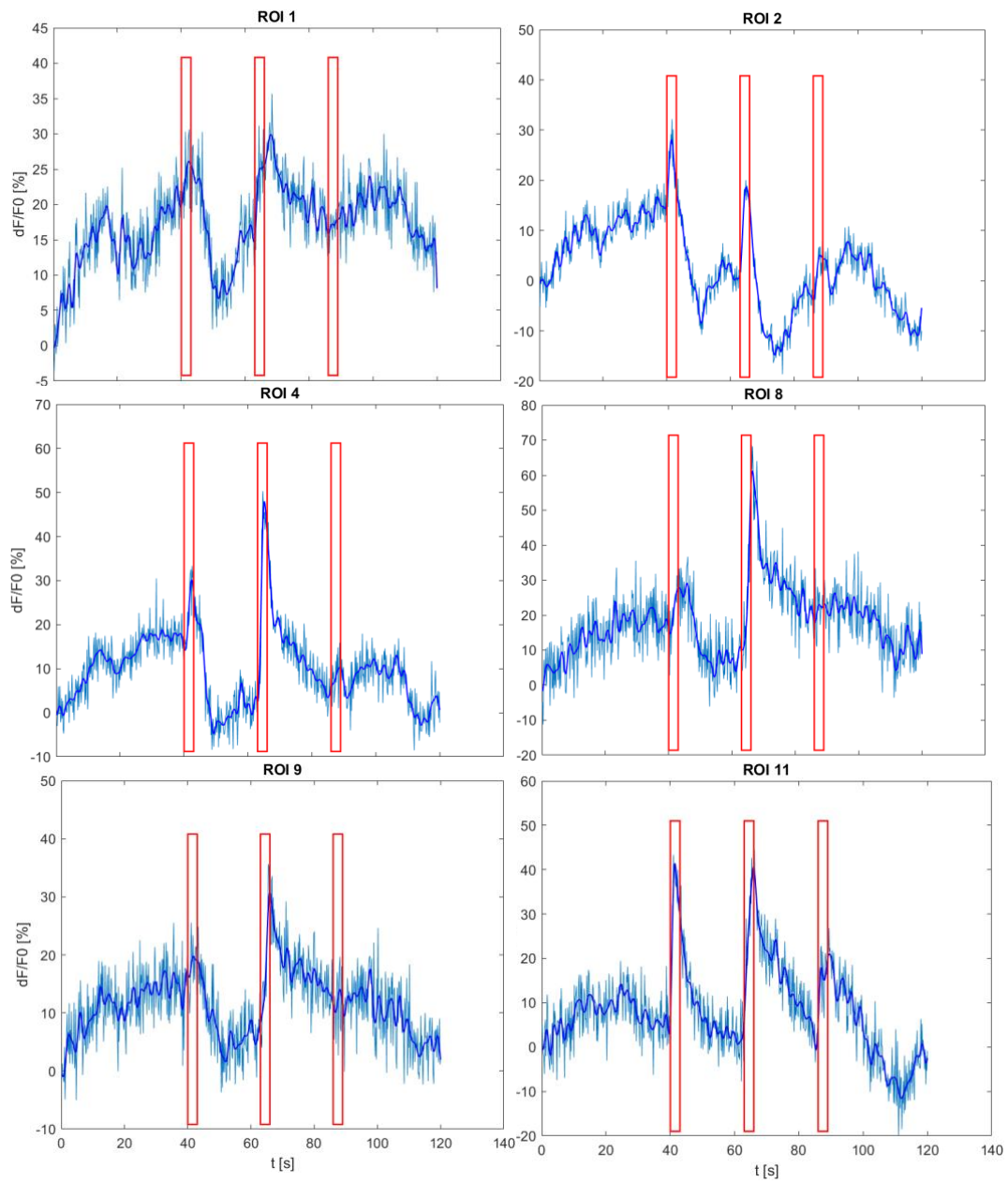


Figure 36 Intensity profile of fluorescence variation for different ROIs of Figure 33 during 1-hexanol presentation protocol. The red rectangles represent the odor presentation.

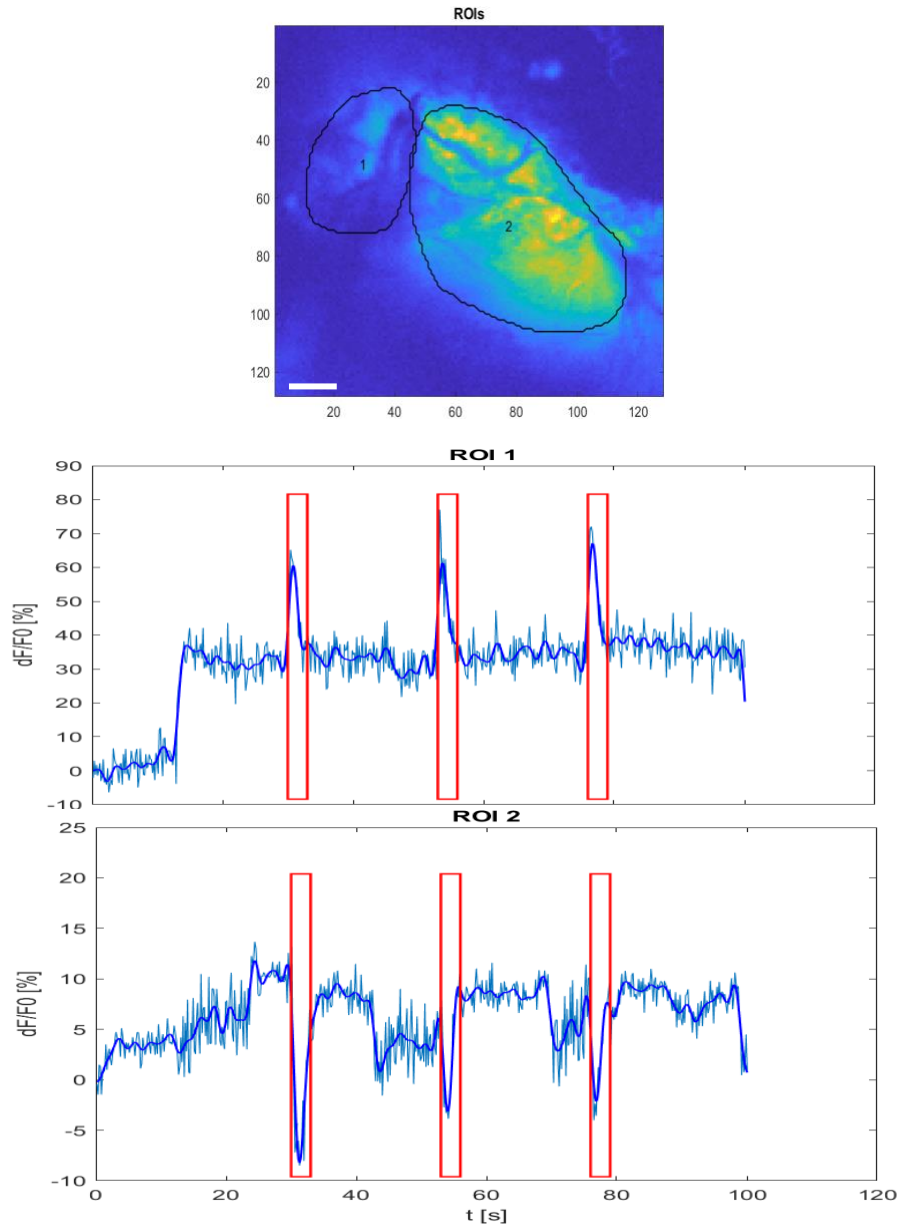


Figure 37 Averaged response to odor mixture for two different areas in the antennal lobe plane: ROI 1 is the surrounding area where the glia cells are, ROI 2 is inside the antennal lobe. Odors were presented in correspondence of the red rectangles. Scale bar 20 μm .

6.2.2 Whole brain responses to optogenetic stimulation

In a first attempt in order to induce neuronal activation in drosophila brain we looked to whole brain response. We've firstly tried to target an antennal lobe with a single point stimulation of 200 ms, monitoring the response in different areas of the brain.

An example is reported in Figure 38 and following, where we tested a fly expressing the ChR2-XXL in the projection neurons that innervates from the antennal lobe and connect the glomerular regions to the higher order centers (mushroom bodies and lateral horns), while the calcium sensor is expressed pan-neuronally.

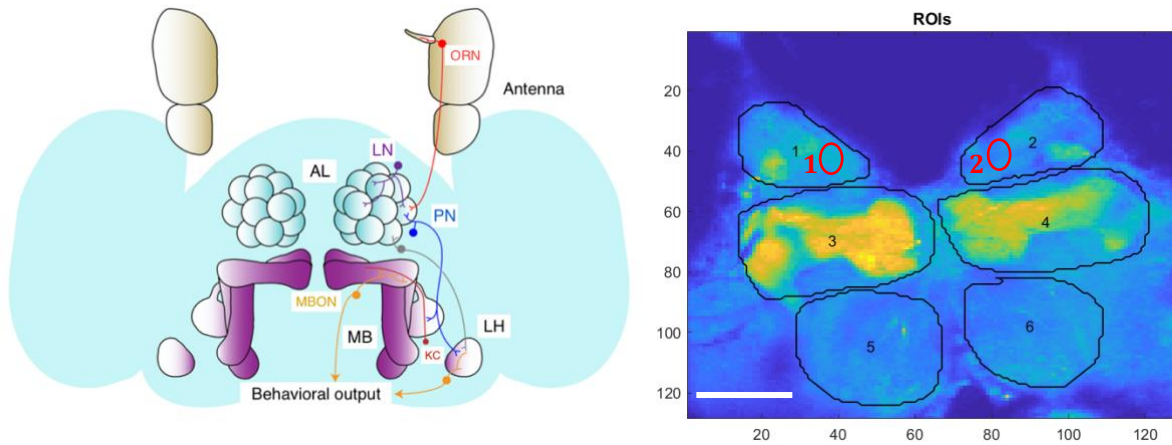


Figure 38 On the left, a sketch of drosophila olfactory pathway: the odor is detected by ORNs at the level of the antennae, information is passed to glomeruli in the AL and sent to higher order centers (MBs and LHs) through PNs (Sayin et al., 2018). On the right, whole fly brain and selected ROIs; ChR2 is expressed at the level of PNs, GCaMP pan-neuronally. ROI 1 and 2 are the left and right antennal lobe respectively, while in ROI 3 and 4 the upper structure of the mushroom bodies is visible. (the fluorescent image has inverted orientation with respect to the sketch on the left). Two different stimulation points are represented by the red circles (responses in Figure 39 and Figure 40 respectively). Scale bar 100 μm.

As it is visible in Figure 38 right we focused on a plane on the upper layer of the antennal lobes, from where also the part of mushroom bodies near to the antennal lobes (about 20 μm from the upper layer of the MBs structure) is clearly distinguishable with its characteristic shape.

Here we've performed 3 different repetitions of 200 ms stimulation at a power lower than 0.02 mW at the objective (frame rate: 3.5 fps); the data reported are an average response over the 3 trials, the red lines at zero time indicate the stimulus presentation (in all the following figures, eventual discrepancies between signal increase and stimulus onset are given by time scale adjustments after stimulation frames removal and average processes: looking at the raw data, the increasing signal starts always with the stimulation). From this first example it is interesting to notice how the antennal lobe of interest presents generally a strong response.

Interestingly, in this case, its stimulation is followed by the direct activation of the proper region of interest and of the relative mushroom body upper region too, with a less significant response in the contra-lateral mushroom body. This is true for both hemispheres' stimulations (Figure 39 and Figure 40).

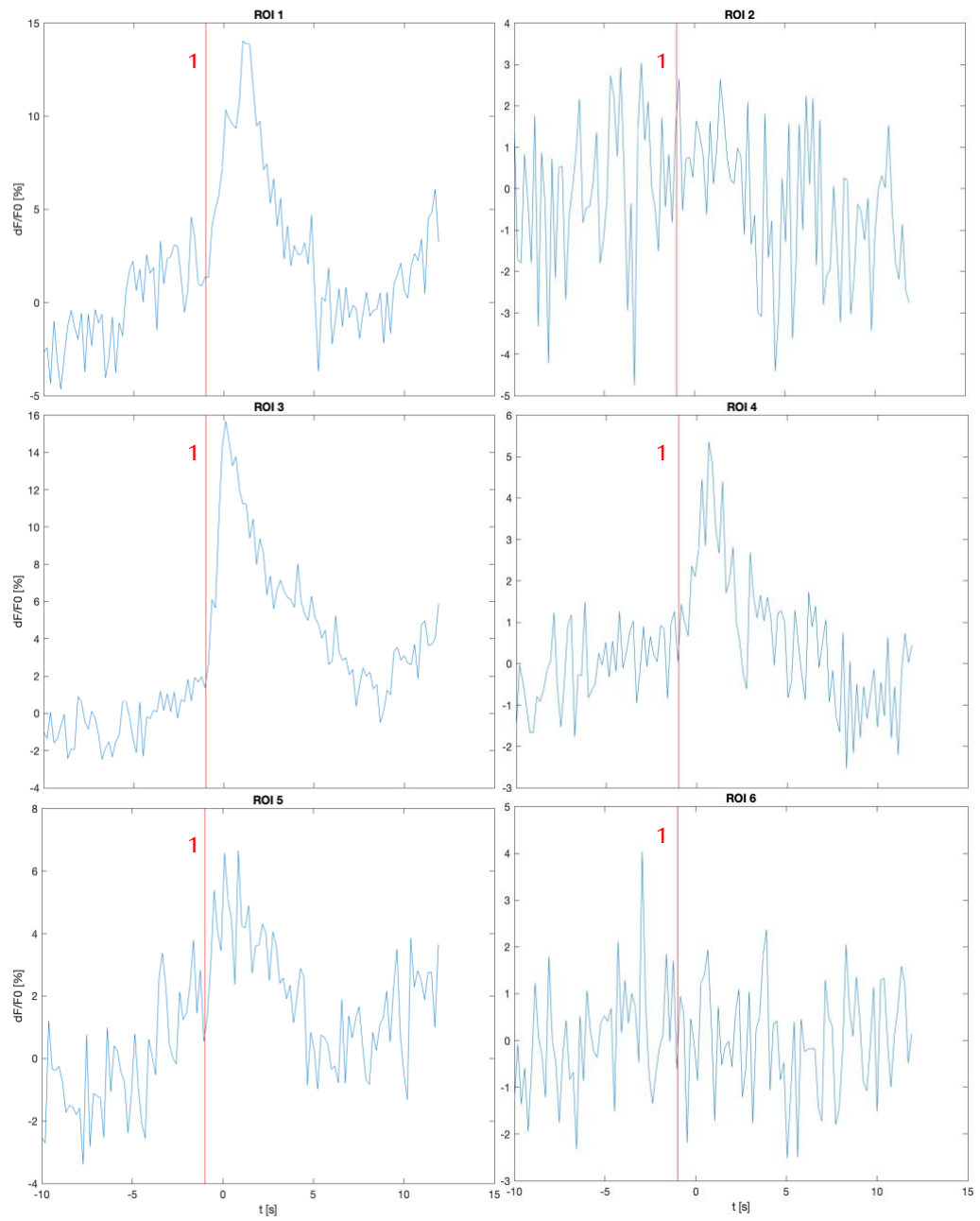


Figure 39 Intensity profile averaged over 3 trials (left antennal lobe -ROI 1- stimulation) for ROIs of Figure 38 right.

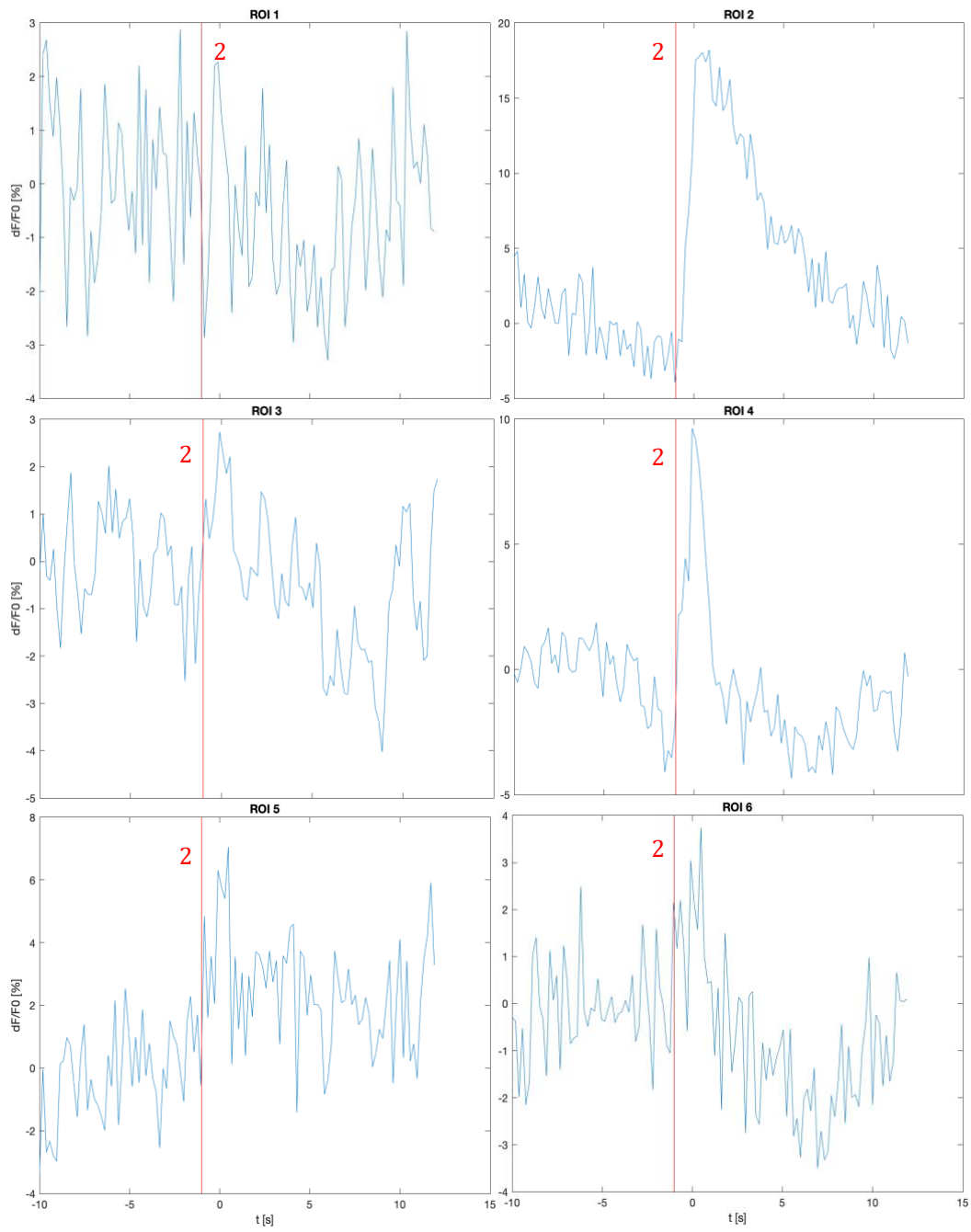


Figure 40 Intensity profile averaged over 3 trials (right antennal lobe -ROI 2- stimulation) for ROIs of Figure 38 right.

As it is visible from these experiments we can notice no response of the contra-lateral antennal lobe, but only of the mushroom bodies; this would suggest us the possibility to exclude an optical over-excitation (that would have elicited both antennal lobe activity) and interpret the responses as proper electrical signaling between the primary and secondary olfactory centers.

A different example is given in Figure 41 and following, showing a fly expressing the opsin at the level of receptor neurons innervating to the antennal lobes, and the GCaMP pan-neuronally expressed.

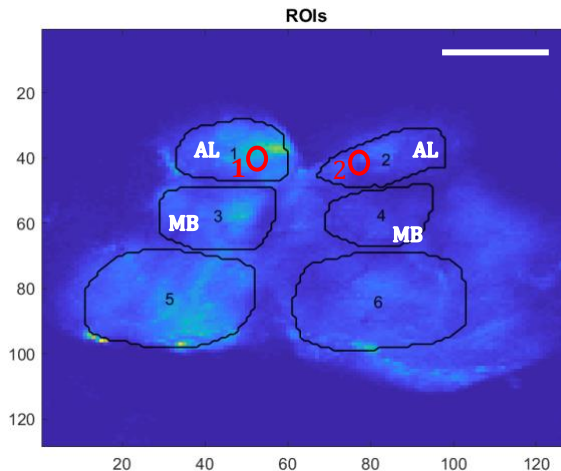


Figure 41 Whole fly brain and selected ROIs; ROI 1 and 2 are the left and right antennal lobe respectively. Two different stimulation points are represented by the red circles (responses in Figure 42 and Figure 43) Scale bar 100 μ m.

Results are presented in Figure 42 and Figure 43, referring to areas depicted in Figure 41: in the first case (Figure 42), the activation point is inside the left antennal lobe (ROI 1). Here we've performed 4 different repetitions of 200ms stimulation at a power lower than 0.02mW at the objective; the data reported are an average response over the 4 trials. Here it is interesting to notice how the antennal lobe of interest presents a strong response, but also the other one undergoes a significative increase; the same cannot be said for other areas of the brain. Interestingly, an analogous behavior can be found stimulating the right antennal lobe too (Figure 43).

Since we would expect a communication between antennal lobes and mushroom bodies, but no significant response is visible at the level of these second order centers, while a contra-lateral antennal lobe activation is found, we cannot exclude in this case that the activation is only optically triggered, with an over-excited area of activation. It's still hard to explain why the mushroom bodies are not responding, it could also be the case that during the preparation some connections were lesioned, or instead the activation stimuli were able to induce a response of the AL but these were not able to trigger any signal to the MBs. A more detailed investigation should be performed with repeated measurements.

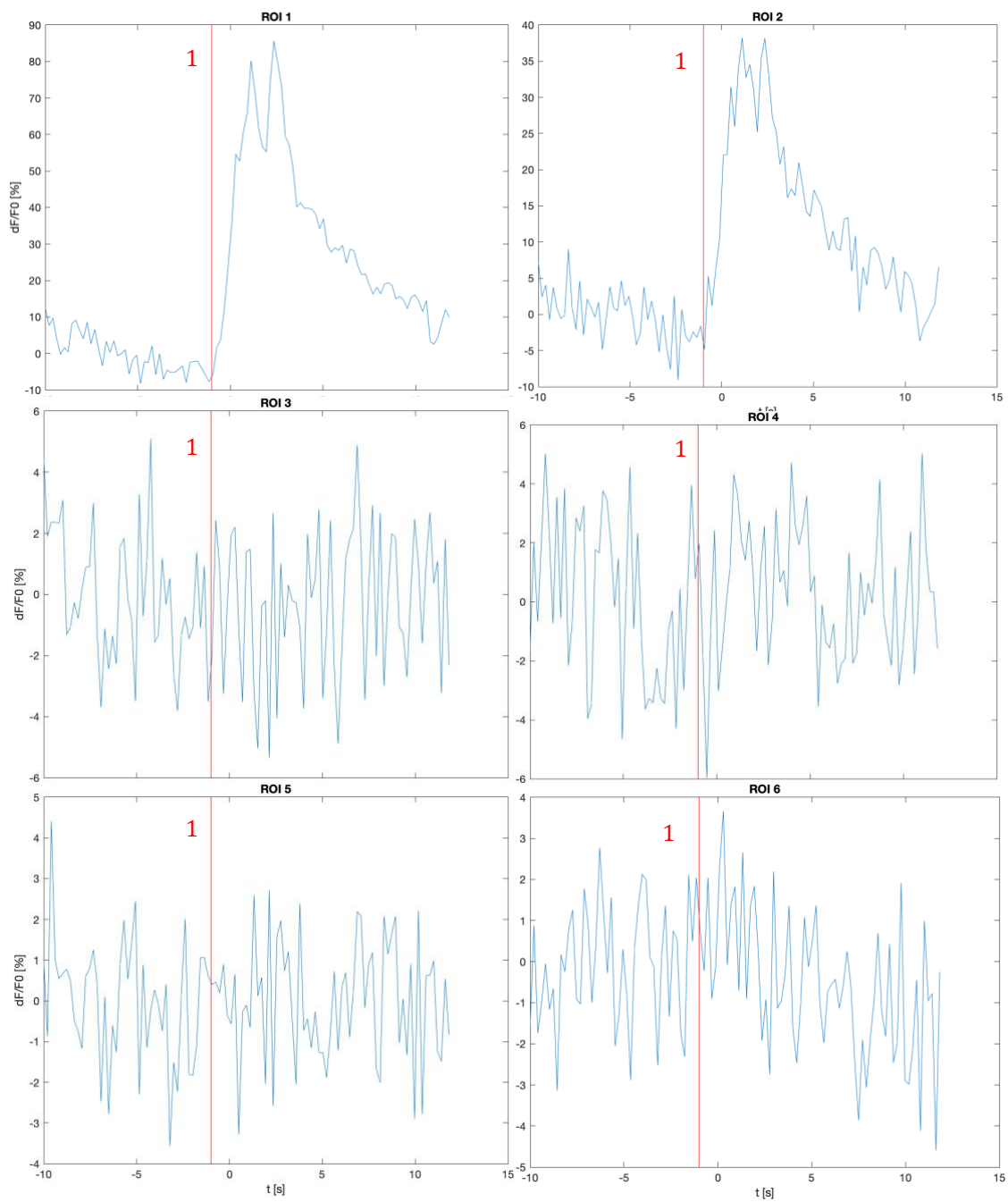


Figure 42 Intensity profile averaged over 4 stimulus repetitions for ROIs in Figure 41; the left antennal lobe (ROI 1) was targeted.

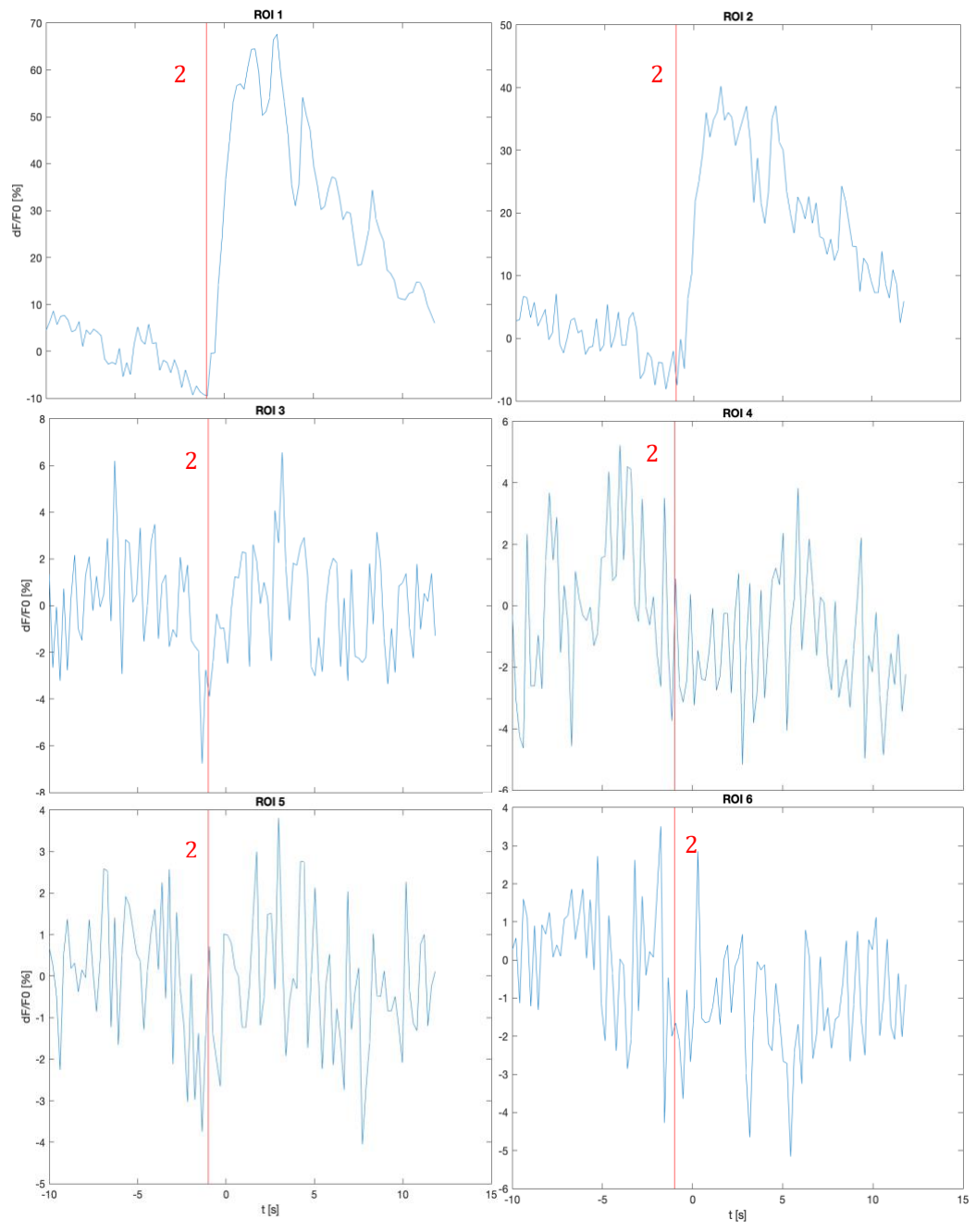


Figure 43 Intensity profile averaged over 4 stimulus repetitions for ROIs in Figure 41: the right antennal lobe (ROI 2) was targeted.

This is a first step through the validation of the method since it shows the possibility to activate optogenetically the brain of the living animal.

Interestingly, this behavior is univocally triggered by the opsin stimulation, since we have never found any similar activation in flies expressing the only GCaMP6 molecule. An example is reported in Figure 44, where no change in fluorescence is detected following an antennal lobe stimulation in any area of the brain; moreover, this is true for both low power and higher power stimulations, while the flies were instead alive and, in some cases, responsive (checked with odor stimulation and body movements).

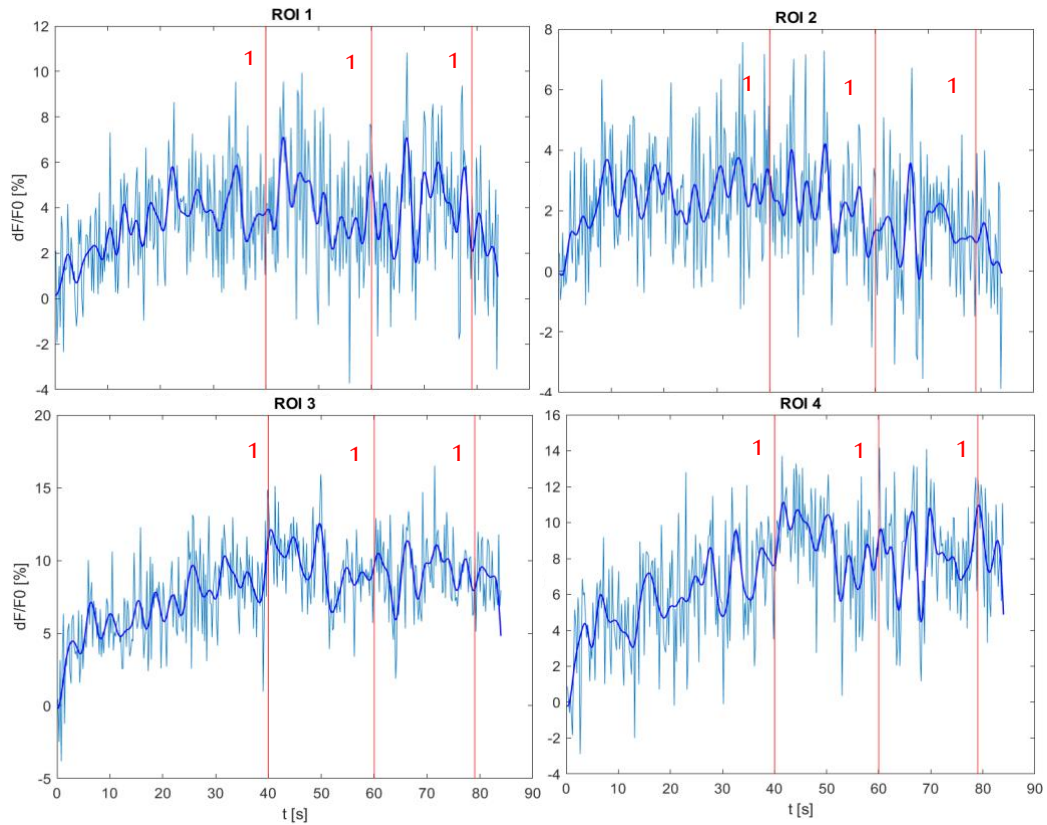


Figure 44 Intensity profile for different regions of the fly brain expressing only GCaMP6, following a stimulation protocol of the right antennal lobe with 0.025 mW at the sample for 150ms (three repetitions, red vertical lines). ROIs correspond to analogous regions to Figure 41.

This can validate our previous results, proving our capability of elicit neuronal response in the brain of flies expressing ChR2, and at the same time detect it thanks to GCaMP6 fluorescence, despite the spectral overlap of the two molecules.

6.2.3 Antennal lobe stimulation

In order to check the effect of blue laser power in glomerular activation, different experiments were performed trying to change power and time stimulation. The aim was to check the parameters in order to induce a specific activation inside the antennal lobe.

The first step was to find an appropriate stimulation time capable to activate consistently the opsin, but not too long to induce photodamage or overexcitation. For this reason, we tested responses to stimuli of the order of ms, finding positively that these were able to induce activation of the antennal lobe. The stimulation we chose is one of the simplest, a continuous illumination spiraling in 5 μm around a single spot. In Figure 45 is reported an example of antennal lobe response to a series of five different stimulation lengths at fix power, with the stimulus responses reported in color code in an ascending order; is it clear how the antennal lobe is already activated consistently at 100-150 ms, spreading even more the activation for stimulation times approximating 200ms. In general, we've noticed that between these range of durations there is not a huge difference in response, since the biggest contribution is given by power. For the previous reasons, we chose to fix our protocol stimulation length at 150 ms, a good compromise to have a clear activation in a very narrow time band.

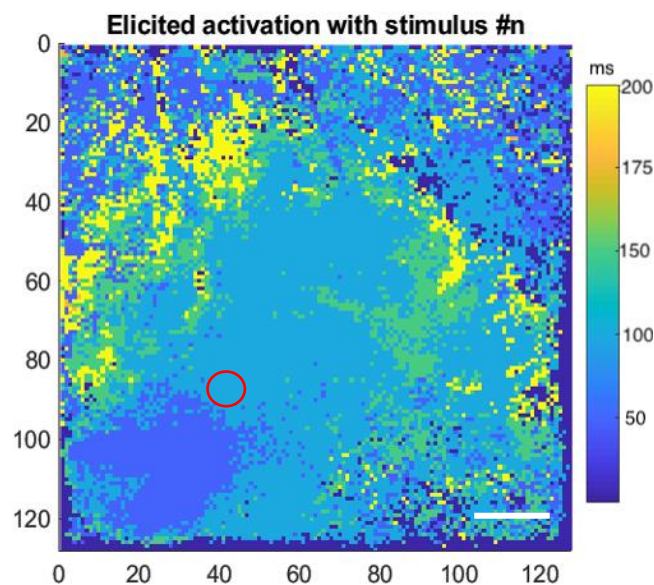


Figure 45 Color code map of the antennal lobe, indicating areas of the AL (different glomeruli) activated by stimulations of different lengths. The red circle indicates the stimulation point, blueish areas the ones activated by lower lengths and yellowish areas the ones activated by higher length of stimulation. Scale bar 20 μm .

Since the stimulus duration of 150 ms was properly adapt with the response timings we wanted to investigate, and since, as I mentioned, the biggest influence on response spreading is given by the power (as I will discuss better in the next paragraph), no further trials were performed trying to vary the stimulation time parameter, focusing instead on the power.

Another step was to check the activation, pointing at different positions in the antennal lobe field of view. An example is reported in Figure 46. Here two repetitions of three stimulations in different points are visible (the total six stimuli in correspondence of the red lines): the first two target two different glomeruli, while the third one is a point outside the antennal lobe.

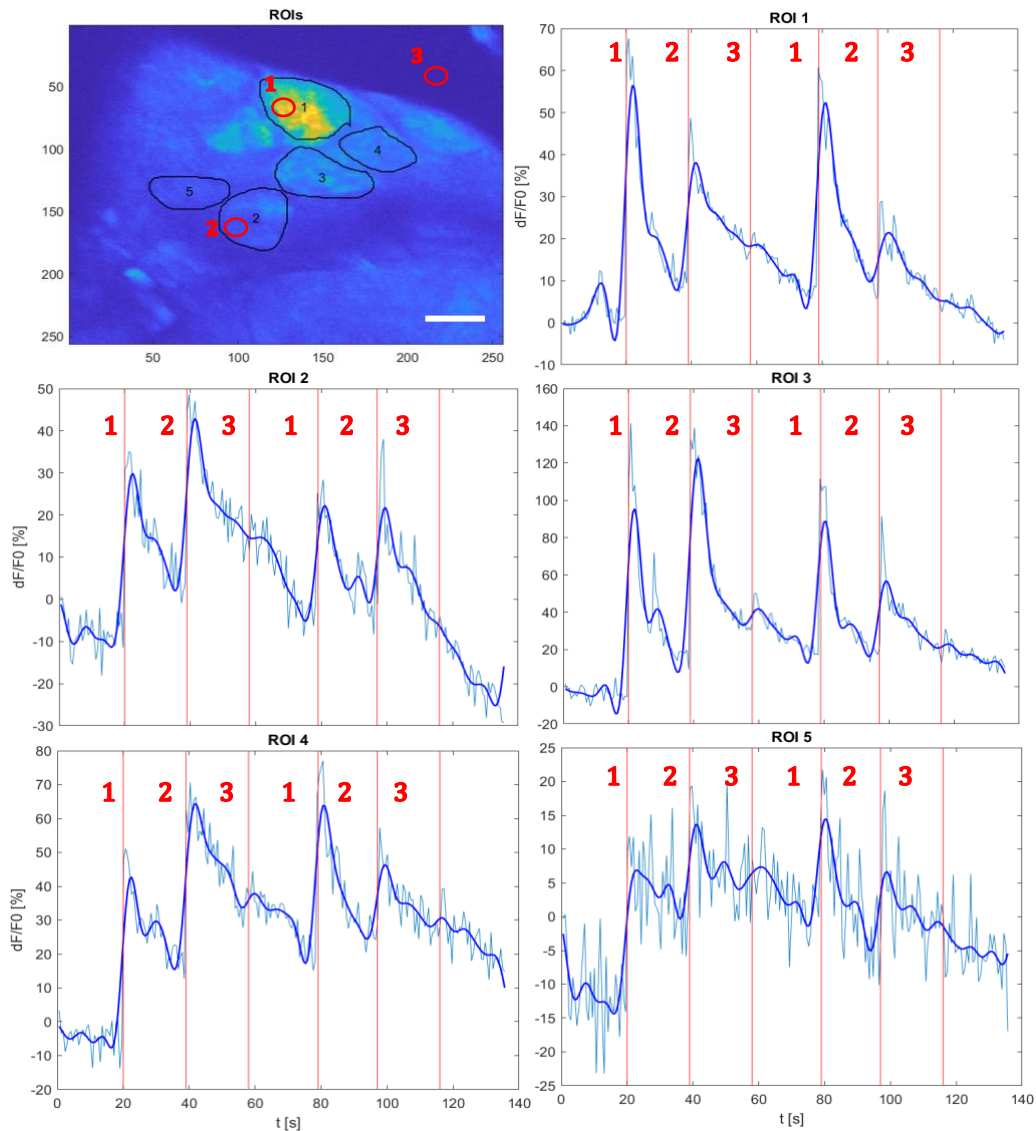


Figure 46 Intensity profile for different glomeruli (ROIs selected in the upper left image), following a double repetition of three points (upper left, red circles) stimulation at intervals of 20s (red vertical lines indicates the different stimuli). The first stimulation is in correspondence of ROI 1, second at ROI 2 and the third one is outside the antennal lobe. Scale bar 20 μm .

These intensity profiles are interesting, since they show a general response of the antennal lobe in correspondence of the blue laser opening, demonstrating once again our capability in stimulating the first olfactory centers; furthermore, a specific response can be investigated: in particular the glomeruli directly involved in laser stimulation show an high fluorescence variation (ROI 1 and ROI 2), with, usually, a bigger signal (at least 10% higher than the neighbors) correspondent to the proper stimulation (first for glomerulus 1 and second for glomerulus 2). Other nearby glomeruli show lower responses (except glomerulus 3) to the stimuli. Moreover, it is interesting to notice that the third stimulation doesn't elicit never any change in fluorescence, in accordance with the fact that it's pointing outside; this provides us a control for the correct functioning of the experiment.

However, the results were not always congruent; a difficulty we encountered, and that has to be fixed better, regards the unspecific activation of the antennal lobe: it happened, in some cases (about 40% of the times), that an increase in fluorescence was found even when pointing the blue laser outside the antennal lobe. We will show in the next paragraph that a better control can be reached reducing the power of the stimulation laser, restricting in this way the activation spread; however, this doesn't solve completely the problem, that still happens in some situations even at minimum power (an example is reported in Figure 47).

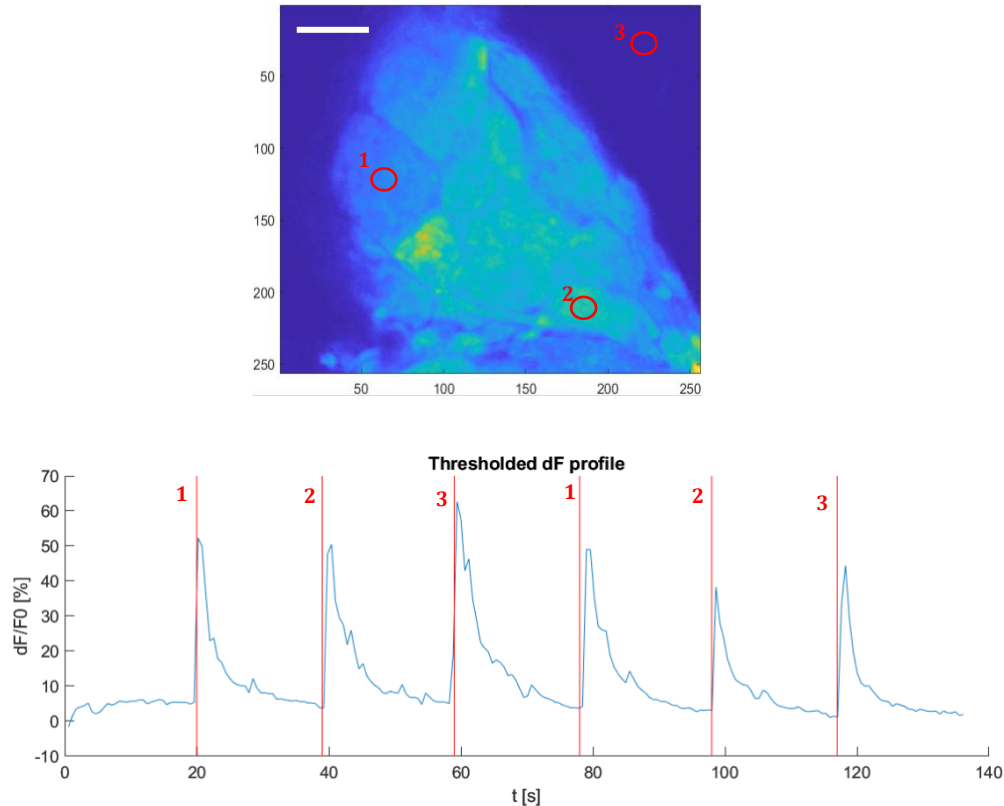


Figure 47 Overall intensity profile for two repetitions of three stimulations at different points (red circles, the first two inside the antennal lobe, the third one outside). Scale bar 20 μm .

We have already seen how, both with cells and with brains not expressing opsin, any response is elicited. One again we tested this protocol of antennal lobe stimulation with fly lines expressing only GCaMP6. As it is visible in Figure 48, no significant increase in fluorescence is visible after stimulation, even at higher powers; in no way we were able to mimic any of the previous reported brain activations in flies not expressing the opsin. This means that the responses are opsin specific and we can exclude any direct activation of the calcium sensor molecule by the blue laser, effect that can be influent theoretically, given the spectral overlap between ChR2 and GCaMP, but that is not detected for the powers we use, as demonstrated by all these examples.

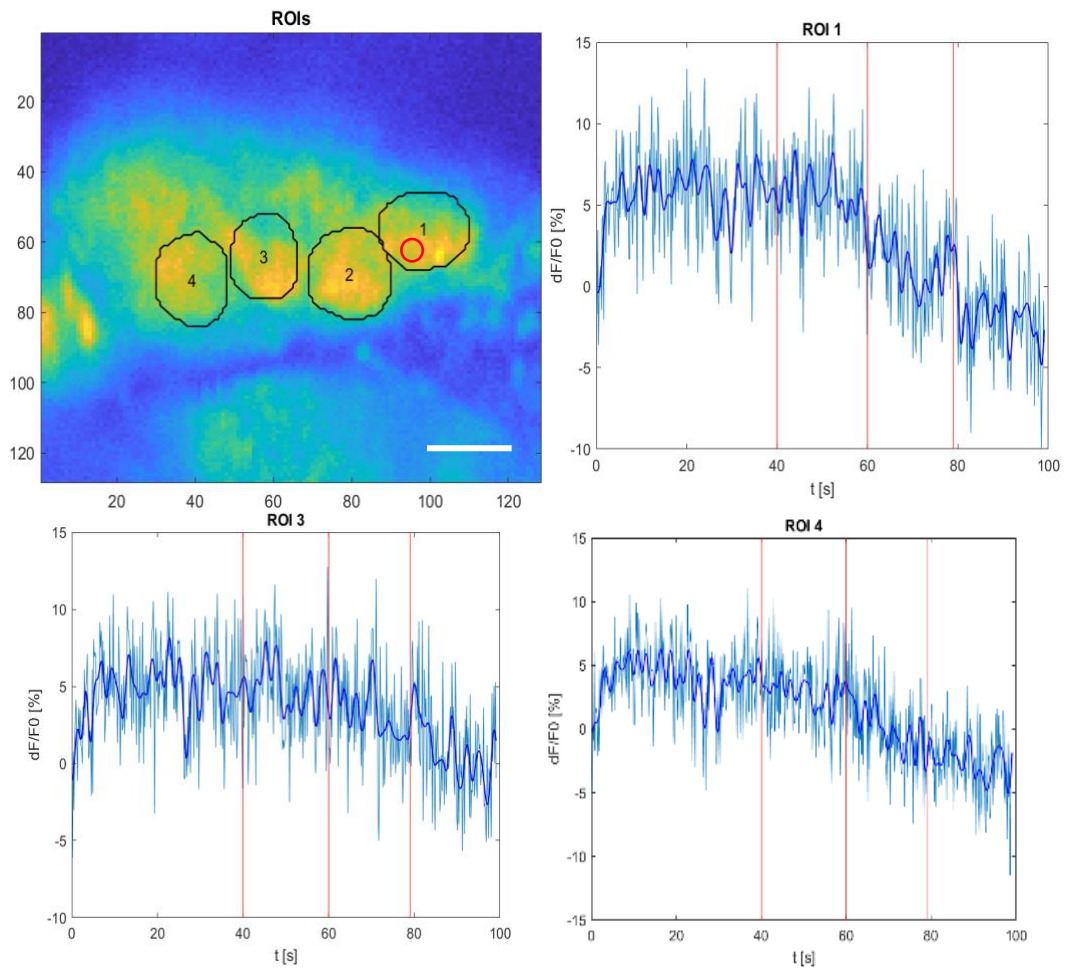


Figure 48 Antennal lobe response to three stimulations of 200ms (red vertical lines) at relative high power (about 0.2mW at the objective), in a fly expressing only the GCaMP construct. No response to blue light stimulation is detectable at all. The stimulation point is indicated by the red circle. Scale bar 20 μ m.

6.2.4 Single glomerulus stimulation

At this point we have seen we are able to activate the brain of the drosophila and in particular its antennal lobes. The final aim was to check the activation spread and to find the threshold for which the lowest optogenetic response is generated, ideally being able to directly stimulate only a single glomerulus.

Thus, we have improved the stimulation playing with power. In fact, the idea is that under a certain power no cells are activated since a not sufficient number of channels is opened; increasing the power, cells are going to be activated consequently, increasing in number, since the threshold power is reached in always more regions also nearby the central focal point. In this way we would test the feasibility to induce activation of a single glomerulus inside the antennal lobe, in order to be able to act in a single functional node of the primary olfactory centers. I would remember at this point that the approximate estimated blue activation laser spot dimension is less than $5\mu\text{m}^2$ in the plane and less than $20\mu\text{m}$ axially, while the glomerulus characteristic size is around $20\mu\text{m}$.

An example of this protocol is reported in Figure 49, where a series of ten stimulations is presented at increasing blue laser powers. How it is clear from the intensity profiles, lower powers elicit no response at all as expected, until a threshold power is reached. At this point, only the neighboring areas of the stimulation position start to show an increase in fluorescence that is even more persistent at higher powers, when also other more distant areas start to respond too. Looking at Figure 49 upper right, where the color code numbers represent the powers in ascending order (blue is the lowest power, yellow the highest), it is clear how at the lower values only the glomerulus of interest (ROI 1) is responding, while the other areas start to increase their fluorescence only at bigger powers, in particular with power higher for regions further from stimulation point. To notice also that the power threshold is very narrow since just a small increase in intensity from this value will activate a bigger area with respect to the single glomerulus; still the difference in activation can be clearly pointed out looking at the intensities, since even if more areas are activated with powers slightly bigger than threshold, there is always a consistent difference between activation intensities of the area directly illuminated (with the higher response) and out of target regions (responding with a lower intensity variation).

This is an example of ideal situation, in which a clear power threshold can be set in order to stimulate a single unit of the antennal lobe. I would stress that we encountered many difficulties since it was not always easy to replicate this condition in other flies, and many times an overall activation of the antennal lobe was obtained even at the lower powers, being impossible to activate a single unit. This is why there's still some work to do in order to optimize this part and to construct a solid model that can be used for a systematic study of glomerular network investigation.

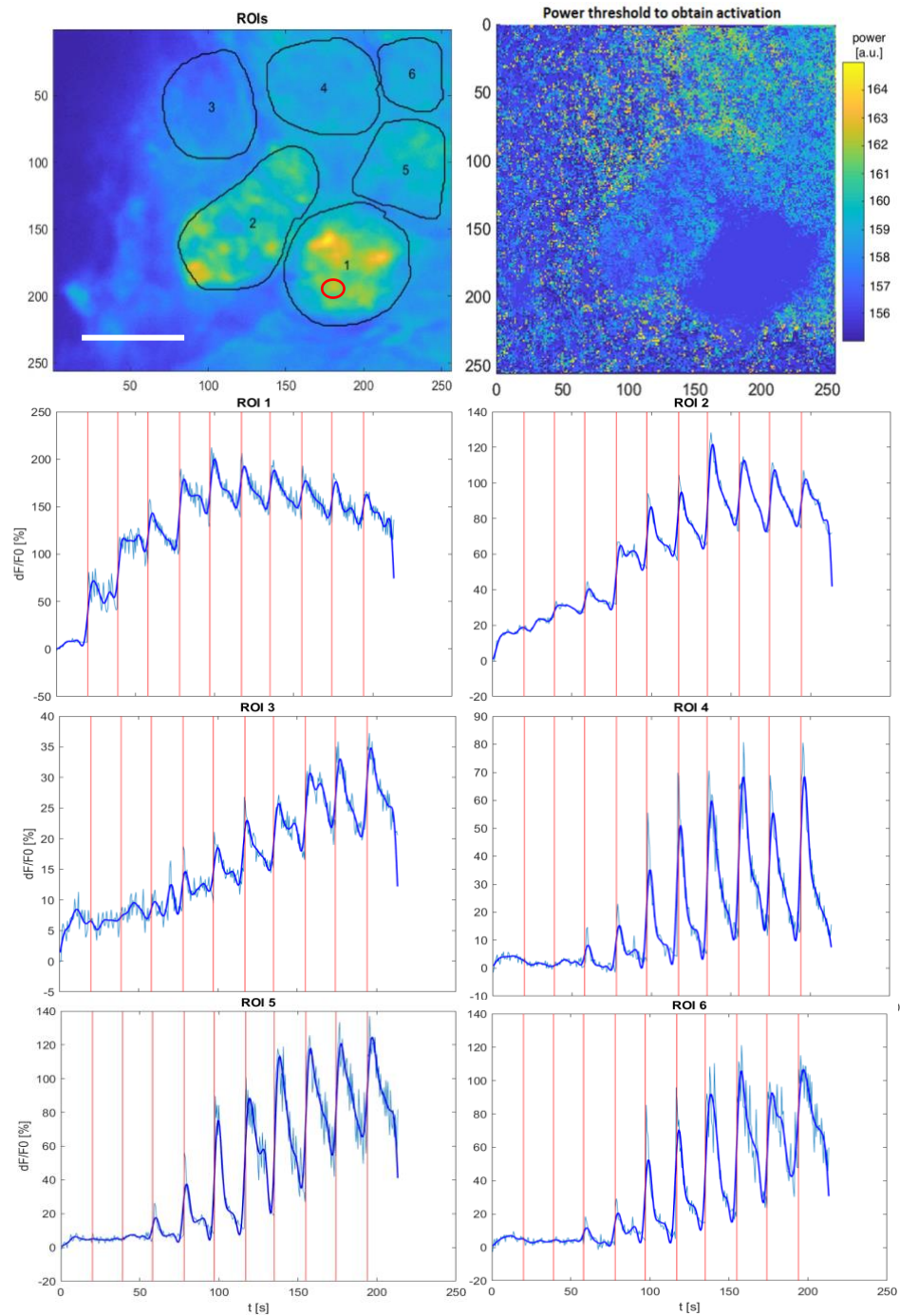


Figure 49 Intensity profiles for different glomeruli depicted in the figure upper left, following a set of 10 stimulations of ROI 1 (red circle in figure upper left) at increasing blue laser powers (stimuli indicated by the red vertical lines). In figure upper right a color code map indicating the lower power necessary to stimulate the different areas is depicted, with powers ordered in ascending order (blueish areas activated by low power, yellowish areas, activated by high power). Power indicated in software a.u. Scale bar 20 μm .

6.3 Data analysis

I report here some analysis methods applied to our data, in order to infer some interesting and more detailed information with respect to the ones obtained by the only intensity profile investigation. All analysis are performed with my custom Matlab software.

A first approach is to compute the simple correlation between signals of different ROIs. In Figure 50 a comparison between the average over three blue laser stimulations on ROI 1 is reported, where in color code (right figure) there is the correlation between couples of ROIs' (depicted on the left) averaged signals.

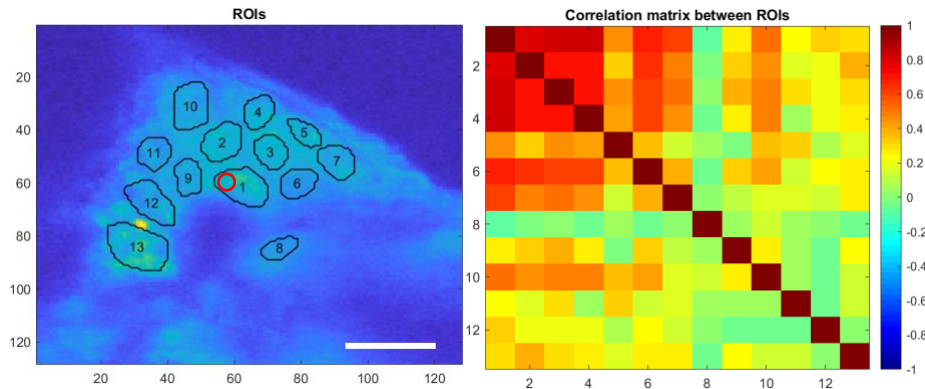


Figure 50 Correlation (right) between different ROIs (depicted on the left) of an opsin expressing antennal lobe, following a blue laser stimulation of ROI 1 (red circle, left). Scale bar 50 μm .

From this analysis it is easy to visualize the ROIs with a similar profile, that are activated together or responding similarly in general; in this example some regions around the activated point (ROI 1-7) show in fact a high correlation between themselves, meaning they are responding to the stimulus, while the others have low or zero correlation since they present background variations only. This permits to infer a first hint about glomeruli functional connectivity and eventually to identify clusters of functional connected glomeruli. This information must be considered in combination with other control data to exclude the possibility that this activation is driven optically.

Another interesting analogous analysis could be the computation of the correlation of all the points in the image with a specific one, for example the stimulation point (seed-based correlation analysis). The correlation is still represented in color code, but this time every pixel represents the correlation of the corresponding image pixel with the selected one. An example is given in Figure 51.

From the correlation plots, it is visible how for a lower power (left plot for stimulus 1), only the points inside the excited glomerulus are highly correlated; increasing the power (middle and right plots for stimuli 3 and 5), always more areas have a correlation with the time response of the excitation point. This shows how the correlation area with the stimulation point increases with the power of the blue laser.

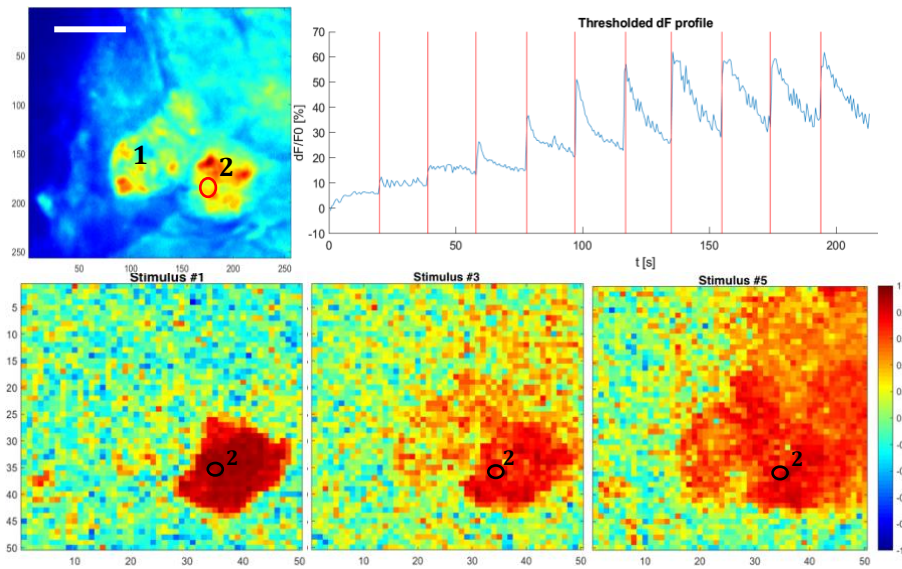


Figure 51 Analysis for a set of 10 stimulations with ascending blue laser power. Upper left, stimulation point (red circle); upper right, overall intensity profile. Lower, three example of seed-based correlation map with stimulation point 2 (for stimuli 1,3,5). Power values from stimulus #1 to #10 (in software a.u.): 156,157,158,159,160,161,162,163,164,165. Scale bar 20 μm .

Another interesting behavior can be noticed at higher powers: in Figure 52 it is shown a comparison of correlations with stimulation points respectively targeting the left and right glomerulus (of Figure 51), for stimulus #9 (high power). It is clear how the correlation found in Figure 51 after a certain power drops down (i.e. the two main neighboring glomeruli are no more correlated as for lower power #3 and #5 in Figure 51), while only some other glomeruli, comprehending the excited one, remain highly correlated. It seems like an increased power changes the correlation between units, fact confirmed by both the stimulations of the two different glomeruli respectively (left and right image of Figure 52).

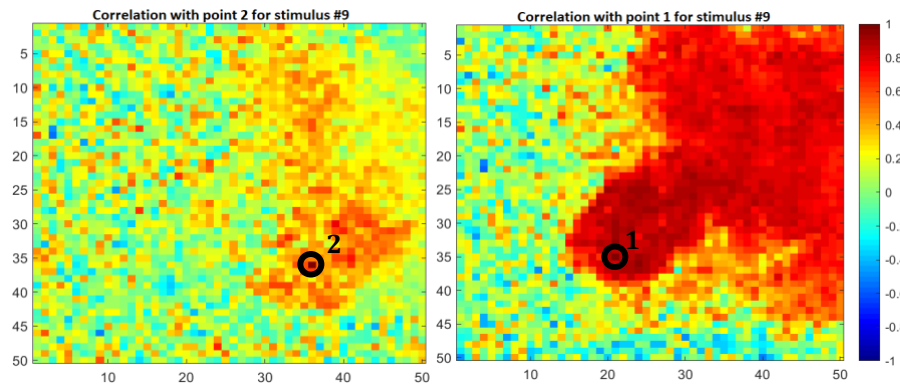


Figure 52 Correlation maps with stimulation points; left figure refers to a stimulation on the right glomerulus (stimulation on point 2), right figure in the left one (stimulation on point 1); analysis for low power #9 stimulation of series in Figure 51.

Even further considerations can be carried on looking at these correlation maps, directly comparing the stimulations in the two neighboring glomeruli respectively. We have already seen how high-power stimulation acts coherently for the two targets, even if with a different degree of correlation (Figure 52); moreover, also a comparison at low power (stimulus #1) gives us interesting hints, like it is visible in Figure 53. In this case the correlations with the two activation points lead to different outputs depending on the stimulated glomerulus. At this lower power, that elicits a correlation only of points inside the glomerulus 2 on the right when it's directly pointed (Figure 53, left), the same stimulus triggers a correlated response of both glomeruli if pointing the left one 1 (Figure 53, right). This means we found an asymmetric behavior, a first interesting step towards an investigation of glomerular connection directionality.

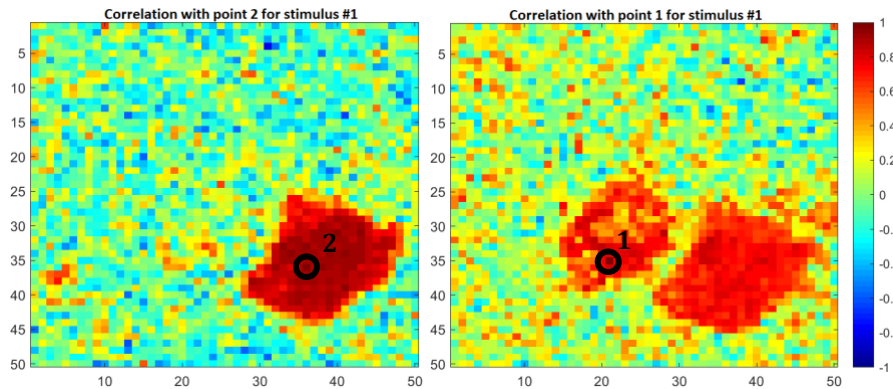


Figure 53 Correlation maps with stimulation points, left figure refers to a stimulation on the right glomerulus (stimulation on point 2), right in the left one (stimulation on point 1); analysis for high power #1 stimulation of series in Figure 51.

As an additional tool, to confirm and implement the analysis, a cross-correlation can be performed, to infer some direct information about signal directionality. An example is given in Figure 54: here a whole brain recording is reported, while activating the left antennal lobe. Looking at the intensity responses (previous Figure 39), an activation is detectable in the stimulated area and relative mushroom body (ROI 1 and 3); other lower responses are visible on the contra-lateral upper mushroom body and on the same side lower mushroom body/lateral horn area (ROI 4 and 5 respectively). Analyzing the cross-correlation we can notice that a maximum correlation occurs with a lag of 0.2 s between stimulated antennal lobe and the two upper areas of the mushroom bodies, while a 0.6 s lag is present for lower left mushroom body area, further from the stimulation point. We can infer a time delay and a directionality of the response, with a signal elicited before in the stimulated antennal lobe and only after propagating to the mushroom bodies. It is worth to say that these numbers, at the level of this analysis, have to be considered with the proper attention, not giving too much weight to absolute values and not using them to infer any kind of conclusion; still, these are interesting to suggest some considerations, for example inferring some hints in accordance with the hypothesis presented in the previous discussion looking at the intensity variation (paragraph 6.2.2), where we suggested a functional connectivity excluding an optical over-excitation.

Thus, with this example, we shown the potentialities of this tool.

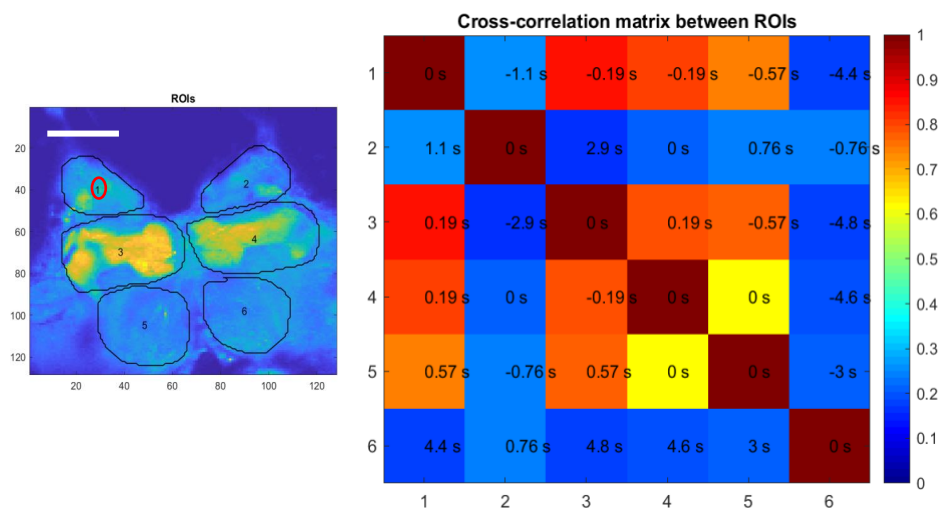


Figure 54 Cross-correlation analysis between different areas of the fly brain, following an antennal lobe stimulation (red circle). In color code it is represented the maximum correlation values, the number inside is the corresponding lag value, i.e. the time shift needed to obtain the maximum correlation, expressed in seconds. Scale bar 100 μm .

Another example exploiting cross-correlation analysis is reported for glomeruli network investigation of Figure 55. This is an interesting experiment, since the targeted glomerulus (ROI1) is showing an oscillatory spontaneous activity even before the stimulation; after this, its intensity is increased, still maintaining an oscillatory behavior, while the other glomeruli start to oscillate consequently (intensity profile reported in Figure 55 right).

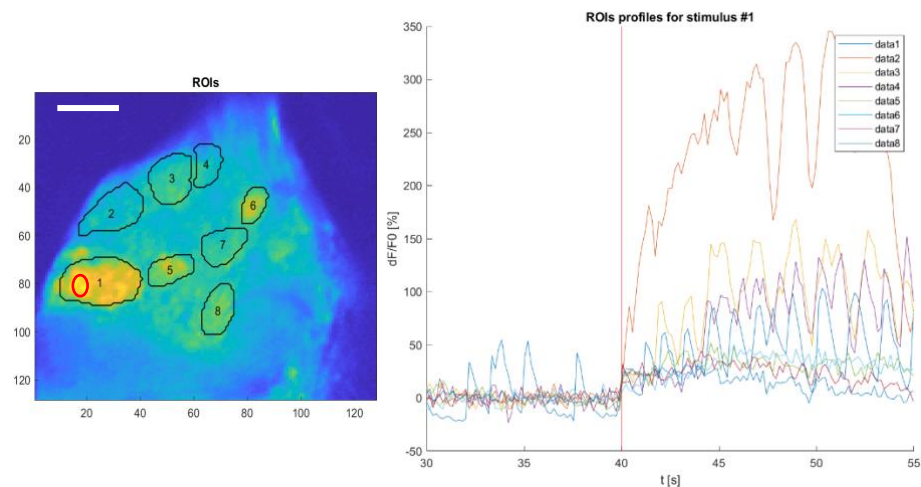


Figure 55 Antennal lobe with ROIs on different glomeruli (left). The glomerulus stimulated is ROI 1 (red circle). Change in fluorescence after stimulus (at 40s, red vertical line) are reported on the right for all the different ROIs. Scale bar 20 μm .

As it is visible from the cross-correlation profiles there is no coherence between the glomeruli before the stimulation (Figure 56), while a huge correlation appears with the stimulus (Figure 57); we can also observe that the maximum correlation it's already present at zero lag in most of the cases, meaning that a shift in the signals doesn't improve the correlation in this case. What it can be more interesting at this point is to study the static correlation for different time windows.

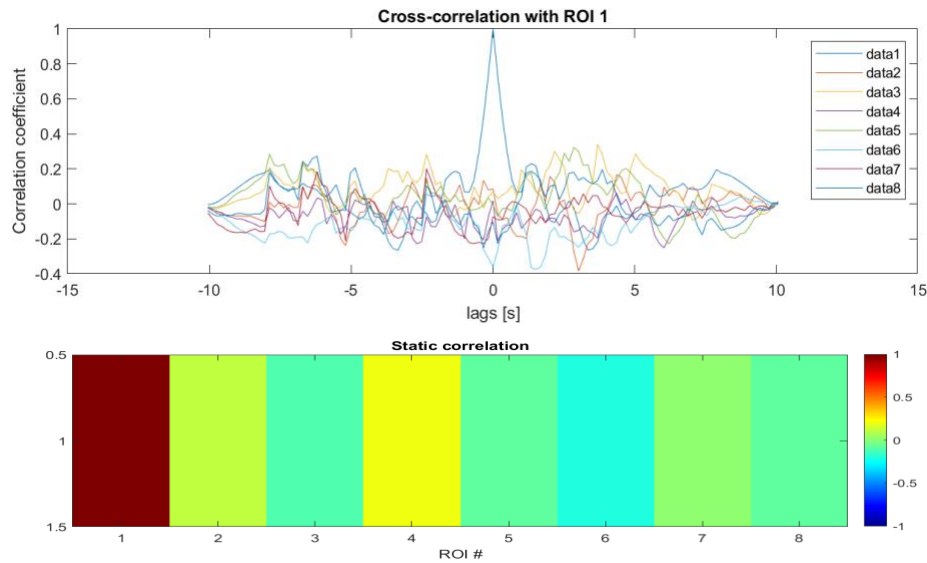


Figure 56 Cross-correlation and static correlation coefficients between targeted glomerulus 1 of Figure 55 and all the others, in a time windows of 20s before the stimulation.

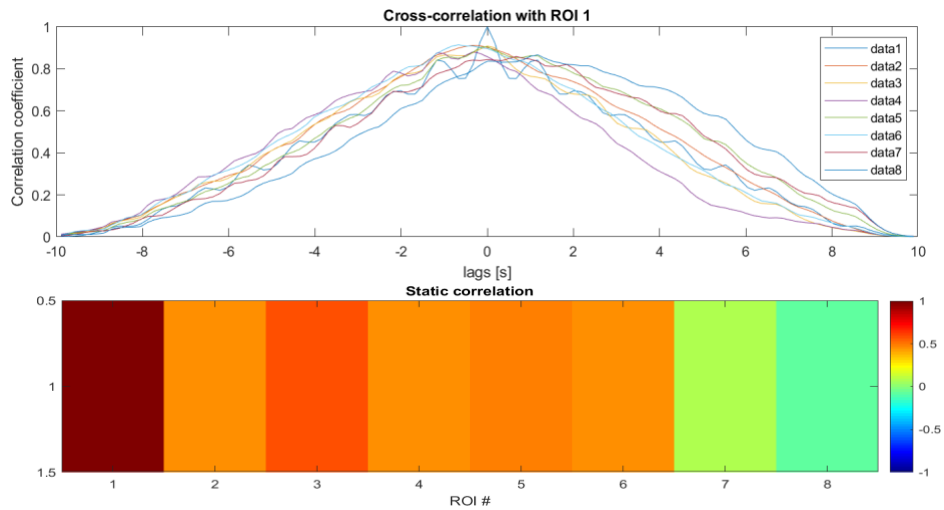


Figure 57 Cross-correlation and static correlation coefficients between targeted glomerulus 1 of Figure 55 and all the others, in a time windows of 20s following the stimulation.

In Figure 58 there is a comparison of correlation matrices for signals 10s before the stimulus (left), in the 10 seconds following it (right) and from 20 to 30s after (bottom). It results, in a clear way, how there's no correlation before the stimulus, while it appears just after, with many glomeruli functionally connected.

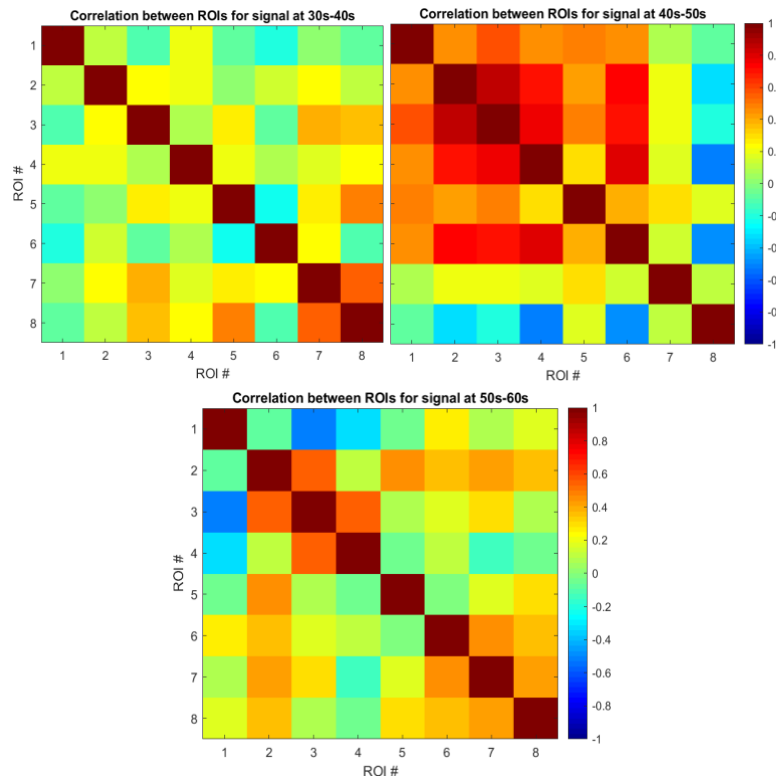


Figure 58 Static correlation matrices between all the different ROIs of Figure 55 for the signals in the 10s before the stimulus (left), 10s following it (right) and from 20 to 30s after the stimulus (bottom); (in the titles time reference stimulus occurs at 40s).

Again, we can infer this consideration by the timing of the responses, many glomeruli starting to fire (or at least to show a strong oscillatory behavior) with some delay with respect to the stimulus presentation: this would suggest a functional rather than an optical activation. Interestingly, many seconds after the stimulus, the starting correlation is lost, but the glomeruli continue to fire in a generally uncoherent way; however, the correlation doesn't drop to zero as in the pre-stimulus phase, but still some glomeruli show a residual correlation. This can give a hint about the effect of ROI 1 stimulation, that triggers the activation of the respective glomerulus and of the others too, which start to oscillate in phase for the first seconds, while losing the correlation just after, but keeping some sporadic connections between some specific glomeruli (like for example ROI 2 and ROI 3 or ROI 3 and ROI 4).

Another interesting way to analyze the temporal response of different units of the olfactory network consists in looking in the frequency domain, calculating the wavelet coherence between two signals. In fact, in some interesting cases as the one reported in the previous example of Figure 55, a characteristic oscillating response is found. In this case, as mentioned, the targeted glomerulus is activated following the stimulation pulse, while the others are following the first one with some temporal delay, showing an oscillatory activity. In this way a frequency analysis can help investigate the oscillation timing and the different activation delay of the glomeruli. An example is reported in Figure 59, where the signal of a given ROI of Figure 55 (ROI 5 in this example) is compared with the one of targeted ROI 1: the oscillating behavior is visible in the upper intensity profile (for a time windows between 10s before the stimulus and 10s after), while the correlation in time-frequency domain between these two signals is depicted in the bottom figure.

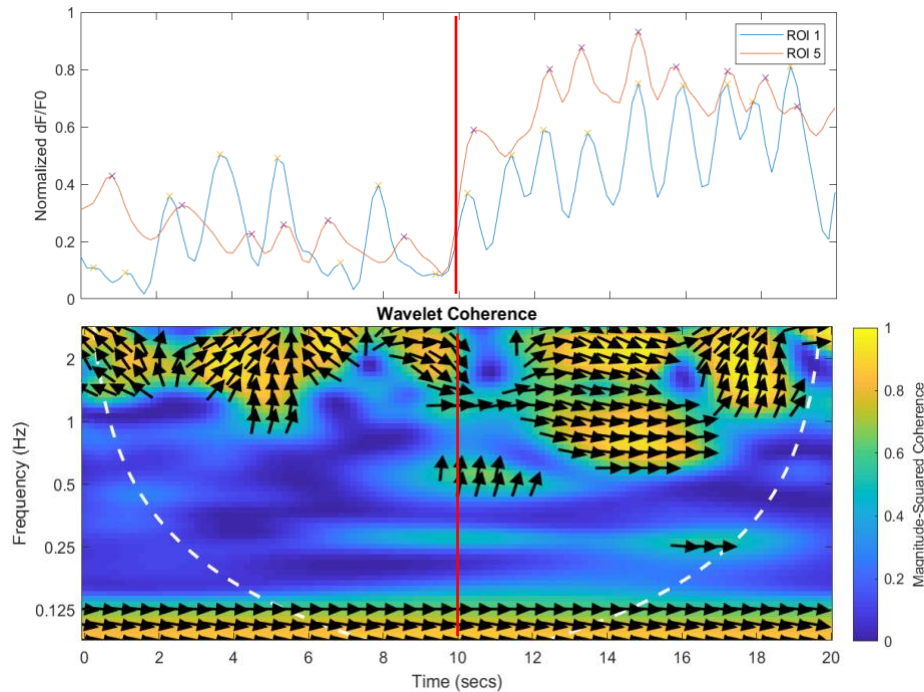


Figure 59 Profile of ROI1 and ROI5 of Figure 55 after stimulation (top) and magnitude-squared wavelet coherence between the two (bottom). Stimulus at red vertical line.

Here the coherence is computed in time-frequency space and the cone of influence is depicted; the interesting part is given by the oscillating responses represented by the higher frequencies band coherence. In particular, the arrows give us indications about the phase of the two signals, corresponding their direction to the phase lag on the unit circle: thus, horizontal arrows pointing on the right mean that the two signals are coherently in phase, while, for example, a vertical one corresponds to a quarter period delay.

In this way we can investigate spontaneous oscillation already occurring before the stimulation and compare it with induced oscillation by the laser pulse. In this case the two glomeruli taken as an example are not in phase before the stimulus; just after, instead, a strong coherence appears with both glomeruli synchronizing to oscillate perfectly in phase for at least 5 seconds (horizontal arrows at frequencies around 1Hz). This suggests clearly how the opsin activation of ROI 1 triggers the coordination of the other glomerulus too.

As I mentioned, we were not able to collect sufficient data to construct a reproducible and solid dataset, thus many results are indicative and the discussions only speculative. What I've tried to show with this work is that we have now a tool that has to be optimized, but that permits us to investigate connectivity in the brain of a living insect, manipulating the nodes of its neural network with optogenetics.

Conclusions

An all-optical approach has many advantages in brain network investigation, permitting both a precise stimulation and a neuronal readout of different cells at a time. Many works performed such an approach with the most advanced technologies (like two-photon lasers both to stimulate and image), choosing mainly molecules not spectrally overlapping. Nevertheless, many of the most efficient calcium sensor and opsin are instead overlapping (since for both sensors, the most performing family is the one excited in the blue spectrum); moreover, at the same time, a cost-effective solution would be desirable.

In this work we showed the possibility to perform a selective stimulation with a basic blue diode laser, while imaging with a two-photon laser, enabling bigger penetration depth; moreover, the feasibility of using some of the most performing sensors (i.e. GCaMP6 and ChR2-XXL) in combination is demonstrated, showing that the effect of opsin activation induced by blue laser stimulation is characteristic and not found in absence of photoactivable channels.

To apply the method, we focused on fly olfactory system. *Drosophila* is a highly developed model in neuroscience, thanks to its dimensions and genetical accessibility. Furthermore, olfaction is one of the most used senses in insects. That's why we used transgenic lines expressing the opsin at the level of the first olfactory centers and the calcium sensors pan-neuronally, in order to study the role of single units in these brain centers. We showed how stimulating the antennal lobes can induce their response, on both side of the brain and with the connected mushroom bodies too. Investigating in detailed the role of single glomeruli in the antennal lobe network, we showed the feasibility of activating only one subunit with our setup, and monitor the following response of all the other glomeruli; in fact, we found in some interesting cases how the direct illumination of a glomerulus induces its specific activation and subsequently the firing of others. This temporal differentiation in responses is a hint of glomerular communication and confirm the possibility of eliciting specific activation of one node of the glomerular network, following monitoring the responding glomeruli.

Finally, we showed some analysis that can help a better and more quantitatively understanding of these connections, illustrating the possibility to apply cross-correlation methods and time-frequency analysis with phase comparison to quantify the different times of firing peaks for both the illuminated glomerulus and the other ones.

Overall, a tool like this allows the investigation of a neuronal network while acting on single units, permitting in principle the reconstruction of a connectome of the area. This would be a big step to define functional connectivity and understand better the role of single elements inside the network under investigation. Moreover, to our knowledge, this is one of the first time a similar all-optical approach is applied to study in vivo functional connectivity in *drosophila*, being published only recently one similar work (Huang et al., 2019); thus, this can have a relevance in the field, given the many advantages of this animal model, overall the accessibility of a whole brain in vivo. Our work suggests in this way the possibility to adopt a cost-effective all-optical paradigm to study this relevant model in an innovative way with respect to the previous approaches with this animal.

To notice, reproducible data are desirable in order to complete the work on connectivity, since only results that are not fully repeatable were obtained: a point to focus on will be the collection of more responding animals stimulating identified glomeruli. A systematic comparison with odor response maps could then be performed, studying the glomerular laser-induced functional connectivity in parallel with the natural odorant response. In this way it will also be possible to mimic natural stimuli and infer many information on how these are encoded in the fly brain. Moreover, it would be necessary to perform a complementary control experiment to validate this protocol, in order to completely exclude a possible activation of the opsin by the imaging laser. During our experiments we already observed that while imaging, activations

comparable with the ones obtained with the blue laser were never elicited; still, a more detailed investigation and quantification of a possible side activation is fundamental.

For an improvement of the experiments a two-photon laser for opsin stimulation would be desirable, even if clearly loosing the cost-effectiveness of our setup. At the same time, it is always present the possibility of keeping using calcium sensor and opsin overlapping, and in principle stimulating them with the same wavelength. This could bring to the use of a single two-photon laser, changing only the power between imaging and stimulation light source. Some attempts to perform a similar protocol were also performed during this work, unluckily without significant results. Thus, after the optimization of the blue laser stimulation and its full characterization, an interesting step forward would be the investigation of the possibility to target the opsin with the two-photon imaging laser itself. This would lead to an increased specificity and the possibility to activate precisely even deeper glomeruli, keeping a cost-effective setup.

Finally, an interesting development for this work would be the application of the same approach moving to honeybees as animal model. These insects have a richer behavioral spectrum, including social abilities, navigation, strong learning and memory performances; at the same time, they have a bigger and complex brain, even if always of reduced dimensions (about 1mm³) with respect to the mammalian one. This study was not possible until now and to our knowledge nobody has performed it, given the impossibility to co-express efficiently calcium sensor and opsin in bee (we also tried some transfections with viruses without success). The problem could be overcome with the introduction of transgenic bees: at the moment such an insect is not available, but the first positive attempt to create a transgenic bee is currently conducted by Beye group (Otte et al., 2018). This would allow to have homogeneous and specific expression of the two molecules in the bee brain, as for flies, and in this way to perform complementary experiments to deeper investigate information coding in the bee antennal lobe, consistently to previous works also performed in our group (Paoli et al., 2018).

Bibliography

- Abbe, E. (1873). Beiträge zur Theorie des Mikroskops und der mikroskopischen Wahrnehmung. *Archiv Für Mikroskopische Anatomie*, 9(1), 456–468. <https://doi.org/10.1007/bf02956176>
- Abbott, S. B. G., Stornetta, R. L., Fortuna, M. G., Depuy, S. D., West, G. H., Harris, T. E., & Guyenet, P. G. (2009). Photostimulation of retrotrapezoid nucleus Phox2b-expressing neurons in vivo produces long-lasting activation of breathing in rats. *Journal of Neuroscience*, 29(18), 5806–5819. <https://doi.org/10.1523/JNEUROSCI.1106-09.2009>
- Adamantidis, A. R., Zhang, F., Aravanis, A. M., Deisseroth, K., & De Lecea, L. (2007). Neural substrates of awakening probed with optogenetic control of hypocretin neurons. *Nature*, 450(7168), 420–424. <https://doi.org/10.1038/nature06310>
- Albert, H., Coons, M. D., & Kaplan, M. H. (1950). Localization of antigen in tissue cells; improvements in a method for the detection of antigen by means of fluorescent antibody. *The Journal of Experimental Medicine*, 91(1), 1–13. <https://doi.org/10.1084/jem.91.1.1>
- Alilain, W. J., Li, X., Horn, K. P., Dhingra, R., Dick, T. E., Herlitze, S., & Silver, J. (2008). Light-induced rescue of breathing after spinal cord injury. *Journal of Neuroscience*, 28(46), 11862–11870. <https://doi.org/10.1523/JNEUROSCI.3378-08.2008>
- Almedom, R. B., Liewald, J. F., Hernando, G., Schultheis, C., Rayes, D., Pan, J., Schedletzky, T., Hutter, H., Bouzat, C., & Gottschalk, A. (2009). An ER-resident membrane protein complex regulates nicotinic acetylcholine receptor subunit composition at the synapse. *EMBO Journal*, 28(17), 2636–2649. <https://doi.org/10.1038/emboj.2009.204>
- Andrione, M., Timberlake, B. F., Vallortigara, G., Antolini, R., & Haase, A. (2017). Morphofunctional experience-dependent plasticity in the honeybee brain. *Learning and Memory*, 24(12), 622–629. <https://doi.org/10.1101/lm.046243.117>
- Antosiewicz, J. M., & Shugar, D. (2016). UV-Vis spectroscopy of tyrosine side-groups in studies of protein structure. Part 1: basic principles and properties of tyrosine chromophore. *Biophysical Reviews*, 8(2), 151–161. <https://doi.org/10.1007/s12551-016-0198-6>
- Arrenberg, A. B., Del Bene, F., & Baier, H. (2009). Optical control of zebrafish behavior with halorhodopsin. *Proceedings of the National Academy of Sciences of the United States of America*, 106(42), 17968–17973. <https://doi.org/10.1073/pnas.0906252106>
- Arrenberg, A. B., Stainier, D. Y. R., Baier, H., & Huisken, J. (2010). *Optogenetic Control of Cardiac Function*. November, 971–974.
- Ayling, O. G. S., Harrison, T. C., Boyd, J. D., Goroshkov, A., & Murphy, T. H. (2009). Automated light-based mapping of motor cortex by photoactivation of channelrhodopsin-2 transgenic mice. *Nature Methods*, 6(3), 219–224. <https://doi.org/10.1038/nmeth.1303>
- Barad, Y., Eisenberg, H., Horowitz, M., & Silberberg, Y. (1997). Nonlinear scanning laser microscopy by third harmonic generation. *Applied Physics Letters*, 70(8), 922–924. <https://doi.org/10.1063/1.118442>
- Barnett, L. M., Hughes, T. E., & Drobizhev, M. (2017). Deciphering the molecular mechanism responsible for GCaMP6m's Ca²⁺-dependent change in fluorescence. *PLoS ONE*, 12(2), 1–24. <https://doi.org/10.1371/journal.pone.0170934>
- Bellmann, D., Richardt, A., Freyberger, R., Nuwal, N., Schwärzel, M., Fiala, A., & Störtkuhl, K. F. (2010). Optogenetically induced olfactory stimulation in drosophila larvae reveals the neuronal basis of odor-aversion behavior. *Frontiers in Behavioral Neuroscience*, 4(JUN), 1–10.

<https://doi.org/10.3389/fnbeh.2010.00027>

- Berndt, Andre, Lee, S. Y., Ramakrishnan, C., & Deisseroth, K. (2014). Structure-Guided Transformation of Channelrhodopsin into a Light-Activated Chloride Channel. *Science (New York, N.Y.)*, 344(April), 420–424. <https://doi.org/10.5061/dryad.9r0p6>
- Berndt, André, Yizhar, O., Gunaydin, L. A., Hegemann, P., & Deisseroth, K. (2009). Bi-stable neural state switches. *Nature Neuroscience*, 12(2), 229–234. <https://doi.org/10.1038/nn.2247>
- Borue, X., Cooper, S., Hirsh, J., Condrón, B., & Venton, B. J. (2009). Quantitative evaluation of serotonin release and clearance in Drosophila. *Journal of Neuroscience Methods*, 179(2), 300–308. <https://doi.org/10.1016/j.jneumeth.2009.02.013>
- Bovetti, S., Moretti, C., Zucca, S., Dal Maschio, M., Bonifazi, P., & Fellin, T. (2017). Simultaneous high-speed imaging and optogenetic inhibition in the intact mouse brain. *Scientific Reports*, 7(February). <https://doi.org/10.1038/srep40041>
- Boyden, E. S. (2011). Optogenetics: using light to control the brain. *Cerebrum : The Dana Forum on Brain Science*, 2011(November), 16. <http://www.ncbi.nlm.nih.gov/pubmed/23447785> <http://www.pubmedcentral.nih.gov/articlerender.fcgi?artid=PMC3574762>
- Boyden, E. S., Zhang, F., Bamberg, E., Nagel, G., & Deisseroth, K. (2005). Millisecond-timescale, genetically targeted optical control of neural activity. *Nature Neuroscience*, 8(9), 1263–1268. <https://doi.org/10.1038/nn1525>
- Braubach, O., Tombaz, T., Geiller, T., Homma, R., Bozza, T., Cohen, L. B., & Choi, Y. (2018). Sparsened neuronal activity in an optogenetically activated olfactory glomerulus. *Scientific Reports*, 8(1), 1–17. <https://doi.org/10.1038/s41598-018-33021-w>
- Brown, M. T. C., Bellone, C., Mameli, M., Labouèbe, G., Bocklisch, C., Balland, B., Dahan, L., Luján, R., Deisseroth, K., & Lüscher, C. (2010). Drug-driven AMPA receptor redistribution mimicked by selective dopamine neuron stimulation. *PLoS ONE*, 5(12). <https://doi.org/10.1371/journal.pone.0015870>
- Bruegmann, T., Malan, D., Hesse, M., Beiert, T., Fuegemann, C. J., Fleischmann, B. K., & Sasse, P. (2010). Optogenetic control of heart muscle in vitro and in vivo. *Nature Methods*, 7(11), 897–900. <https://doi.org/10.1038/nmeth.1512>
- Busskamp, V., Duebel, J., Balya, D., Fradot, M., Viney, T. J., Siebert, S., Groner, A. C., Cabuy, E., Forster, V., Seeliger, M., Biel, M., Humphries, P., Paques, M., Mohand-Said, S., Trono, D., Deisseroth, K., Sahel, J. A., Picaud, S., & Roska, B. (2010). Genetic reactivation of cone photoreceptors restores visual responses in retinitis pigmentosa. *Science*, 329(5990), 413–417. <https://doi.org/10.1126/science.1190897>
- Cannel, M. B., Berlin, J. R., & Lederer, W. J. (1987). Intracellular calcium in cardiac myocytes: calcium transients measured using fluorescence imaging. *Soc Gen Physiol Ser.*, 42, 201–214.
- Cardin, J. A., Carlén, M., Meletis, K., Knoblich, U., Zhang, F., Deisseroth, K., Tsai, L. H., & Moore, C. I. (2009). Driving fast-spiking cells induces gamma rhythm and controls sensory responses. *Nature*, 459(7247), 663–667. <https://doi.org/10.1038/nature08002>
- Carter, M. E., Yizhar, O., Chikahisa, S., Nguyen, H., Adamantidis, A., Nishino, S., Deisseroth, K., & De Lecea, L. (2010). Tuning arousal with optogenetic modulation of locus coeruleus neurons. *Nature Neuroscience*, 13(12), 1526–1535. <https://doi.org/10.1038/nn.2682>
- Chalfie, M., Tu, Y., Euskirchen, G., Ward William, W., & Prasher Douglas, C. (1994). Green fluorescent protein as a marker for gene expression. *Science*, 263(5148), 802–805. <https://doi.org/10.1126/science.8303295>

- Chen, T. W., Wardill, T. J., Sun, Y., Pulver, S. R., Renninger, S. L., Baohan, A., Schreiter, E. R., Kerr, R. A., Orger, M. B., Jayaraman, V., Looger, L. L., Svoboda, K., & Kim, D. S. (2013). Ultrasensitive fluorescent proteins for imaging neuronal activity. *Nature*, *499*(7458), 295–300. <https://doi.org/10.1038/nature12354>
- Chuhma, N., Tanaka, K. F., Hen, R., & Rayport, S. (2011). Functional connectome of the striatal medium spiny neuron. *Journal of Neuroscience*, *31*(4), 1183–1192. <https://doi.org/10.1523/JNEUROSCI.3833-10.2011>
- Ciocchi, S., Herry, C., Grenier, F., Wolff, S. B. E., Letzkus, J. J., Vlachos, I., Ehrlich, I., Sprengel, R., Deisseroth, K., Stadler, M. B., Müller, C., & Lüthi, A. (2010). Encoding of conditioned fear in central amygdala inhibitory circuits. *Nature*, *468*(7321), 277–282. <https://doi.org/10.1038/nature09559>
- Conti, E., Allegra Mascaro, A., & Pavone, F. (2019). Large Scale Double-Path Illumination System with Split Field of View for the All-Optical Study of Inter-and Intra-Hemispheric Functional Connectivity on Mice. *Methods and Protocols*, *2*(1), 11. <https://doi.org/10.3390/mps2010011>
- Covington, H. E., Lobo, M. K., Maze, I., Vialou, V., Hyman, J. M., Zaman, S., LaPlant, Q., Mouzon, E., Ghose, S., Tammimga, C. A., Neve, R. L., Deisseroth, K., & Nestler, E. J. (2010). Antidepressant effect of optogenetic stimulation of the medial prefrontal cortex. *Journal of Neuroscience*, *30*(48), 16082–16090. <https://doi.org/10.1523/JNEUROSCI.1731-10.2010>
- Crick, F. H. C. (1979). Thinking about the brain. In *Scientific American*, *241* (pp. 219–233).
- dal Maschio, M., Donovan, J. C., Helmbrecht, T. O., & Baier, H. (2017). Linking Neurons to Network Function and Behavior by Two-Photon Holographic Optogenetics and Volumetric Imaging. *Neuron*, *94*(4), 774–789.e5. <https://doi.org/10.1016/j.neuron.2017.04.034>
- Dana, H., Sun, Y., Mohar, B., Hulse, B. K., Kerlin, A. M., Hasseman, J. P., Tsegaye, G., Tsang, A., Wong, A., Patel, R., Macklin, J. J., Chen, Y., Konnerth, A., Jayaraman, V., Looger, L. L., Schreiter, E. R., Svoboda, K., & Kim, D. S. (2019). High-performance calcium sensors for imaging activity in neuronal populations and microcompartments. *Nature Methods*, *16*(7), 649–657. <https://doi.org/10.1038/s41592-019-0435-6>
- Deisseroth, K., Feng, G., Majewska, A. K., Miesenböck, G., Ting, A., & Schnitzer, M. J. (2006). Next-generation optical technologies for illuminating genetically targeted brain circuits. *Journal of Neuroscience*, *26*(41), 10380–10386. <https://doi.org/10.1523/JNEUROSCI.3863-06.2006>
- Denk, W., Strickler, J. H., & Webb, W. W. (1990). *Two-Photon Laser Scanning Fluorescence Microscopy*. April, 1–4.
- Devaud, J.-M., Papouin, T., Carcaud, J., Sandoz, J.-C., Grünewald, B., & Giurfa, M. (2015). Neural substrate for higher-order learning in an insect: Mushroom bodies are necessary for configural discriminations. *Proceedings of the National Academy of Sciences*, *112*(43). <https://doi.org/10.1073/pnas.1508422112>
- Diaspro, A., & Robello, M. (2000). Two-photon excitation of fluorescence for three-dimensional optical imaging of biological structures. *Journal of Photochemistry and Photobiology B: Biology*, *55*(1), 1–8. [https://doi.org/10.1016/S1011-1344\(00\)00028-2](https://doi.org/10.1016/S1011-1344(00)00028-2)
- Diester, I., Kaufman, M. T., Mogri, M., Pashaie, R., Goo, W., Yizhar, O., Ramakrishnan, C., Deisseroth, K., & Shenoy, K. V. (2011). An optogenetic toolbox designed for primates. *Nature Neuroscience*, *14*(3), 387–397. <https://doi.org/10.1038/nn.2749>
- Douglass, A. D., Kraves, S., Deisseroth, K., Schier, A. F., & Engert, F. (2008). Escape Behavior Elicited by Single, Channelrhodopsin-2-Evoked Spikes in Zebrafish Somatosensory Neurons. *Current Biology*, *18*(15), 1133–1137. <https://doi.org/10.1016/j.cub.2008.06.077>
- Eichler, K., Li, F., Litwin-Kumar, A., Park, Y., Andrade, I., Schneider-Mizell, C. M., Saumweber, T., Huser, A., Eschbach, C., Gerber, B., Fetter, R. D., Truman, J. W., Priebe, C. E., Abbott, L. F., Thum, A. S., Zlatic, M., &

- Cardona, A. (2017). The complete connectome of a learning and memory centre in an insect brain. *Nature*, *548*(7666), 175–182. <https://doi.org/10.1038/nature23455>
- Faber, T., Joerges, J., & Menzel, R. (1999). Associative learning modifies neural representations of odors in the insect brain. *Nature Neuroscience*, *2*(1), 74–78. <https://doi.org/10.1038/4576>
- Fenno, L., Yizhar, O., & Deisseroth, K. (2011). The Development and Application of Optogenetics. *Annual Review of Neuroscience*, *34*(1), 389–412. <https://doi.org/10.1146/annurev-neuro-061010-113817>
- Fishilevich, E., & Vosshall, L. B. (2005). Genetic and functional subdivision of the *Drosophila* antennal lobe. *Current Biology*, *15*(17), 1548–1553. <https://doi.org/10.1016/j.cub.2005.07.066>
- Forli, A., Vecchia, D., Binini, N., Succol, F., Bovetti, S., Moretti, C., Nespoli, F., Mahn, M., Baker, C. A., Bolton, M. M., Yizhar, O., & Fellin, T. (2018). Two-Photon Bidirectional Control and Imaging of Neuronal Excitability with High Spatial Resolution In Vivo. *Cell Reports*, *22*(11), 3087–3098. <https://doi.org/10.1016/j.celrep.2018.02.063>
- Förster, D., Dal Maschio, M., Laurell, E., & Baier, H. (2017). An optogenetic toolbox for unbiased discovery of functionally connected cells in neural circuits. *Nature Communications*, *8*(1). <https://doi.org/10.1038/s41467-017-00160-z>
- Freund, I., & Deutsch, M. (1986). Second-harmonic microscopy of biological tissue. *Optics Letters*, *11*(2), 94. <https://doi.org/10.1364/ol.11.000094>
- Galizia, C. G. (2014). Olfactory coding in the insect brain: Data and conjectures. *European Journal of Neuroscience*, *39*(11), 1784–1795. <https://doi.org/10.1111/ejn.12558>
- Galizia, C. G., Sachse, S., Rappert, A., & Menzel, R. (1999). The glomerular code for odor representation is species specific in the honeybee *Apis mellifera*. *Nature Neuroscience*, *2*(5), 473–478. <https://doi.org/10.1038/8144>
- Garini, Y., Vermolen, B. J., & Young, I. T. (2005). From micro to nano: Recent advances in high-resolution microscopy. *Current Opinion in Biotechnology*, *16*(1 SPEC. ISS.), 3–12. <https://doi.org/10.1016/j.copbio.2005.01.003>
- Goepper Mayer, M. (1931). Ueber elementarakte mit zwei quantenspruengen. *Ann. Phys.*, *9*, 273–294.
- Gordon, M. D., & Scott, K. (2009). Motor Control in a *Drosophila* Taste Circuit. *Neuron*, *61*(3), 373–384. <https://doi.org/10.1016/j.neuron.2008.12.033>
- Gradinaru, V., Thompson, K. R., & Deisseroth, K. (2008). eNpHR: A *Natronomonas* halorhodopsin enhanced for optogenetic applications. *Brain Cell Biology*, *36*(1–4), 129–139. <https://doi.org/10.1007/s11068-008-9027-6>
- Gradinaru, V., Thompson, K. R., Zhang, F., Mogri, M., Kay, K., Schneider, M. B., & Deisseroth, K. (2007). Targeting and readout strategies for fast optical neural control in vitro and in vivo. *Journal of Neuroscience*, *27*(52), 14231–14238. <https://doi.org/10.1523/JNEUROSCI.3578-07.2007>
- Gradinaru, V., Zhang, F., Ramakrishnan, C., Mattis, J., Prakash, R., Diester, I., Goshen, I., Thompson, K. R., & Deisseroth, K. (2010). Molecular and Cellular Approaches for Diversifying and Extending Optogenetics. *Cell*, *141*(1), 154–165. <https://doi.org/10.1016/j.cell.2010.02.037>
- Gryczynski, I., Szmajcinski, H., & Lakowicz, J. R. (1995). On the possibility of calcium imaging using Indo-1 with three-photon excitation. *Photochem Photobiol*, *62*(4), 804–808. http://www.ncbi.nlm.nih.gov/entrez/query.fcgi?cmd=Retrieve&db=PubMed&dopt=Citation&list_uids=7480157
- Gunaydin, L. A., Yizhar, O., Berndt, A., Sohal, V. S., Deisseroth, K., & Hegemann, P. (2010). Ultrafast optogenetic control. *Nature Neuroscience*, *13*(3), 387–392. <https://doi.org/10.1038/nn.2495>

- Guo, Z. V., Hart, A. C., & Ramanathan, S. (2009). Optical interrogation of neural circuits in *Caenorhabditis elegans*. *Nature Methods*, 6(12), 891–896. <https://doi.org/10.1038/nmeth.1397>
- Haase, A., Rigosi, E., Trona, F., Anfora, G., Vallortigara, G., Antolini, R., & Vinegoni, C. (2011). In-vivo two-photon imaging of the honey bee antennal lobe. *Biomedical Optics Express*, 2(1), 131. <https://doi.org/10.1364/BOE.2.000131>
- Hallem, E. A., & Carlson, J. R. (2006). Coding of Odors by a Receptor Repertoire. *Cell*, 125(1), 143–160. <https://doi.org/10.1016/j.cell.2006.01.050>
- Hamblin, M. R., & Avci, P. (2015). *Applications of Nanoscience in Photomedicine*.
- Han, X., Qian, X., Bernstein, J. G., Zhou, H. hui, Franzesi, G. T., Stern, P., Bronson, R. T., Graybiel, A. M., Desimone, R., & Boyden, E. S. (2009). Millisecond-Timescale Optical Control of Neural Dynamics in the Nonhuman Primate Brain. *Neuron*, 62(2), 191–198. <https://doi.org/10.1016/j.neuron.2009.03.011>
- Haubensak, W., Kunwar, P. S., Cai, H., Ciocchi, S., Wall, N. R., Ponnusamy, R., Biag, J., Dong, H. W., Deisseroth, K., Callaway, E. M., Fanselow, M. S., Lüthi, A., & Anderson, D. J. (2010). Genetic dissection of an amygdala microcircuit that gates conditioned fear. *Nature*, 468(7321), 270–276. <https://doi.org/10.1038/nature09553>
- Helmbrecht, T. O., dal Maschio, M., Donovan, J. C., Koutsouli, S., & Baier, H. (2018). Topography of a Visuomotor Transformation. *Neuron*, 100(6), 1429–1445.e4. <https://doi.org/10.1016/j.neuron.2018.10.021>
- Hira, R., Honkura, N., Noguchi, J., Maruyama, Y., Augustine, G. J., Kasai, H., & Matsuzaki, M. (2009). Transcranial optogenetic stimulation for functional mapping of the motor cortex. *Journal of Neuroscience Methods*, 179(2), 258–263. <https://doi.org/10.1016/j.jneumeth.2009.02.001>
- Hirase, H., Nikolenko, V., Goldberg, J. H., & Yuste, R. (2002). Multiphoton stimulation of neurons. *Journal of Neurobiology*, 51(3), 237–247. <https://doi.org/10.1002/neu.10056>
- Hornstein, N. J., Pulver, S. R., & Griffith, L. C. (2009). Channelrhodopsin2 mediated stimulation of synaptic potentials at drosophila neuromuscular junctions. *Journal of Visualized Experiments*, 25, 3–5. <https://doi.org/10.3791/1133>
- Huang, C., Tai, C. Y., Yang, K. P., Chang, W. K., Hsu, K. J., Hsiao, C. C., Wu, S. C., Lin, Y. Y., Chiang, A. S., & Chu, S. W. (2019). All-Optical Volumetric Physiology for Connectomics in Dense Neuronal Structures. *IScience*, 22, 133–146. <https://doi.org/10.1016/j.isci.2019.11.011>
- Hull, C., Adesnik, H., & Scanziani, M. (2009). Neocortical disinaptic inhibition requires somatodendritic integration in interneurons. *Journal of Neuroscience*, 29(28), 8991–8995. <https://doi.org/10.1523/JNEUROSCI.5717-08.2009>
- Hwang, R. Y., Zhong, L., Xu, Y., Johnson, T., Zhang, F., Deisseroth, K., & Tracey, W. D. (2007). Nociceptive Neurons Protect *Drosophila* Larvae from Parasitoid Wasps. *Current Biology*, 17(24), 2105–2116. <https://doi.org/10.1016/j.cub.2007.11.029>
- Jeanne, J. M., Fişek, M., & Wilson, R. I. (2018). The Organization of Projections from Olfactory Glomeruli onto Higher-Order Neurons. *Neuron*, 98(6), 1198–1213.e6. <https://doi.org/10.1016/j.neuron.2018.05.011>
- Johansen, J. P., Hamanaka, H., Monfils, M. H., Behnia, R., Deisseroth, K., Blair, H. T., & LeDoux, J. E. (2010). Optical activation of lateral amygdala pyramidal cells instructs associative fear learning. *Proceedings of the National Academy of Sciences of the United States of America*, 107(28), 12692–12697. <https://doi.org/10.1073/pnas.1002418107>
- Kaiser, W., & Garrett, C. G. B. (1961). Two-photon excitation in CaF₂: Eu²⁺. *Physical Review Letters*, 7(6),

229–231. <https://doi.org/10.1103/PhysRevLett.7.229>

- Kanbar, R., Stornetta, R. L., Cash, D. R., Lewis, S. J., & Guyenet, P. G. (2010). Photostimulation of Phox2b medullary neurons activates cardiorespiratory function in conscious rats. *American Journal of Respiratory and Critical Care Medicine*, *182*(9), 1184–1194. <https://doi.org/10.1164/rccm.201001-00470C>
- Kato, H. E., Zhang, F., Yizhar, O., Ramakrishnan, C., Nishizawa, T., Hirata, K., Ito, J., Aita, Y., Tsukazaki, T., Hayashi, S., Hegemann, P., Maturana, A. D., Ishitani, R., Deisseroth, K., & Nureki, O. (2012). Crystal structure of the channelrhodopsin light-gated cation channel. *Nature*, *482*(7385), 369–374. <https://doi.org/10.1038/nature10870>
- Kätzel, D., Zemelman, B. V., Buetfering, C., Wölfel, M., & Miesenböck, G. (2011). The columnar and laminar organization of inhibitory connections to neocortical excitatory cells. *Nature Neuroscience*, *14*(1), 100–109. <https://doi.org/10.1038/nn.2687>
- Kim, A. J., Lazar, A. A., & Slutskiy, Y. B. (2015). Projection neurons in Drosophila antennal lobes signal the acceleration of odor concentrations. *ELife*, *4*(MAY), 1–11. <https://doi.org/10.7554/eLife.06651>
- Kim, C. K., Yang, S. J., Pichamoorthy, N., Young, N. P., Kauvar, I., Jennings, J. H., Lerner, T. N., Berndt, A., Lee, S. Y., Ramakrishnan, C., Davidson, T. J., Inoue, M., Bito, H., & Deisseroth, K. (2016). Simultaneous fast measurement of circuit dynamics at multiple sites across the mammalian brain. *Nature Methods*, *13*(4), 325–328. <https://doi.org/10.1038/nmeth.3770>
- Lee, J. H., Durand, R., Gradinaru, V., Zhang, F., Goshen, I., Kim, D. S., Fenno, L. E., Ramakrishnan, C., & Deisseroth, K. (2010). Global and local fMRI signals driven by neurons defined optogenetically by type and wiring. *Nature*, *465*(7299), 788–792. <https://doi.org/10.1038/nature09108>
- Li, X., Gutierrez, D. V., Hanson, M. G., Han, J., Mark, M. D., Chiel, H., Hegemann, P., Landmesser, L. T., & Herlitze, S. (2005). Fast noninvasive activation and inhibition of neural and network activity by vertebrate rhodopsin and green algae channelrhodopsin. *Proceedings of the National Academy of Sciences*, *102*(49), 17816–17821. <https://doi.org/10.1073/PNAS.0509030102>
- Liewald, J. F., Brauner, M., Stephens, G. J., Bouhours, M., Schultheis, C., Zhen, M., & Gottschalk, A. (2008). Optogenetic analysis of synaptic function. *Nature Methods*, *5*(10), 895–902. <https://doi.org/10.1038/nmeth.1252>
- Lima, S. Q., & Miesenböck, G. (2005). Remote control of behavior through genetically targeted photostimulation of neurons. *Cell*, *121*(1), 141–152. <https://doi.org/10.1016/j.cell.2005.02.004>
- Lin, J. Y., Knutsen, P. M., Muller, A., Kleinfeld, D., & Tsien, R. Y. (2013). ReaChR: A red-shifted variant of channelrhodopsin enables deep transcranial optogenetic excitation. *Nature Neuroscience*, *16*(10), 1499–1508. <https://doi.org/10.1038/nn.3502>
- Lin, J. Y., Lin, M. Z., Steinbach, P., & Tsien, R. Y. (2009). Characterization of engineered channelrhodopsin variants with improved properties and kinetics. *Biophysical Journal*, *96*(5), 1803–1814. <https://doi.org/10.1016/j.bpj.2008.11.034>
- Lin, M. Z., & Schnitzer, M. J. (2017). Genetically encoded indicators of neuronal activity. *Physiology & Behavior*, *176*(1), 139–148. <https://doi.org/10.1016/j.physbeh.2017.03.040>
- Llewellyn, M. E., Thompson, K. R., Deisseroth, K., & Delp, S. L. (2010). Orderly recruitment of motor units under optical control in vivo. *Nature Medicine*, *16*(10), 1161–1165. <https://doi.org/10.1038/nm.2228>
- Low, S. E., Ryan, J., Sprague, S. M., Hirata, H., Cui, W. W., Zhou, W., Hume, R. I., Kuwada, J. Y., & Saint-Amant, L. (2010). Touché Is Required for Touch-Evoked Generator Potentials Within Vertebrate Sensory Neurons. *Journal of Neuroscience*, *30*(28), 9359–9367. <https://doi.org/10.1523/JNEUROSCI.1639-10.2010>

- Lozier, R. H., Bogomolni, R. A., & Stoeckenius, W. (1975). Bacteriorhodopsin: a light-driven proton pump in Halobacterium Halobium. *Biophysical Journal*, 15(9), 955–962. [https://doi.org/10.1016/S0006-3495\(75\)85875-9](https://doi.org/10.1016/S0006-3495(75)85875-9)
- Mardinly, A. R., Oldenburg, I. A., Pégard, N. C., Sridharan, S., Lyall, E. H., Chesnov, K., Brohawn, S. G., Waller, L., & Adesnik, H. (2018). Precise multimodal optical control of neural ensemble activity. *Nature Neuroscience*, 21(6), 881–893. <https://doi.org/10.1038/s41593-018-0139-8>
- Marshel, J. H., Kim, Y. S., Machado, T. A., Quirin, S., Benson, B., Kadmon, J., Raja, C., Chibukhchyan, A., Ramakrishnan, C., Inoue, M., Shane, J. C., McKnight, D. J., Yoshizawa, S., Kato, H. E., Ganguli, S., & Deisseroth, K. (2019). Cortical layer-specific critical dynamics triggering perception. *Science*, 365(6453). <https://doi.org/10.1126/science.aaw5202>
- Martelli, C., Carlson, J. R., & Emonet, T. (2013). Intensity Invariant Dynamics and Odor-Specific Latencies in Olfactory Receptor Neuron Response. *Journal of Neuroscience*, 33(15), 6285–6297. <https://doi.org/10.1523/JNEUROSCI.0426-12.2013>
- Mattis, J., Tye, K. M., Ferenczi, E. A., Ramakrishnan, C., O’Shea, D. J., Prakash, R., Gunaydin, L. A., Hyun, M., Fenno, L. E., Gradinaru, V., Yizhar, O., & Deisseroth, K. (2012). Principles for applying optogenetic tools derived from direct comparative analysis of microbial opsins. *Nature Methods*, 9(2), 159–172. <https://doi.org/10.1038/nmeth.1808>
- Nagel, G., Brauner, M., Liewald, J. F., Adeishvili, N., Bamberg, E., & Gottschalk, A. (2005). Light activation of Channelrhodopsin-2 in excitable cells of caenorhabditis elegans triggers rapid behavioral responses. *Current Biology*, 15(24), 2279–2284. <https://doi.org/10.1016/j.cub.2005.11.032>
- Nagel, G., Ollig, D., Fuhrmann, M., Kateriya, S., Musti, A. M., Bamberg, E., & Hegemann, P. (2002). Channelrhodopsin-1: A light-gated proton channel in green algae. *Science*, 296(5577), 2395–2398. <https://doi.org/10.1126/science.1072068>
- Nagel, G., Szellas, T., Huhn, W., Kateriya, S., Adeishvili, N., Berthold, P., Ollig, D., Hegemann, P., & Bamberg, E. (2003). Channelrhodopsin-2, a directly light-gated cation-selective membrane channel. *Pnas*, 100(24), 13940–13945. <https://doi.org/10.1073/pnas.1936192100>
- Oesterhelt, D., & Stoeckenius, W. (1971). Rhodopsin-like protein from the purple membrane of Halobacterium halobium. *Nature New Biology*, 233(39), 149–152. <https://doi.org/10.1038/newbio233149a0>
- Otte, M., Netschitailo, O., Kaftanoglu, O., Wang, Y., Page, R. E., & Beye, M. (2018). Improving genetic transformation rates in honeybees. *Scientific Reports*, 8(1), 1–6. <https://doi.org/10.1038/s41598-018-34724-w>
- Packer, A. M., Russell, L. E., Dagleish, H. W. P., & Häusser, M. (2015). Simultaneous all-optical manipulation and recording of neural circuit activity with cellular resolution in vivo. *Nature Methods*, 12(2), 140–146. <https://doi.org/10.1038/nmeth.3217>
- Paoli, M., Albi, A., Zanon, M., Zanini, D., Antolini, R., & Haase, A. (2018). Neuronal response latencies encode first odor identity information across subjects. *Journal of Neuroscience*, 38(43), 9240–9251. <https://doi.org/10.1523/JNEUROSCI.0453-18.2018>
- Paoli, M., Weisz, N., Antolini, R., & Haase, A. (2016). Spatially resolved time-frequency analysis of odour coding in the insect antennal lobe. *European Journal of Neuroscience*, 44(6), 2387–2395. <https://doi.org/10.1111/ejn.13344>
- Peteanu, L., Huber, D., Sobczyk, A., & Svoboda, K. (2007). Channelrhodopsin-2-assisted circuit mapping of long-range callosal projections. *Nature Neuroscience*, 10(5), 663–668. <https://doi.org/10.1038/nn1891>
- Peteanu, L., Mao, T., Sternson, S. M., & Svoboda, K. (2009). The subcellular organization of neocortical

- Stirman, J. N., Brauner, M., Gottschalk, A., & Lu, H. (2010). High-throughput study of synaptic transmission at the neuromuscular junction enabled by optogenetics and microfluidics. *Journal of Neuroscience Methods*, *191*(1), 90–93. <https://doi.org/10.1016/j.jneumeth.2010.05.019>
- Stoeckenius, W. (1985). The rhodopsin-like pigments of halobacteria: light-energy and signal transducers in an archaeobacterium. *Trends in Biochemical Sciences*, *10*(12), 483–486. [https://doi.org/10.1016/0968-0004\(85\)90210-5](https://doi.org/10.1016/0968-0004(85)90210-5)
- Stroh, A., Tsai, H. C., Wang, L. P., Zhang, F., Kressel, J., Aravanis, A., Santhanam, N., Deisseroth, K., Konnerth, A., & Schneider, M. B. (2011). Tracking stem cell differentiation in the setting of automated optogenetic stimulation. *Stem Cells*, *29*(1), 78–88. <https://doi.org/10.1002/stem.558>
- Strube-Bloss, M. F., & Rössler, W. (2018). Multimodal integration and stimulus categorization in putative mushroom body output neurons of the honeybee. *Royal Society Open Science*, *5*(2). <https://doi.org/10.1098/rsos.171785>
- Szabo, V., Ventalon, C., De Sars, V., Bradley, J., & Emiliani, V. (2014). Spatially selective holographic photoactivation and functional fluorescence imaging in freely behaving mice with a fiberscope. *Urology*, *84*(6), 1157–1169. <https://doi.org/10.1016/j.neuron.2014.11.005>
- Tian, L., Hires, S. A., Mao, T., Huber, D., Chiappe, M. E., Chalasani, S. H., Petreanu, L., Akerboom, J., McKinney, S. A., Schreiter, E. R., Bargmann, C. I., Jayaraman, V., Svoboda, K., & Looger, L. L. (2009). Imaging neural activity in worms, flies and mice with improved GCaMP calcium indicators. *Nature Methods*, *6*(12), 875–881. <https://doi.org/10.1038/nmeth.1398>
- Tye, K. M., Prakash, R., Kim, S. Y., Fenno, L. E., Grosenick, L., Zarabi, H., Thompson, K. R., Gradinaru, V., Ramakrishnan, C., & Deisseroth, K. (2011). Amygdala circuitry mediating reversible and bidirectional control of anxiety. *Nature*, *471*(7338), 358–362. <https://doi.org/10.1038/nature09820>
- Venkatachalam, V., & Cohen, A. E. (2014). Imaging GFP-based reporters in neurons with multiwavelength optogenetic control. *Biophysical Journal*, *107*(7), 1554–1563. <https://doi.org/10.1016/j.bpj.2014.08.020>
- Wang, H., Peca, J., Matsuzaki, M., Matsuzaki, K., Noguchi, J., Qiu, L., Wang, D., Zhang, F., Boyden, E., Deisseroth, K., Kasai, H., Hall, W. C., Feng, G., & Augustine, G. J. (2007). High-speed mapping of synaptic connectivity using photostimulation in Channelrhodopsin-2 transgenic mice. *Proceedings of the National Academy of Sciences of the United States of America*, *104*(19), 8143–8148. <https://doi.org/10.1073/pnas.0700384104>
- Wang, J. W., Wong, A. M., Flores, J., Vosshall, L. B., & Axel, R. (2003). Two-photon calcium imaging reveals an odor-evoked map of activity in the fly brain. *Cell*, *112*(2), 271–282. <http://www.ncbi.nlm.nih.gov/pubmed/12553914>
- Weick, J. P., Johnson, M. A., Skroch, S. P., Williams, J. C., Deisseroth, K., & Zhang, S. C. (2010). Functional control of transplantable human ESC-derived neurons via optogenetic targeting. *Stem Cells*, *28*(11), 2008–2016. <https://doi.org/10.1002/stem.514>
- Wilson, N. R., Runyan, C. A., Wang, F. L., & Sur, M. (2012). Division and subtraction by distinct cortical inhibitory networks in vivo. *Nature*, *488*(7411), 343–348. <https://doi.org/10.1038/nature11347>
- Witten, I. B., Lin, S. C., Brodsky, M., Prakash, R., Diester, I., Anikeeva, P., Gradinaru, V., Ramakrishnan, C., & Deisseroth, K. (2010). Cholinergic interneurons control local circuit activity and cocaine conditioning. *Science*, *330*(6011), 1677–1681. <https://doi.org/10.1126/science.1193771>
- Wolf, M. Born, E. (1961). Principles of Optics. *Optica Acta: International Journal of Optics*, *8*(2), 181–182. <https://doi.org/10.1080/713826373>
- Xiang, Y., Yuan, Q., Vogt, N., Looger, L. L., Jan, L. Y., & Jan, Y. N. (2010). Light-avoidance-mediating photoreceptors tile the Drosophila larval body wall. *Nature*, *468*(7326), 921–926.

<https://doi.org/10.1038/nature09576>

- Xu, C., Zipfel, W., Shear, J. B., Williams, R. M., & Webb, W. W. (1996). Multiphoton fluorescence excitation: New spectral windows for biological nonlinear microscopy. *Proceedings of the National Academy of Sciences of the United States of America*, *93*(20), 10763–10768. <https://doi.org/10.1073/pnas.93.20.10763>
- Yang, W., Carrillo-Reid, L., Bando, Y., Peterka, D. S., & Yuste, R. (2018). Simultaneous two-photon imaging and two-photon optogenetics of cortical circuits in three dimensions. *ELife*, *7*, 1–21. <https://doi.org/10.7554/eLife.32671>
- Yizhar, O., Fenno, L. E., Prigge, M., Schneider, F., Davidson, T. J., Ogshea, D. J., Sohal, V. S., Goshen, I., Finkelstein, J., Paz, J. T., Stehfest, K., Fudim, R., Ramakrishnan, C., Huguenard, J. R., Hegemann, P., & Deisseroth, K. (2011). Neocortical excitation/inhibition balance in information processing and social dysfunction. *Nature*, *477*(7363), 171–178. <https://doi.org/10.1038/nature10360>
- Zemelman, B. V., Lee, G. A., Ng, M., & Miesenböck, G. (2002). Selective photostimulation of genetically chARGed neurons. *Neuron*, *33*(1), 15–22. [https://doi.org/10.1016/S0896-6273\(01\)00574-8](https://doi.org/10.1016/S0896-6273(01)00574-8)
- Zhang, F., Gradinaru, V., Adamantidis, A. R., Durand, R., Airan, R. D., De Lecea, L., & Deisseroth, K. (2010). Optogenetic interrogation of neural circuits: Technology for probing mammalian brain structures. *Nature Protocols*, *5*(3), 439–456. <https://doi.org/10.1038/nprot.2009.226>
- Zhang, F., Prigge, M., Beyrière, F., Tsunoda, S. P., Mattis, J., Yizhar, O., Hegemann, P., & Deisseroth, K. (2008). Red-shifted optogenetic excitation: A tool for fast neural control derived from *Volvox carteri*. *Nature Neuroscience*, *11*(6), 631–633. <https://doi.org/10.1038/nn.2120>
- Zhang, F., Wang, L. P., Boyden, E. S., & Deisseroth, K. (2006). Channelrhodopsin-2 and optical control of excitable cells. *Nature Methods*, *3*(10), 785–792. <https://doi.org/10.1038/nmeth936>
- Zhang, F., Wang, L. P., Brauner, M., Liewald, J. F., Kay, K., Watzke, N., Wood, P. G., Bamberg, E., Nagel, G., Gottschalk, A., & Deisseroth, K. (2007). Multimodal fast optical interrogation of neural circuitry. *Nature*, *446*(7136), 633–639. <https://doi.org/10.1038/nature05744>
- Zhang, W., Ge, W., & Wang, Z. (2007). A toolbox for light control of *Drosophila* behaviors through Channelrhodopsin 2-mediated photoactivation of targeted neurons. *European Journal of Neuroscience*, *26*(9), 2405–2416. <https://doi.org/10.1111/j.1460-9568.2007.05862.x>
- Zhang, Y. P., & Oertner, T. G. (2007). Optical induction of synaptic plasticity using a light-sensitive channel. *Nature Methods*, *4*(2), 139–141. <https://doi.org/10.1038/nmeth988>
- Zhang, Z., Russell, L. E., Packer, A. M., Gauld, O. M., & Häusser, M. (2018). Closed-loop all-optical interrogation of neural circuits in vivo. *Nature Methods*, *15*(12), 1037–1040. <https://doi.org/10.1038/s41592-018-0183-z>
- Zimmermann, G., Wang, L. P., Vaughan, A. G., Manoli, D. S., Zhang, F., Deisseroth, K., Baker, B. S., & Scott, M. P. (2009). Manipulation of an innate escape response in *Drosophila*: Photoexcitation of acj6 neurons induces the escape response. *PLoS ONE*, *4*(4), e5100. <https://doi.org/10.1371/journal.pone.0005100>
- Zipfel, W. R., Williams, R. M., & Webb, W. W. (2003). Nonlinear magic: Multiphoton microscopy in the biosciences. *Nature Biotechnology*, *21*(11), 1369–1377. <https://doi.org/10.1038/nbt899>

Personal articles

Paoli, M., Albi, A., Zanon, M., Zanini, D., Antolini, R., & Haase, A. (2018). Neuronal response latencies encode first odor identity information across subjects. *Journal of Neuroscience*, *38*(43), 9240–9251. <https://doi.org/10.1523/JNEUROSCI.0453-18.2018>

Index of abbreviations

1P one-photon

2P two-photon

AL antennal lobe

ChR2 Channelrhodopsin-2

LH lateral horn

MB mushroom body

ORN olfactory receptor neuron

PMT photomultiplier

PN projection neuron

ROI region of interest

Index of figures

Figure 1 Sketch of a monopolar neuron.....	9
Figure 2 Action potential: cell depolarization and repolarization after a stimulus onset are depicted; a refractory period follows before the cell is back to its resting state.....	11
Figure 3 Sketch of drosophila olfactory pathway: the odor is detected by ORNs at the level of the antennae, information is passed to glomeruli in the AL and sent to higher order centers (MBs and LHs) through PNs (Sayin et al., 2018)	12
Figure 4 Jablonski energy level diagram of luminescence processes: fluorescence and phosphorescence are depicted. The singlet ground, first and second electronic states are depicted by S0, S1 and S2, triplet states with T1 and T2; moreover, some vibrational energy levels are added to the graph. Radiative transitions are shown as colored arrows, while non-radiative processes are represented by gray arrows (Antosiewicz & Shugar, 2016).	16
Figure 5 Example of fluorescence absorption (blue) and emission (red) spectra. The emission spectrum is red-shifted (Stokes shift) with respect to absorption one.	17
Figure 6 Point spread function as observed along the y axis: (a) for a conventional microscope, (b) for a confocal microscope. Function calculated for NA=1 and $\lambda = 500\text{nm}$ (Garini et al., 2005).	18
Figure 7 One photon vs. two photon excitation process.....	20
Figure 8 Publications related to multi-photon microscopy (instrumentation development -black-; usages to improve biological research -white-), (Zipfel et al., 2003)	23
Figure 9 Two photon excitation spectra of GCaMP6m are presented as a linear combination of the two individual two-photon action cross-section spectra (Barnett et al., 2017).	24
Figure 10 Scheme of the setup	37
Figure 11 Scheme of filters and PMTs.....	38
Figure 12 Laser power calibration curves. The units on the x axes refer to a scale from 0 to 1000 of arbitrary units of the microscope software.....	41
Figure 13 Lasers alignment procedure. A two-photon image of a yellow marker layer is taken as reference and some points are bleached with the blue laser (0.12 mW at the sample, 500ms): the coordinates of the points can be adjusted by software in order to fit perfectly the effective hole positions. Scale bar 10 μm	42
Figure 14 Bleaching spot by the blue laser at different planes (lower -7 μm , focal 0 μm , upper 9 μm). Scale bar 5 μm	43
Figure 15 HEK cells expressing opsin ChR2:mCherry (red, left); calcium sensor GCaMP6 (green, middle); the right figure represents the merge.	44
Figure 16 Drosophila preparation protocol (Silbering et al., 2012). In figure A it is visible the mounting block with the copper grid fixed; figure B shows the fly blocked by the neck and in figure C a view from the top shows the separation of the antennae from the head complex.	45
Figure 17 Image of a mounting block with the copper grid used to fix drosophila by the neck.	46
Figure 18 The drosophila is blocked with a cactus spine (left), the antennae are pushed by a wire (top right) and covered with a plastic shield (bottom right).	46
Figure 19 Image of a dissected and fixed fly brain, marked with antibody anti-ChETA (top left, magenta) for ChR2-XXL identification and anti-GFP (top right, green) for calcium sensor GCaMP identification. The opsin is expressed in the antennal lobes, GCaMP pan-neuronally. Bottom figure represents the merge. Scale bar: 100 μm . (Damiano Zanini, private communication).	48
Figure 20 Example of a drosophila blocked under the microscope.....	49
Figure 21 Example of raw data intensity profile with four blue laser stimulations. The frames in correspondence with the stimulation present saturated pixels and are clearly detectable (peaks in the profile); consequently they are removed to compute the final profile and analysis.	50

Figure 22 Decay time, rise time and fluorescence variation for different markers. Light blue and magenta are respectively GCaMP6f and GCaMP6m. (Chen et al., 2013).	51
Figure 23 miniPID response curves for the five odorants (mean \pm SEM, n = 5). Red lines denote threshold criteria and onset points for odor concentration increase with respect to valve opening (for more details, Paoli et al., 2018).	52
Figure 24 Simplified flow chart of the custom Matlab app functionalities.....	53
Figure 25 Analysis app layout, loading window	53
Figure 26 App layout, intensity profile and time-frequency analysis	54
Figure 27 HEK cells activation protocol: activation points are depicted on the left (40 points inside one cell), while on the right different ROIs are selected	56
Figure 28 Fluorescence response (percentage in change of intensity) for different ROIs of Figure 27. Two set of 7s-stimulations were performed (the saturated stimulation frames were removed from the profiles where a red vertical line is depicted, indicating the stimulus occurrence).	57
Figure 29 HEK cell stimulation protocol. Green channel (GCaMP, left), red channel (ChR2, middle), ROIs analyzed (right). On the left also the stimulation points are visible, three for ROI 1 (opsin and calcium sensor co-expressing cell) and three for ROI 2 (only calcium sensor expressing cell).	58
Figure 30 Fluorescence response for different ROIs of Figure 26. First stimulation (vertical line) targets the three points in ROI 1, cell co-expressing opsin and calcium sensor; second stimulation targets the three points in ROI 2, cell only expressing GCaMP.	58
Figure 31 HEK cells expressing opsin (red, left) and GCaMP (green, middle). On the right the merge, with yellowish areas representing the co-expression. The co-expression rate is poor (less than 10%).	59
Figure 32 Example of resting state fluorescence (with GCaMP6 at 940nm) of drosophila whole brain (left) and antennal lobe (right). Scale bar: left 100 μ m, right 20 μ m.	60
Figure 33 Reference ROIs corresponding to different glomeruli inside a fly antennal lobe. Intensity profiles for the different ROIs during odors presentation are reported in Figure 34. Scale bar 20 μ m.	61
Figure 34 Intensity profile of fluorescence variation for different ROIs of Figure 33 during an odor mix presentation protocol. The red rectangles represent the odor presentation.	62
Figure 35 Different odors elicit different patterns of glomerular activation in the AL. Scale bar 10 μ m. (J. W. Wang et al., 2003).	63
Figure 36 Intensity profile of fluorescence variation for different ROIs of Figure 33 during 1-hexanol presentation protocol. The red rectangles represent the odor presentation.	64
Figure 37 Averaged response to odor mixture for two different areas in the antennal lobe plane: ROI 1 is the surrounding area where the glia cells are, ROI 2 is inside the antennal lobe. Odors were presented in correspondence of the red rectangles. Scale bar 20 μ m.	65
Figure 38 On the left, a sketch of drosophila olfactory pathway: the odor is detected by ORNs at the level of the antennae, information is passed to glomeruli in the AL and sent to higher order centers (MBs and LHs) through PNs (Sayin et al., 2018). On the right, whole fly brain and selected ROIs; ChR2 is expressed at the level of PNs, GCaMP pan-neuronally. ROI 1 and 2 are the left and right antennal lobe respectively, while in ROI 3 and 4 the upper structure of the mushroom bodies is visible. (the fluorescent image has inverted orientation with respect to the sketch on the left). Two different stimulation points are represented by the red circles (responses in Figure 36 and Figure 37 respectively). Scale bar 100 μ m.	66
Figure 39 Intensity profile averaged over 3 trials (left antennal lobe -ROI 1- stimulation) for ROIs of Figure 38 right.....	67
Figure 40 Intensity profile averaged over 3 trials (right antennal lobe -ROI 2- stimulation) for ROIs of Figure 38 right.....	68
Figure 41 Whole fly brain and selected ROIs; ROI 1 and 2 are the left and right antennal lobe respectively. Two different stimulation points are represented by the red circles (responses in Figure 42 and Figure 43) Scale bar 100 μ m.	69

Figure 42 Intensity profile averaged over 4 stimulus repetitions for ROIs in Figure 41; the left antennal lobe (ROI 1) was targeted.	70
Figure 43 Intensity profile averaged over 4 stimulus repetitions for ROIs in Figure 41: the right antennal lobe (ROI 2) was targeted.	71
Figure 44 Intensity profile for different regions of the fly brain expressing only GCaMP, following a stimulation protocol of the right antennal lobe with 0.025 mW at the sample for 150ms (three repetitions, red vertical lines). ROIs correspond to analogous regions to Figure 41.	72
Figure 45 Color code map of the antennal lobe, indicating areas of the AL (different glomeruli) activated by stimulations of different lengths. The red circle indicates the stimulation point, blueish areas the ones activated by lower lengths and yellowish areas the ones activated by higher length of stimulation. Scale bar 20 μ m.	73
Figure 46 Intensity profile for different glomeruli (ROIs selected in the upper left image), following a double repetition of three points (upper left, red circles) stimulation at intervals of 20s (red vertical lines indicates the different stimuli). The first stimulation is in correspondence of ROI 1, second at ROI 2 and the third one is outside the antennal lobe. Scale bar 20 μ m.	74
Figure 47 Overall intensity profile for two repetitions of three stimulations at different points (red circles, the first two inside the antennal lobe, the third one outside). Scale bar 20 μ m.	75
Figure 48 Antennal lobe response to three stimulations of 200ms (red vertical lines) at relative high power (about 0.2mW at the objective), in a fly expressing only the GCaMP construct. No response to blue light stimulation is detectable at all. The stimulation point is indicated by the red circle. Scale bar 20 μ m.	76
Figure 49 Intensity profiles for different glomeruli depicted in the figure upper left, following a set of 10 stimulations of ROI 1 (red circle in figure upper left) at increasing blue laser powers (stimuli indicated by the red vertical lines). In figure upper right a color code map indicating the lower power necessary to stimulate the different areas is depicted, with powers ordered in ascending order (blueish areas activated by low power, yellowish areas, activated by high power). Power indicated in software a.u. Scale bar 20 μ m.	78
Figure 50 Correlation (right) between different ROIs (depicted on the left) of an opsin expressing antennal lobe, following a blue laser stimulation of ROI 1 (red circle, left). Scale bar 50 μ m.	79
Figure 51 Analysis for a set of 10 stimulations with ascending blue laser power. Upper left, stimulation point (red circle); upper right, overall intensity profile. Lower, three example of seed-based correlation map with stimulation point 2 (for stimuli 1,3,5). Power values from stimulus #1 to #10 (in software a.u.): 156,157,158,159,160,161,162,163,164,165. Scale bar 20 μ m.	80
Figure 52 Correlation maps with stimulation points; left figure refers to a stimulation on the right glomerulus (stimulation on point 2), right figure in the left one (stimulation on point 1); analysis for low power #9 stimulation of series in Figure 51.	80
Figure 53 Correlation maps with stimulation points, left figure refers to a stimulation on the right glomerulus (stimulation on point 2), right in the left one (stimulation on point 1); analysis for high power #1 stimulation of series in Figure 51.	81
Figure 54 Cross-correlation analysis between different areas of the fly brain, following an antennal lobe stimulation (red circle). In color code it is represented the maximum correlation values, the number inside is the corresponding lag value, i.e. the time shift needed to obtain the maximum correlation, expressed in seconds. Scale bar 100 μ m.	82
Figure 55 Antennal lobe with ROIs on different glomeruli (left). The glomerulus stimulated is ROI 1 (red circle). Change in fluorescence after stimulus (at 40s, red vertical line) are reported on the right for all the different ROIs. Scale bar 20 μ m.	82
Figure 56 Cross-correlation and static correlation coefficients between targeted glomerulus 1 of Figure 55 and all the others, in a time windows of 20s before the stimulation.	83
Figure 57 Cross-correlation and static correlation coefficients between targeted glomerulus 1 of Figure 55 and all the others, in a time windows of 20s following the stimulation.	83

Figure 58 Static correlation matrices between all the different ROIs of Figure 55 for the signals in the 10s before the stimulus (left), 10s following it (right) and from 20 to 30s after the stimulus (bottom); (in the titles time reference stimulus occurs at 40s). 84

Figure 59 Profile of ROI1 and ROI5 of Figure 55 after stimulation (top) and magnitude-squared wavelet coherence between the two (bottom). Stimulus at red vertical line. 85

Acknowledgments

Albrecht Haase, P.I., University of Trento (supervisor)

Damiano Zanini, Ph.D., University of Wuerzburg (drosophila line preparation)